Composite Functional Materials
2025, 1(2): 20250202 https://doi.org/10.63823/20250202

REVIEW ARTICLE

Hollow-structured materials for advanced energy storage and conversion: rational synthesis, multifunctional applications, and mechanism insights

Yiran Sun[a,b], Changqu Liu[a,b], Shuqi Ji[a,b], Jinbo Ni[a,b], Xiangning Wu[a,b], Sembukuttiarachilage Ravi Pradip Silva[a,b,c,d], Meng Cai[a,b,d,*], Guosheng Shao[a,b,d,*], Peng Zhang[a,b,d,*]

a. School of Materials Science and Engineering, Zhengzhou University, Zhengzhou 450001, China.
b. State Center for International Cooperation on Designer Low-carbon & Environmental Materials (CDLCEM), Zhengzhou University, Zhengzhou 450001, China.
c. Nanoelectronics Center, Advanced Technology Institute, University of Surrey, Guildford GU2 7XH, UK
d. Zhengzhou Materials Genome Institute (ZMGI), Zhongyuanzhigu, Building 2, Xingyang 450100, China.

ABSTRACT: Hollow-structured materials exhibit breakthrough potential in energy storage and conversion, leveraging unique advantages including high specific surface area, controllable cavity architecture, and short-range mass transfer pathways, alongside tunable functional properties. This review synthesizes recent progress, emphasizing the constitutive relationships governing material synthesis, structural engineering, and resultant performance. Key synthesis strategies including encompassing hard-templating, soft-templating, and template-free approaches are delineated with respect to their mechanisms and characteristics. Subsequently, cutting-edge applications in energy storage systems (e.g., lithium-ion batteries, supercapacitors), conversion systems (e.g., photoelectrocatalysis) and the application of partial in-situ testing technology for exploring the reaction mechanism are highlighted. The review concludes by outlining critical challenges and opportunities pertaining to scalable fabrication, structural stability, and device integration, providing a roadmap for the precise design and performance optimization of these materials.

KEYWORDS: Hollow structure, Template synthesis, Energy storage, Energy conversion, *In situ* testing techniques

Received: July 16, 2025. **Revised:** September 13, 2025. **Accepted:** September 13, 2025. **Available online:** November 11, 2025
***Corresponding author:** mengcai@gs.zzu.edu.cn (M. Cai); gsshao@zzu.edu.cn (G. Shao); zhangp@zzu.edu.cn (P. Zhang)

Graphical Abstract

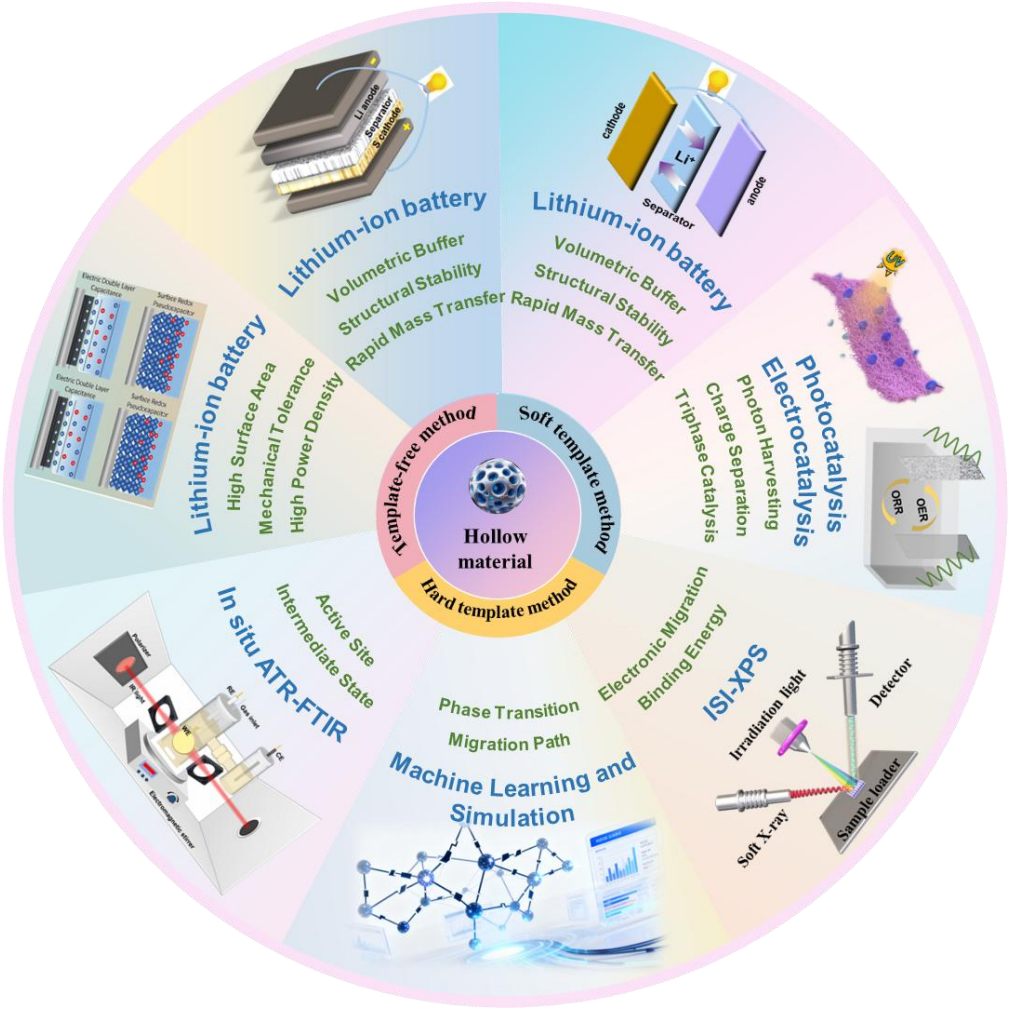

1. Introduction

The global energy transition and pursuit of "dual carbon" strategic goals have intensified research into efficient and stable materials for energy storage and conversion [1, 2]. The properties of a single-phase structural material are predominantly determined by its intrinsic characteristics, such as chemical composition and crystalline structure. Altering its properties typically requires modifying the material itself—for instance, through alloying—which may inadvertently increase overall weight and cost. Conventional bulk materials contain limitations, including sluggish ion diffusion kinetics, low utilization of active sites, and inadequate cycling stability (e.g., significant volume expansion and particle fragmentation in silicon anodes leading to rapid capacity decay). These constraints impede their ability to meet the performance demands of next-generation energy devices. Consequently, hollow-structured materials [3-9], defined by their precisely delineated outer boundaries and enclosed internal voids, have garnered substantial research interest. Their unique morphology confers critical advantages: low mass density, elevated specific surface area, minimized charge/material transport distances, and high volumetric loading capacity for active components [10]. These intrinsic attributes render them highly attractive across diverse energy technologies.

Hollow materials are characterized by distinct internal/external interfaces and enclosed voids. Based on complexity, they are categorized as: Single-shell structures: A single shell enclosing a cavity. Multi-shell

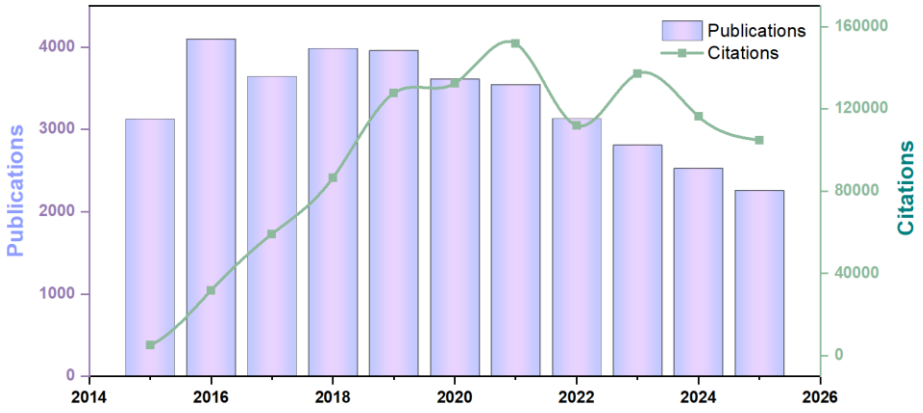

Figure 1 Number of citations and publications of research on hollow-structured materials in Web of Science over time.

structures: Multiple concentric shells forming independent chambers, attracting significant interest due to superior physicochemical properties [2, 11]. Their intricate, precisely controlled architecture often outperforms single-shell structures and bulk materials.

The synergy of low density, high porosity, and short transport pathways makes hollow structures pivotal for overcoming bottlenecks in energy storage and conversion, finding broad utility in fields like nanoreactors, catalysis, and fuel cells (**Scheme 1** illustrates key applications). Hollow architectures effectively mitigate detrimental volumetric expansion during electrochemical cycling and suppress polysulfide migration in lithium-sulfur systems. Their porous shells provide abundant active sites, enhance photon management, while multi-shell or hierarchical designs optimize mass transport pathways and boost energy density [10]. Consequently, they find extensive application in:

i) Lithium-ion batteries (LIBs): Provide abundant accessible storage sites, expanded electrode/electrolyte interfaces, shortened transport distances, and internal voids buffering volumetric expansion, enhancing specific capacity and cycling stability.

ii) Lithium metal anodes: Serve as hosts decreasing local current density, inhibiting Li dendrite growth, stabilizing the SEI, and restricting volume expansion [12].

iii) Lithium-sulfur (Li-S) batteries: Offer high pore volume for efficient sulfur loading. Heteroatom doping or heterojunction formation within the hollow architecture significantly enhances polysulfide anchoring and adsorption, mitigating the shuttle effect and improving capacity/cycle life [12, 13].

iv) Dye-sensitized solar cells (DSSCs): As photoanodes, enhance light harvesting via multiple internal reflections within the shell, enable high-density dye adsorption, facilitate electrolyte infiltration, and shorten charge transport distances [14].

v) Electrocatalysis: enable compartmentalization of distinct catalysts within sequential localized shells for cascade reactions. Shell pore structure and chemistry can be regulated to optimize reaction selectivity.

vi) Photocatalysis and photoelectrochemical: Provide large surface areas for catalytic sites, shorter charge carrier paths, and internal light-trapping effects for efficient photon collection [15].

For example, the HCT-x@Co_3O_4@SnS_2 core multi-shell structure features an inner conductive hollow carbon tube (HCT) core promoting electron transport and shortening ion diffusion. The outer Co_3O_4@SnS_2 layer leverages Co_3O_4 pseudo capacitance (Co^{2+}/Co^{3+} redox) and SnS_2 nanosheets providing abundant Faradaic reaction sites. This design achieves 63.5% capacity retention after 15, 000 cycles and enables flexible supercapacitors with an energy density of 40.22 $Wh \cdot kg^{-1}$ and power density of 750.22 $W \cdot kg^{-1}$ [16]. Similarly, “pomegranate-like” Si@C structures encapsulate nano-silicon within porous carbon microspheres, effectively mitigating silicon volume expansion and active material loss while enhancing areal capacity and volumetric energy density [17].

Substantial progress has been achieved in the synthesis and structural regulation of hollow materials, with established synthesis strategies broadly classified into three primary categories including hard templating, soft templating, template-free methods. This methodological diversity has directly enabled the development of hollow materials exhibiting extreme complexity in both composition and geometry (**Scheme 2**). Compositionally, they span single inorganic phases (oxides, sulfides, nitrides), organic polymers (e.g., polypyrrole, polyethylene terephthalate), and inorganic/organic hybrids (e.g., MOF-derived

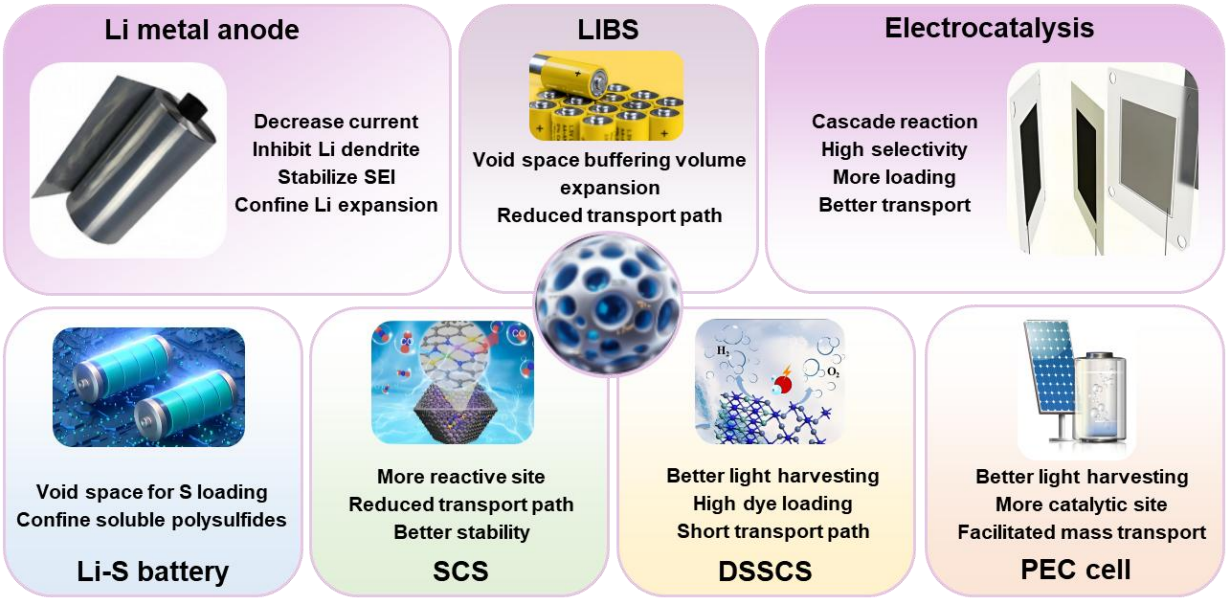

Scheme 1 Advantages of hollow nanostructures for energy storage applications.

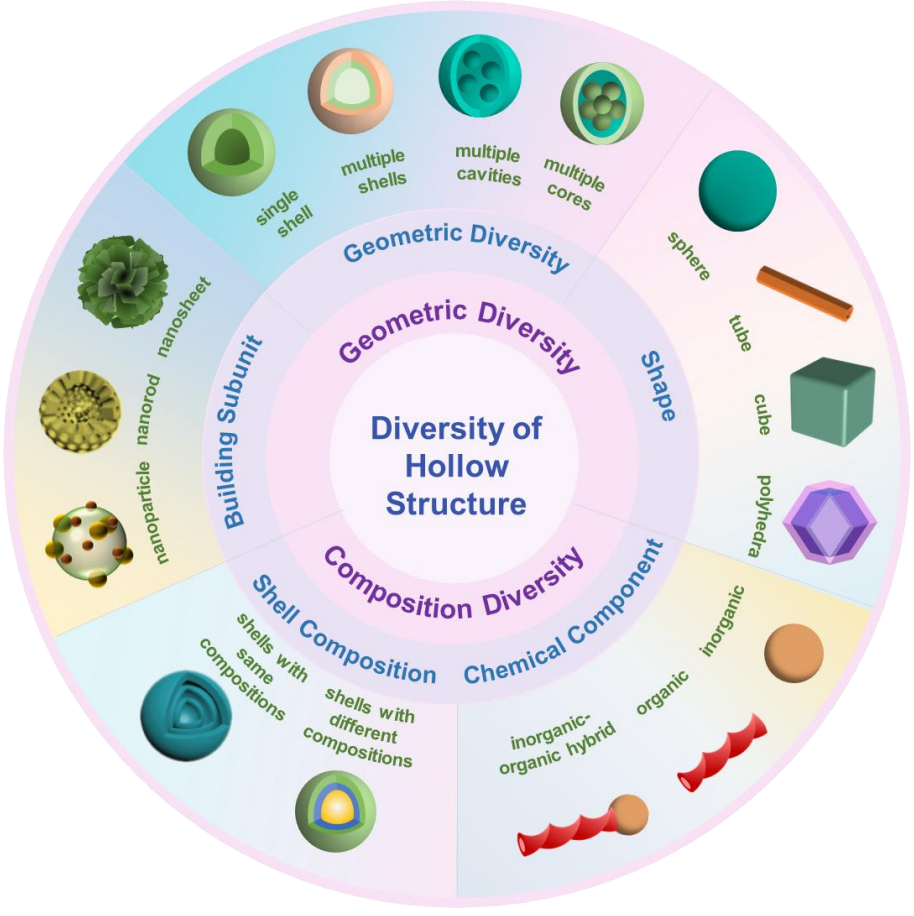

Scheme 2 Diversity of hollow structure.

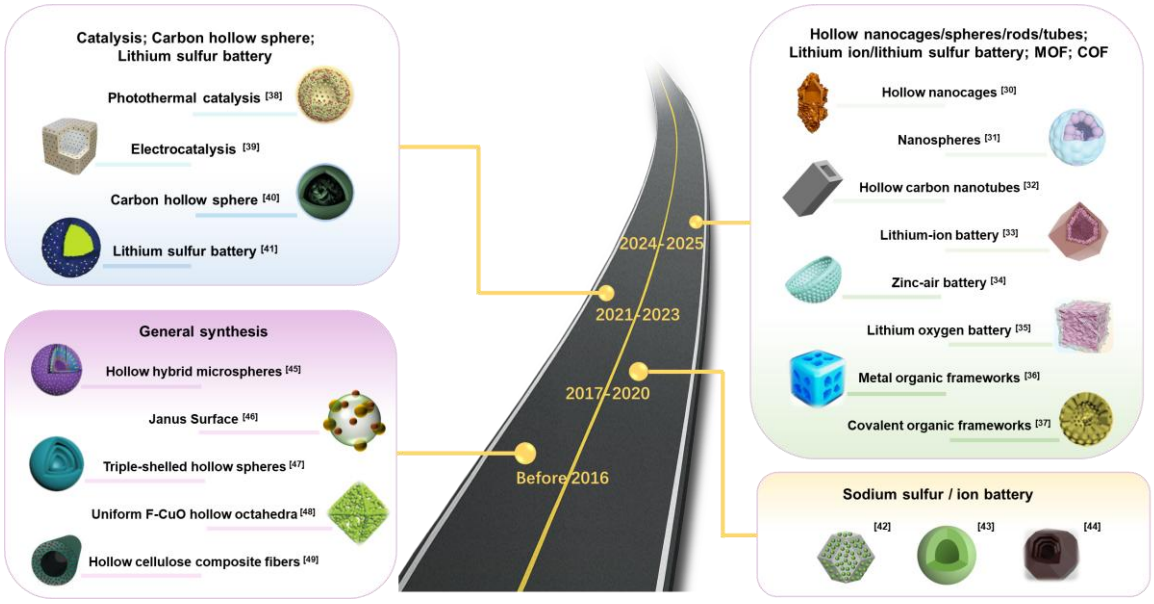

Scheme 3 A brief timeline of the development history of research on the synthesis and application of hollow-structured materials.

materials) [18-20]. Hybrid systems leverage synergistic effects and efficient electron transfer to optimize adsorption/desorption energetics of reaction intermediates (e.g., in electrocatalysis). Abundant heterogeneous interfaces induce charge redistribution, regulate electronic structure, lower activation barriers, and enhance catalytic activity. Furthermore, these structures combine stability with mass transfer advantages, suppressing nanoparticle aggregation while promoting electrolyte penetration [21]. Geometrically, beyond traditional spheres and tubes, diverse non-symmetrical configurations have been achieved (cubes, polyhedrons, prisms, bowls) [16, 22 -24]. Surface curvature control and interface reaction dynamics further refine these shapes. This multidimensional diversity enables precise performance optimization through structural and compositional engineering.

For instance, hierarchical aerogels integrating 3D spiral carbon nanowire coils, 2D reduced graphene oxide, 1D carbon nanofibers, and 0D Fe_3O_4@C core-shell particles create porous frameworks and gradient interfaces for enhanced microwave absorption [25]. Multi-shell/chamber structures (e.g., double-shell $CoMn_2O_4$ cubes [26]) synergistically enhance mechanical stability and interfacial reactivity. Chemically graded shells (e.g., magnetic Fe_2O_3/sub-black TiO_2 heterojunctions [27]) optimize charge separation via bandgap engineering. These examples illustrate how multidimensional design addresses specific energy challenges like electrode expansion and photo-generated carrier recombination.

Despite significant progress, the fundamental structure-performance relationships in hollow materials warrant deeper understanding. This review systematically dissects the correlation between hollow architectural features (composition, geometry, hierarchy) and their performance across key energy applications (LIBs, Li-S, SCs, photo/electrocatalysis). By analyzing representative design strategies, we elucidate the critical role of structural engineering in dictating function. Furthermore, prospective design methodologies are proposed to address current challenges and enhance the efficacy of hollow nanostructures in future energy storage, conversion, and generation technologies.

2. Synthesis Methods of Hollow Structures

The innovation and optimization of hollow structures synthesis methodologies constitute a major research focus in materials science. Based on core preparation principles, synthetic strategies are systematically categorized into two primary routes: template-assisted and template-free methods [48].

Template-assisted methods employ sacrificial molds for structural control: Hard templating utilizes rigid sacrificial templates (e.g., SiO_2, polystyrene microspheres, carbon). Precise control over shell thickness and cavity size is achieved via layer-by-layer

Table 1 Typical research contents related to hollow-structured materials in **Scheme 3**.

Year	Hollow structural materials type	Synthetic method	Ref.
2024-2025	Hollow nanocages	Template-free method	[30]
	Hollow nanospheres	Template-free method	[31]
	Hollow nanotubes	Template-free method	[32]
	Hollow core-shell dodecahedra	Hard template method	[33]
	Hollow bowl	Hard template method	[34]
	Hollow nanocage	Template-free method	[35]
	Hollow metal organic frameworks	Template-free method	[36]
	Hollow covalent organic frameworks	Soft template method	[37]
2021-2023	Hollow core-shell nanoparticles	Hard template method	[38]
	Hollow nanocubes	Hard template method	[39]
	Carbon hollow spheres	Hard template method	[40]
	Hollow microspheres	Hard template method	[41]
2017-2020	Hollow Janus-Featured	Hard template method	[42]
	Hollow nanospheres	Hard template method	[43,44]
Before 2016	Hollow hybrid microspheres through inward crystallization process	Template-free method	[45]
	Hollow carbon nitride structure with a Janus Surface	Hard template method	[46]
	Triple-shelled hollow spheres	Template-free method	[47]
	Uniform F-CuO hollow octahedra	Template-free method	[48]
	Hollow materials by fast pyrolysis of cellulose composite fibers	Template-free method	[49]

deposition followed by template removal. This method excels at producing multi-shell structures, as demonstrated by scalable sequential templating using carbon microspheres (CMS) to synthesize complex multi-shell hollow metal oxides in a single annealing step [49-51]. Soft templating employs dynamic assemblies (e.g., micelles, emulsions, bubbles, surfactant aggregates) to form cavities, facilitating the controlled synthesis of flexible organic or composite materials [52, 53].

Template-free methods exploit intrinsic material phenomena for cavity formation, including Ostwald ripening (driven by dissolution-reprecipitation kinetics), the Kirkendall effect (resulting from differential diffusion rates between core and shell materials), ion exchange (inducing structural rearrangement), and selective etching (removing a sacrificial component from a binary precursor), which approaches significantly simplify preparation by eliminating template constraints [54-56].

2.1 Hard Template Synthesis

Hard template method represents a foundational strategy for fabricating hollow architectures. This approach utilizes pre-formed, rigid sacrificial templates (e.g., inorganic or polymeric microspheres) as three-dimensional molds. The synthesis involves sequential deposition of target material precursors onto the template surfaces, followed by selective template removal, yielding defined hollow structures [57]. Renowned for its simplicity, versatility, and efficacy, this method is extensively employed for hollow nanostructure preparation. Templates are broadly categorized as inorganic (e.g., SiO_2, Al_2O_3) or organic/polymer (e.g., polystyrene (PS), polymethyl methacrylate (PMMA)).

Fundamental synthesis typically comprises four critical stages:

i) Template fabrication: Preparation of sacrificial templates with precise morphology and size control.

ii) Surface functionalization (optional): Modification of template surfaces to enhance interfacial adhesion with the target material. This step is circumvented if inherent compatibility exists between the template and the target precursor [11].

iii) Target material deposition: Controlled coating or deposition of the functional material onto the template surface. This stage is often the most technically demanding, requiring meticulous parameter optimization to achieve precise shell layer thickness and uniformity, which are paramount for structural integrity [17].

iv) Template removal: Selective elimination of the sacrificial template via chemical etching or thermal decomposition, resulting in the hollow architecture.

These strategies traces its origins to Caruso et al. (1998), who pioneered colloidal templating combined with layer-by-layer (LbL) self-assembly [58] (**Figure 2b**). PS microspheres served as templates. Charged polymers (e.g., PDDA, PSS) were alternately deposited to form a uniform pre-coating, facilitating subsequent electrostatic assembly of SiO_2 nanoparticles. Controlled deposition cycles regulated shell thickness. Calcination or solvent decomposition removed the PS core, yielding mesoporous SiO_2 hollow spheres with tunable cavities, valuable for applications like drug delivery and catalysis. Subsequent research expanded material scope and structural complexity.

Cui et al. synthesized SiMP@Gr yolk-shell structures by employed a dual-functional Ni template [59] (**Figure 2a**). Conformal Ni coating on Si microparticles acted as both a catalyst for low-temperature graphene nucleation/growth via dissolution-precipitation-assisted carbonization and a sacrificial buffer layer. Selective Ni etching ($FeCl_3$(aq)) created a mechanically flexible graphene cage. This structure enhances Si anode stability by: (1) buffering Si volume expansion while maintaining electrical contact; (2) suppressing electrolyte side reactions via an inert graphene interface, promoting stable SEI formation and reducing Li^+ consumption; (3) inhibiting Si particle pulverization via 3D confinement, achieving 90% capacity retention over 100 cycles in full cells.

SiO_2 nanofibers encapsulating silicon nanoparticles (Si NPs) were prepared by electrospinning a precursor solution containing tetraethyl orthosilicate (TEOS) and Si NPs, ultimately leading to the formation of SiO_2-templated Si@hollow carbon tubes [60] (**Figure 2c**). The SiO_2 layer served as substrate and spacer. Low-temperature polystyrene pyrolysis deposited a continuous carbon coating. Selective SiO_2 etching (HF(aq)) produced hollow carbon tubes containing Si NPs suspended within, buffering volume changes. The carbon shell stabilizes electrical contact and isolates Si from the electrolyte, stabilizing SEI formation.

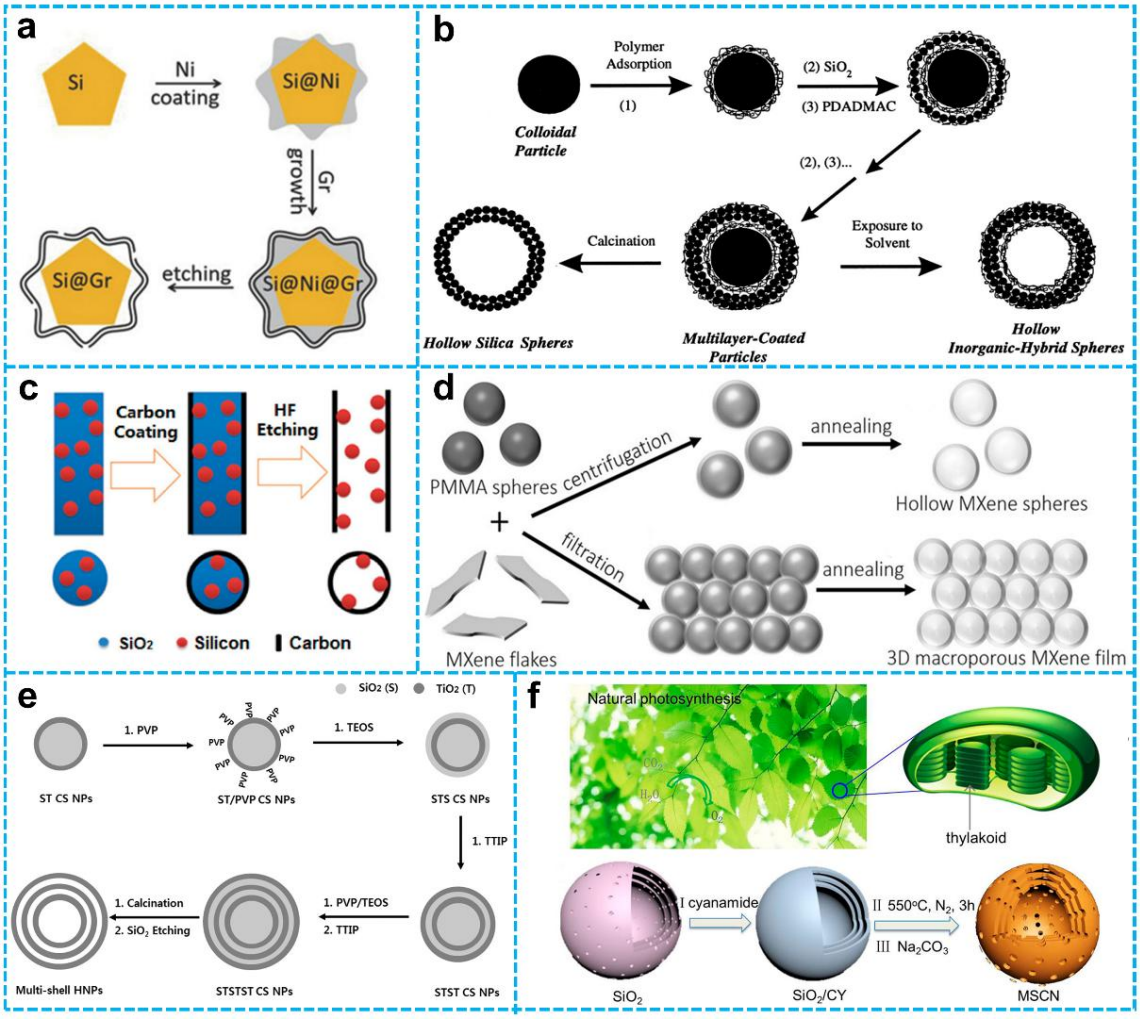

Figure 2 a) Schematic diagram of the synthesis of SiMP@Gr yolk-shell structure [59]. Copyright 2016, Springer Nature. b) Description of synthetic protocols for inorganic and hybrid hollow spheres [58]. Copyright 1998, The American Association for the Advancement of Science. c) Overview of the manufacturing of hollow carbon tubes encapsulated with Si nanoparticles [60]. Copyright 2012, American Chemical Society. d) Diagram illustrating the synthesis of hollow MXene spheres and MXene-Derived 3D macroporous frameworks [61]. Copyright 2017, John Wiley and Sons. e) Schematic illustration for the hard templating synthesis of TiO_2 TSHSs [62]. Copyright 2014, John Wiley and Sons. f) Schematic illustration for the hard templating synthesis of MSCN [63]. Copyright 2017, American Chemical Society.

PMMA spheres templated hollow MXene (e.g., $Ti_3C_2T_x$) structures [61] (**Figure 2d**) show MXene flakes, interacting via surface hydroxyl groups, spontaneously wrapped PMMA spheres. Centrifugation yielded MXene/PMMA composites. Argon annealing (450°C) thermally decomposed PMMA, forming multi-layered MXene hollow spheres with tunable wall thickness (via MXene:PMMA ratio). These structures exhibit excellent dispersibility and potential in environmental and biomedical applications. The method demonstrates universality for other MXenes (e.g., V_2CT_x, Mo_2CT_x).

This hard template methods versatility extends to synthesis of complex multi-shell hollow structures (MSHSs) via sequential deposition of functional shell components and removable intermediate layers onto the initial template, followed by differential etching [49].

Jang et al utilized Stöber SiO_2 spheres as the core template to synthesis TiO_2 multi-shell hollow spheres [62] (**Figure 2e**). Alternating TiO_2 and SiO_2 layers were deposited via sol-gel processing, constructing core-shell composites (e.g., single-, triple-, quintuple-layer). High-temperature calcination removed organics, followed by alkaline etching to remove all SiO_2 components, yielding TiO_2 hollow spheres with single- (SSHS), double- (DSHS), or triple-shell (TSHS) structures.

Tong et al. employed pre-synthesized multi-shell SiO_2 nanospheres as templates to form multi-shell g-C_3N_4 (MSCN) nanocapsules [63] (**Figure 2f**). Cyanamide (CY) precursor infiltrated the mesopores and cavities of the SiO_2 shells, adsorbing onto the shell surfaces. Thermal polymerization (550°C) formed SiO_2/g-C_3N_4 composites. Sequential addition of TEOS/BTME mixtures and thermal processing built up SSHS, DSHS, or TSHS composite structures. Final Na_2CO_3(aq) etching removed the SiO_2 template, yielding MSCN nanocapsules with a hollow core and multi-layered mesoporous shell.

2.2 Soft Template Synthesis

The soft template method is a synthetic technique for synthesizing hollow structures, utilizing dynamic self-assembling molecules—surfactants, block copolymers, micelles, or vesicles as structural templates. This approach exploits the thermodynamically metastable assemblies formed by amphiphilic molecules in solution (e.g., micelles, vesicles, or emulsion droplets) to direct the oriented deposition of target materials onto the template surface. Subsequent removal of the soft template yields the final hollow architecture [64-70].

Unlike hard templating, which relies on pre-synthesized rigid structures (e.g., SiO_2 or polystyrene spheres), the soft template method employs inherently dynamic templates. These templates form *in situ* during the reaction via spontaneous self-assembly driven by intermolecular non-covalent interactions, such as hydrophobic effects and hydrogen bonding. This dynamic nature provides significant flexibility for controlling critical structural parameters of the resultant hollow materials, including shell layer number, porosity, and overall morphology. Consequently, soft templating is particularly well-suited for synthesizing complex architectures featuring multi-level porosity or flexible frameworks [52].

The assembly behavior of soft templates is highly sensitive to synthetic parameters, including temperature, solvent polarity, pH, amphiphilic molecule concentration, ionic strength, and the presence of organic/inorganic additives. Theoretically, this parameter dependence offers a pathway for precise morphological control over micellar/vesicular templates, enabling regulation of template size, packing density, and interfacial properties through manipulation of the solution environment. However, in practice, the complexity of multi-component reaction systems poses significant challenges to template stability. The introduction of target precursors (e.g., metal salts, silicon sources, or carbon sources) can disrupt the dynamic equilibrium of micelles/vesicles through competitive adsorption, potentially leading to template deformation or disintegration. This instability has historically limited the broad applicability of soft templating for synthesizing multi-component and heterogeneous materials.

Despite these challenges, researchers have developed strategies as precursor-template cooperative assembly, enabling breakthrough syntheses of multi-shelled hollow structures (MSHS) across diverse material classes, including silica, metal oxides, and sulfides.

Within the domain of photocatalytic materials research, Guo et al. synthesized surface sulfur-vacancy-rich hollow $ZnIn_2S_4$ nanocages (ZIS-HNCs) via soft templating. These structures form robust interfaces with $NiCo_2S_4$ (NCS), facilitating efficient transfer and accumulation of photo-generated electrons on the NCS surface (**Figure 3a**). The hollow architecture enhances light absorption via multiple scattering, while sulfur vacancies promote electron accumulation and consumption. This synergy excites photo-generated electrons in NCS into long-lived hot electrons, culminating in a remarkable visible/near-infrared photocatalytic hydrogen production rate of 19, 654.0 $\mu mol \cdot g^{-1} \cdot h^{-1}$ (**Figure 3b**), an apparent quantum efficiency of 56.7% at 400 nm (**Figure 3c**), and a reduced apparent activation energy (from 49.6 $kJ \cdot mol^{-1}$ to 32.2 $kJ \cdot mol^{-1}$, **Figure 3d**) [52].

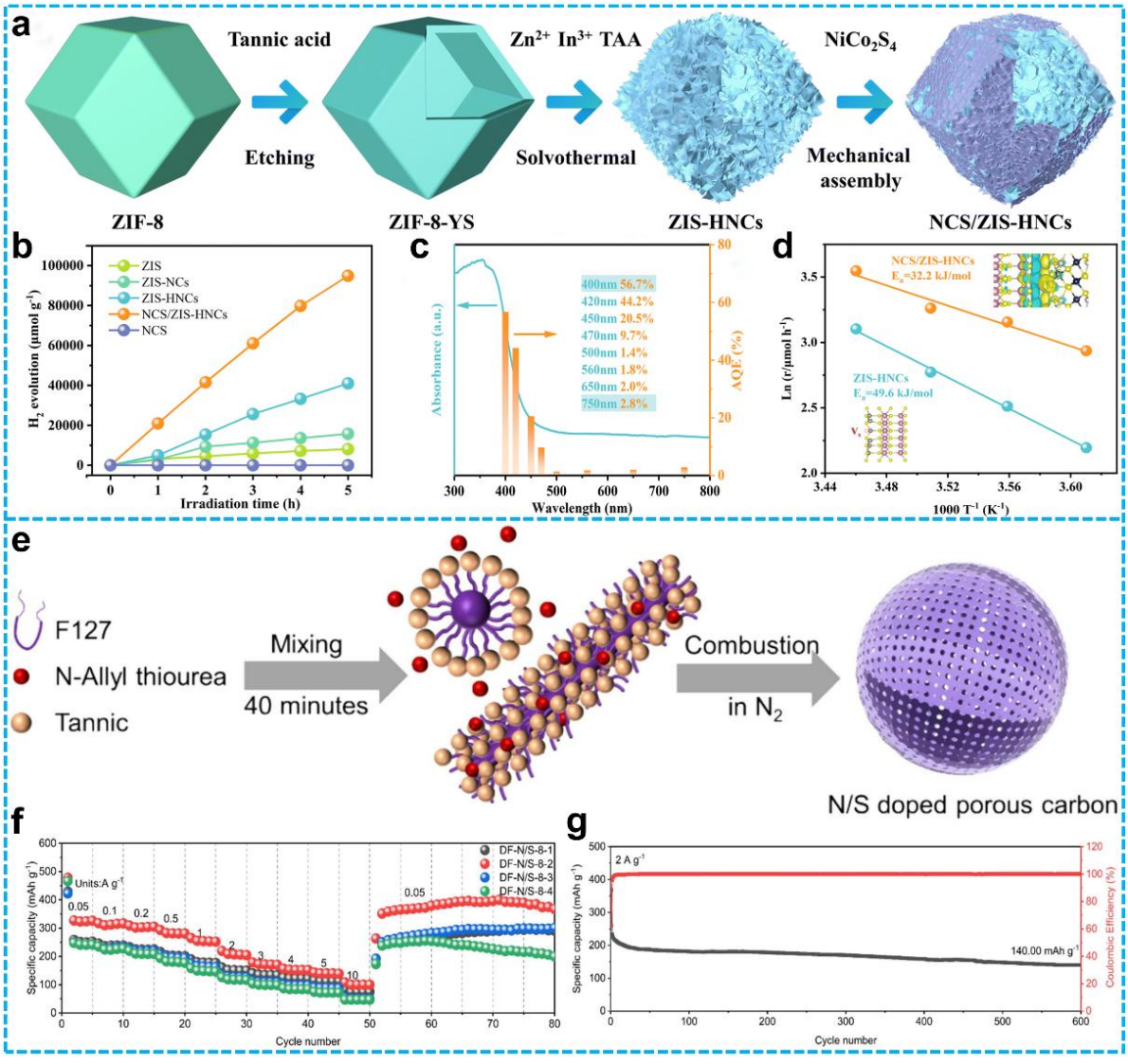

Figure 3 a) Schematic illustration of the fabrication pathway for NCS/ZIS-HNC heterostructures; Photocatalytic hydrogen evolution (PHE) performance of the prepared samples; c) Apparent quantum efficiency (AQE) and diffuse reflectance spectroscopy (DRS) spectral data for NCS/ZIS-HNCs; d) Temperature-dependent PHE rate analysis of ZIS-HNC and NCS/ZIS-HNC materials [52]. Copyright 2023, Royal Society of Chemistry. e) Schematic diagram of the synthetic procedures for DF-N/S-8-2; f) Rate capability at different doping levels; g) Cycling stability tested at a current density of 2 $A \cdot g^{-1}$ [53]. Copyright 2024, Elsevier.

In battery anodes research, Zhang et al. employed a soft-template-induced self-assembly strategy using biomass-derived tannic acid as a precursor, Pluronic F127 as the template, and N-allyl thiourea as a dopant to synthesize N/S co-doped porous carbon spheres (DF-N/S) (**Figure 3e**). As a sodium-ion battery anode in an ether-based electrolyte, DF-N/S delivers a high specific capacity of 327.04 $mA \cdot h \cdot g^{-1}$ at 0.05 $A \cdot g^{-1}$ (**Figure 3f**) and maintains 140 $mA \cdot h \cdot g^{-1}$ after 600 cycles at 2 $A \cdot g^{-1}$ (**Figure 3g**). Its exceptional performance is attributed to the porous structure facilitating Na^+ transport, N/S doping increasing active sites, and the formation of a thin SEI layer with rapid Na^+ diffusion kinetics in the ether-based electrolyte [53].

In silica-based systems, silica and its derivatives represent highly successful applications of soft templating, benefiting from the precise control over silicon precursor hydrolysis and condensation in aqueous solutions. Zhang et al. utilized Pluronic P85 triblock copolymer as a single template, adjusting synthesis pH (4.8-5.5) to achieve controlled preparation of organic silica-based multilamellar vesicles. This mild system

produces vesicles in high yield (> 90%), with wall layer count tunable from seven to a single layer. The vesicle walls feature a 6 nm mesoporous sponge-like structure, exhibiting a high specific surface area (695 $m^2 \cdot g^{-1}$) and large pore volume (2.10 $cm^3 \cdot g^{-1}$) [71]. Liu et al. employed vesicular templates formed by co-assembly of FC4/F127 dual surfactants. By controlling the template ratio and reaction conditions (pH 9.8-12.2), they synthesized mesoporous silica hollow spheres with uniform size and tunable shell layers. Ethanol content and ammonia addition allowed precise control over shell number, thickness, and meso-porosity. The resulting material demonstrated specific adsorption capacity for methylene blue (25 $mg \cdot g^{-1}$) and high drug loading/release capabilities (e.g., 448 $mg \cdot g^{-1}$ ibuprofen) [68].

2.3 Template-Free Synthesis

2.3.1 Selective Etching

Selective etching is a synthetic strategy for constructing hollow structures by exploiting inherent chemical property differences within a material to selectively remove specific regions via chemical dissolution, eliminating the requirement for external templates. The core principle involves precise control of etching conditions to preferentially dissolve chemically less stable ("soft") regions while preserving more stable ("hard") regions, which subsequently act as structural supports. This intrinsic self-etching mechanism, proceeding from the interior outwards, circumvents the limitations of traditional template-based methods and provides a versatile pathway for the controlled synthesis of complex multi-shell architectures.

Conceptually, the selective etching process for generating hollow materials resembles the template removal step in hard templating [72]. Yet a critical distinction lies in the initial template: as it possesses homogeneous composition and structure, creating a differential in solubility or chemical stability between the inner and outer regions is essential. This differential susceptibility enables targeted etching leads two primary approaches upon this:

Surface-protected etching utilizes a stabilizer coating to protect the outer shell surface, confining the etchant action to the interior [72, 73]. For instance, Liang et al. demonstrated this by forming a protective polyvinylpyrrolidone (PVP) layer on silica spheres. This confined the NaOH etchant action predominantly within the sphere core, generating a mesoporous structure. This modification significantly enhanced the material's specific surface area (161.1357 $m^2 \cdot g^{-1}$) and pore volume (0.5591 $cm^3 \cdot g^{-1}$). Furthermore, the resulting quantum confinement effect facilitated the uniform dispersion of Fe_3O_4 nanoparticles, increasing the iron loading to 32.67 wt% (approximately double that of the unetched material). Enhanced surface wettability, evidenced by a reduced water contact angle (from 43.6° to 21.24°), further optimized interaction efficiency between the catalyst and pollutants [74].

Intrinsic stability gradients approach leverages differential chemical stability inherently formed during the initial template synthesis. Regions with lower stability ("soft" regions) are selectively etched, while higher stability ("hard" regions) remain intact. Wang et al. exemplified this strategy by utilizing the alkaline etching effect of ethylenediamine (EDA) under template-free hydrothermal conditions. EDA preferentially etched the inner core of amorphous titanium dioxide spheres, characterized by low polymerization degree. Concurrently, the outer, highly crystalline titanium dioxide layer resisted etching, forming a porous shell. Complete dissolution of the inner core resulted in hollow cavities. The addition of NaCl further modulated the oriented assembly of hydrated titanium oxide nanosheets into layered hollow microspheres [75]. Similarly, Cheng et al. developed a solvent-selective etching strategy for carbon microspheres. Following phenolic resin microsphere formation, acetone dissolved the low-molecular-weight oligomers within the core, while the highly cross-linked outer shell remained intact. This template-free process yielded multi-chamber mesoporous carbon microspheres (MCMCs). Crucially, the number of internal pores and mesopore distribution could be precisely tuned by varying the acetone volume (20-80 mL), with an optimized hierarchical pore structure achieved at 60 mL [76].

2.3.2 Ostwald Ripening

Ostwald ripening, a phenomenon driven by disparities in crystal surface energy, describes the spontaneous dissolution of smaller, higher-surface-energy nanocrystals and the subsequent redeposition of the dissolved material onto larger crystals [55]. This self-organizing mechanism offers distinct advantages for the template-free synthesis of hollow structures. By manipulating the dissolution-recrystallization equilibrium, it facilitates the in-situ transformation of solid nanoparticles into hollow architectures, circumventing the complexities associated with template preparation and removal. This approach is particularly effective for metal oxide systems exhibiting significant solubility variations as Co_3O_4 [77], Mn_3O_4 [78], and TiO_2 [79].

Research demonstrates that multi-step Ostwald ripening strategies enable the precise construction of multi-shell structures [80]. For instance, Zhang et al. achieved controlled structural evolution in nanospheres

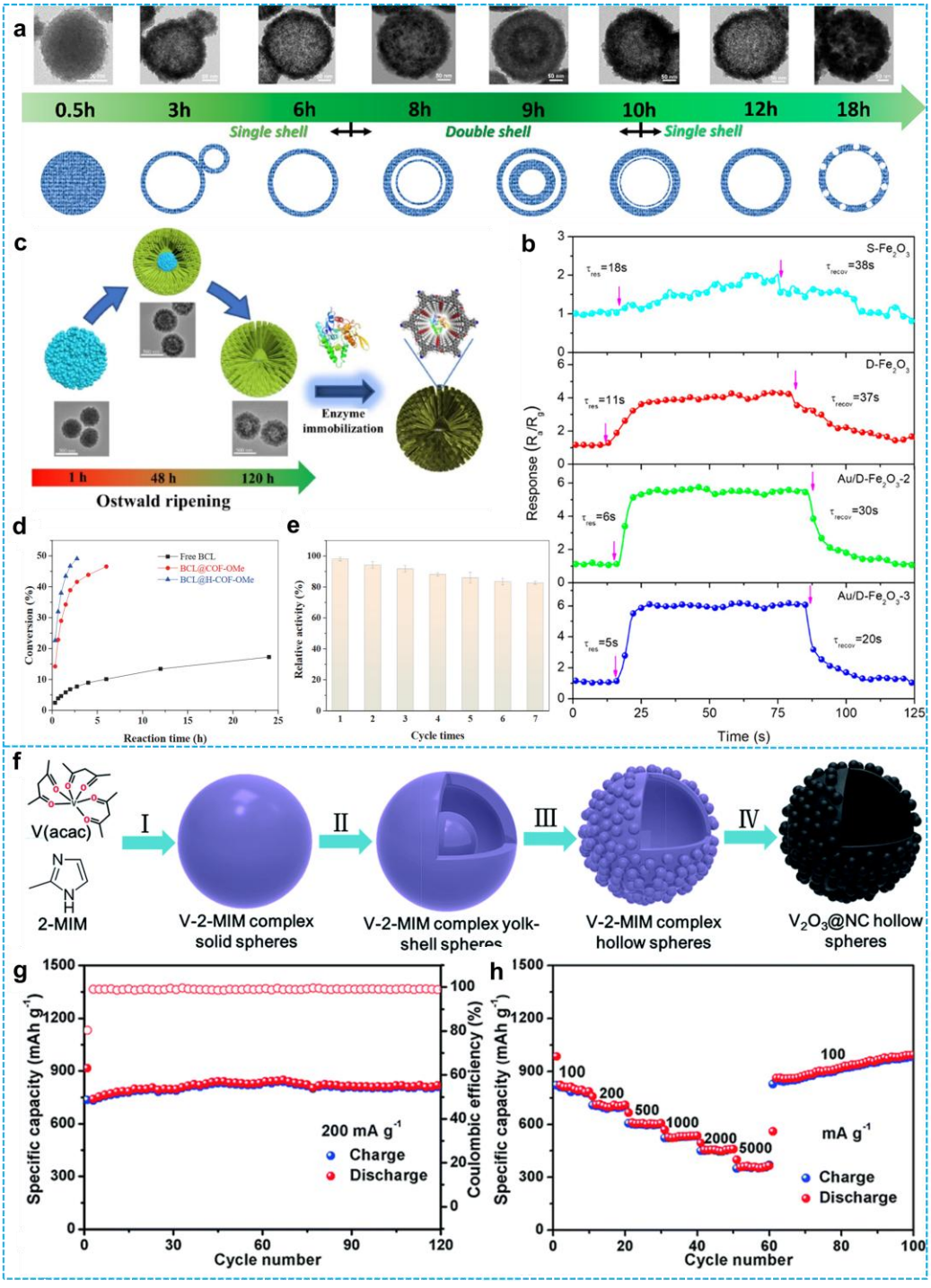

Figure 4 a) Structural evolution of Fe_2O_3 spheres as a function of reaction duration; b) Dynamic response profiles of four gas sensors to 10 ppm acetone at 200°C [81]. Copyright 2019, American Chemical Society. c) Self-template method for preparing hollow lipase (BCL@H-COF-OMe) via Ostwald ripening mechanism; d) Comparison of catalytic performance of different catalysts for kinetic resolution of l-phenyl ethanol; e) Recycling catalytic performance tests of BCL@H-COF-OMe for kinetic resolution of 1-phenylethanol [55]. Copyright 2022, Springer Nature. f) Schematic representation of the formation process for uniform V_2O_3@NC hollow spheres; g) Cycling stability at a low current density of 200 mA·g^{-1}; h) Rate capability at current densities of 100, 200, 500, 1000, 2000, 5000, and back to 100 mA·g^{-1} [82]. Copyright 2018, Royal Society of Chemistry.

by precisely regulating hydrothermal reaction time (0.5-18 hours) (**Figure 4a**): i) Initial stage (0.5 h): Formation of solid nanoparticles. ii) Intermediate stage (1-6 h): Internal-to-external Ostwald ripening yields a single-shell structure. iii) Shell formation stage (7-10 h): External-to-internal ripening drives dissolved nanoparticle redeposition onto the inner surface, forming a double-shell structure. iv) Late stage (> 10 h): Gradual dissolution of the inner shell reverts the structure to a single shell.

This entirely template-free process relies solely on the dissolution-redeposition mechanism governed by nanoparticle surface energy gradients: material dissolves preferentially from high-energy regions, diffuses through pores, and recrystallizes in low-energy regions. The dynamic equilibrium allows precise temporal control over shell number with high reproducibility. The resulting double-shell structure exhibits enhanced specific surface area and porosity. Loading with Au nanoparticles (Au/D-Fe_2O_3) leverages synergistic structural and catalytic sensitization, achieving a remarkably low acetone detection limit (0.132 ppm), rapid response time (5 s), high sensitivity (0.465 ppm^{-1}), and selectivity (**Figure 4b**). This methodology overcomes limitations of conventional templating and provides novel design principles for high-performance gas sensors [81].

Liu et al. applied Ostwald ripening to the large-scale synthesis of hollow covalent organic frameworks (COFs) for biocatalysis. Self-assembly of TAPB and DMTA monomers in acetonitrile/acetic acid initially forms solid microspheres (1-12 h). Subsequent internal dissolution-reprecipitation via Ostwald ripening progressively evolves these into an eggshell structure (24-72 h), culminating in uniform hollow spheres (diameter: 580 nm; shell thickness: 122 nm) (**Figure 4c**). Immobilizing Burkholderia cepacia lipase (BCL) on these hollow COFs (BCL@H-COF-OMe) significantly enhanced its thermal stability, tolerance to polar organic solvents, and reusability. In the kinetic resolution of secondary alcohols, BCL@H-COF-OMe outperformed both non-hollow COF-immobilized and free enzymes, achieving a maximum conversion of 49.12% (**Figure 4d**). Furthermore, BCL@H-COF-OMe retained high activity over multiple cycles with only a slight decrease in relative activity (**Figure 4e**), demonstrating excellent reusability while maintaining enantiomeric excess (ee) > 99% [55].

Han et al. utilized solvothermal Ostwald ripening to achieve morphological evolution from solid microspheres to hollow spheres (**Figure 4f**): i) Initial stage (3 h): Formation of solid V-2-MIM composite microspheres. ii) Intermediate stage (6 h): Internal dissolution and outer shell recrystallization transform the structure into an eggshell morphology. iii) Final stage (12 h): Complete core consumption yields uniform nitrogen-doped carbon-coated V_2O_3 hollow spheres. Driven by minimization of the system's Gibbs free energy, material preferentially dissolves from low-curvature regions, diffuses through solution, and precipitates onto external high-curvature regions, promoting shell densification. This spontaneous mechanism eliminates the complex steps of traditional templating, producing submicron-scale hollow structures (~200 nm diameter, ~30 nm shell thickness) composed of tightly packed nanoparticles. These structures provide an ideal foundation for carbon-coated metal oxide hollow materials. As a lithium-ion battery anode, this material exhibited high initial discharge capacity (915 $mA{\cdot}h{\cdot}g^{-1}$, **Figure 4g**), excellent rate capability (361 $mA{\cdot}h{\cdot}g^{-1}$ at 5000 $mA{\cdot}g^{-1}$, **Figure 4h**), and outstanding long-term cycling stability (472 $mA{\cdot}h{\cdot}g^{-1}$ retained after 700 cycles at 2000 $mA{\cdot}g^{-1}$, exceeding 100% retention). The unique hollow structure combined with the carbon coating effectively shortens ion diffusion paths, enhances electrical conductivity, and buffers volume changes during cycling [82].

2.3.3 Kirkendall Effect

The Kirkendall effect describes the phenomenon where an imbalance in the mutual diffusion rates of two substances across an interface leads to vacancy formation. Specifically, the preferential outward diffusion of faster-migrating metal atoms creates vacancies that slower-diffusing atoms cannot adequately replenish. This net vacancy flux ultimately results in pore formation and coalescence into hollow structures within the material. This mechanism provides a fundamental theoretical basis for the template-free synthesis of nanoscale hollow structures. Such synthesis obviates the need for pre-designed templates, instead achieving directed cavity formation solely through the control of diffusion kinetics. Crucially, the approach is applicable to diverse material systems, including metals, oxides, and sulfides [83].

Chu et al. successfully synthesized hollow NiO nanoparticles via a Kirkendall-effect-driven template-free method [84]. Their approach involved: i) Precursor synthesis: Preparation of Ni/C nanocomposites using a molten salt calcination method (**Figure 5a**). ii) Oxidation and hollowing: Secondary calcination in air, where Ni nanoparticles act as sacrificial precursors. During oxidation, Ni^{2+} ions diffuse outward significantly faster than O^{2-} ions diffuse inward (the nanoscale Kirkendall effect). This asymmetric diffusion creates a concentration gradient between the metal core and the

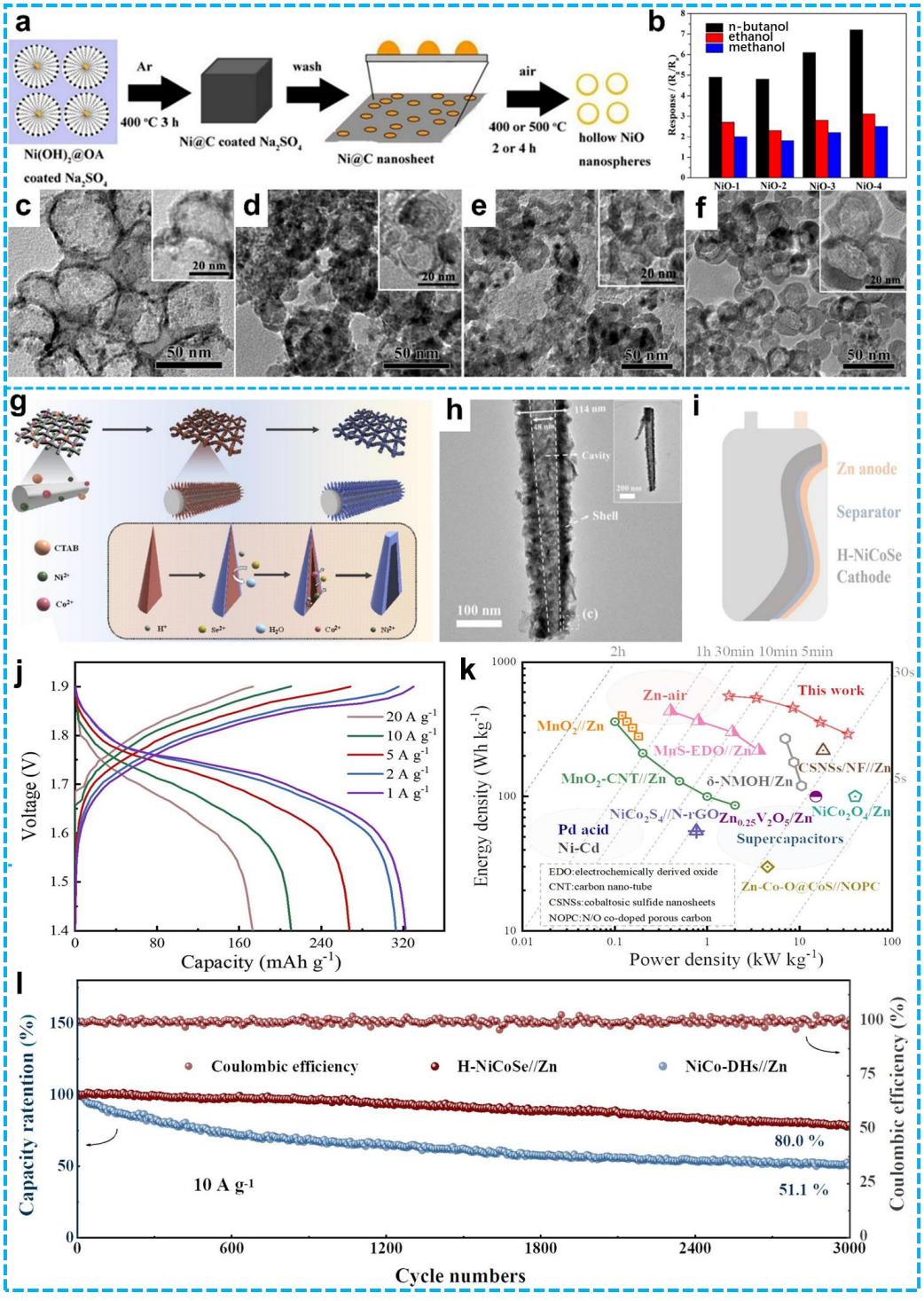

Figure 5 a) Schematic diagram of hollow NiO nanosphere synthesis procedures; b) Selectivity of four NiO-based sensors toward 800 ppm target gases at 240°C; TEM images of (c) NiO-1; (d) NiO-2; (e) NiO-3; (f) NiO-4. The inset images show cross-sectional TEM views of hollow NiO nanospheres [84]. Copyright 2019, Elsevier. g) Diagram depicting the synthesis route of H-NiCoSe@CC nanoarrays; h) TEM image of the prepared H-NiCoSe nanoarrays; i) Schematic representation of a flexible full battery using H-NiCoSe as the cathode and zinc metal as the anode; j) Galvanostatic charge-discharge (GCD) profiles of the H-NiCoSe//Zn battery at various current densities; k) Ragone plots for the H-NiCoSe//Zn battery; l) Cycling performance of the as-assembled H-NiCoSe//Zn and NiCo-DHs//Zn batteries at a current density of 10 A·g^{-1} [54]. Copyright 2023, Elsevier.

forming oxide shell, driving vacancy accumulation and the eventual formation of a central void.

Systematic variation of calcination temperature (400-500 ℃) and duration (2-4 h) enabled control over the crystallinity and morphology of the resulting hollow structures. Transmission electron microscopy (TEM) analysis revealed the significant influence of heat treatment parameters: NiO-1 (**Figure 5c**): Exhibited polydisperse hollow spheres (~40 nm avg. diameter) with a wide size distribution. NiO-2 (**Figure 5d**) and NiO-3 (**Figure 5e**): Evolved into more uniform spherical hollow structures (~20 nm diameter). Their shells comprised disordered stacks of 10-15 nm nanoparticles, creating a porous assembly that substantially increased the specific surface area. NiO-4 (**Figure 5f**): Displayed highly symmetrical hemispherical hollow cavities (consistent ~20 nm diameter). Multi-angle TEM confirmed a preferred orientation arrangement of the shell nanoparticles.

Notably, the NiO-4 hollow structure demonstrated excellent gas sensing performance at 240 °C, exhibiting high sensitivity (R_g/R_a = 9.0) and selectivity towards 1000 ppm n-butanol (**Figure 5b**). This performance is attributed to the thin, porous outer shell facilitating efficient gas diffusion and electron transport, highlighting a novel design strategy for functional hollow nanomaterials [84].

Gao et al. developed a related template-free strategy, leveraging the Kirkendall effect to fabricate hollow bimetallic selenide electrodes [54]. Their methodology comprised: i) Precursor fabrication: Growth of NiCo bimetallic hydroxide (NiCo-DHs) nanoneedle arrays on carbon cloth (CC) via hydrothermal synthesis (**Figure 5g**). ii) Selenidation and hollowing: Reaction with H_2Se gas, where surface hydroxides react to form an initial $Ni_3Se_4/CoSe_2$ shell layer. Crucially, asymmetric diffusion occurs: Se^{2-} anions diffuse inward to bind metal cations, while Ni^{2+}/Co^{2+} cations migrate outward to form new selenide phases at the surface. This preferential loss of internal metal ions due to their faster outward diffusion drives vacancy supersaturation and cavity formation within the nanostructure (**Figure 5h**).

This ion-diffusion-rate-based Kirkendall effect successfully yielded self-supporting hollow bimetallic selenides (H-NiCoSe/CC) directly on carbon cloth, serving as cathodes for aqueous zinc-based batteries (AZBBs) (**Figure 5i**). The template-free, asymmetric diffusion strategy avoids the cumbersome steps of traditional templating methods and eliminates "dead volume" issues associated with polymeric binders. The H-NiCoSe/CC cathode exhibited exceptional electrochemical performance: i) High specific capacities: 405.8 $mA·h·g^{-1}$ at 1 $A·g^{-1}$; 300.2 $mA·h·g^{-1}$ at 30 $A·g^{-1}$ (**Figure 5j**). ii) High energy density in a flexible full cell: 557.0 $Wh·kg^{-1}$ (**Figure 5k**). iii) Excellent cycling stability: 80% capacity retention after 3, 000 cycles (**Figure 5l**). This work presents a viable new strategy for designing high-performance energy storage devices [54].

Beyond these specific examples, the Kirkendall effect offers a versatile design principle for synthesizing hollow nanostructures in numerous other material systems, including NiO, CuO, PtCu, etc. [85, 86].

2.3.4 Ion Exchange

Ion exchange represents a pivotal strategy for synthesizing hollow nanostructures. Its fundamental mechanism relies on the directed replacement of lattice ions in a solid precursor with ions from the solution phase, inducing controlled reconstruction of composition and morphology. This process leverages the chemical potential gradient between specific metal cations or anions within the precursor and the introduced ionic species in the reaction medium. The resulting diffusion-controlled ion transport facilitates compositional transformation and structural evolution, culminating in hollow architectures [87].

Li et al. utilized a template-free methodology to synthesize hollow microplate-like $CoMoO_4$ structures via ion exchange [88]. Initially, cobalt-based metal-organic framework (Co-MOF) microplate arrays were fabricated on a nickel foam (NF) substrate solvothermally, serving as the precursor. Subsequent hydrothermal ion exchange involved the gradual replacement of BDC^{2+} organic ligands within the Co-MOF by MoO_4^{2-} anions from solution. During this exchange, MoO_4^{2-} combined with Co^{2+} to form an ultrathin $CoMoO_4$ nanolayer shell, while the Co-MOF core was concurrently consumed. This process yielded ultrathin nanolayer-assembled hollow microplate arrays ($CoMoO_4$-HMPA/NF) (**Figure 6a, b**). Electrochemical characterization revealed that the $CoMoO_4$-HMPA/NF electrode exhibited ultra-high specific capacitance (12.2 $F·cm^{-2}$, 6120 $C·cm^{-2}$ at 2 $mA·cm^{-2}$), excellent rate performance (82.2% retention at 50 $mA·cm^{-2}$), and cycling stability (90.5% capacity retention after 5000 cycles) (**Figure 6c, d**). Asymmetric supercapacitors (ASCs) assembled using this electrode delivered an energy density of 0.321 $mWh·cm^{-2}$ (**Figure 6e**) and exceptional cycling stability (96.0% capacity retention after 5000 cycles) (**Figure 6f**), demonstrated by successfully powering a blue LED, underscoring its practical potential [88].

Xu et al. synthesized multicomponent $CoSe_2/FeSe_2$ double-shell hollow nanocubes (DS-HNCs) as an efficient catalyst (**Figure 6g-i**) [56]. Solid-state cobalt precursor nanocubes served as templates. Room-

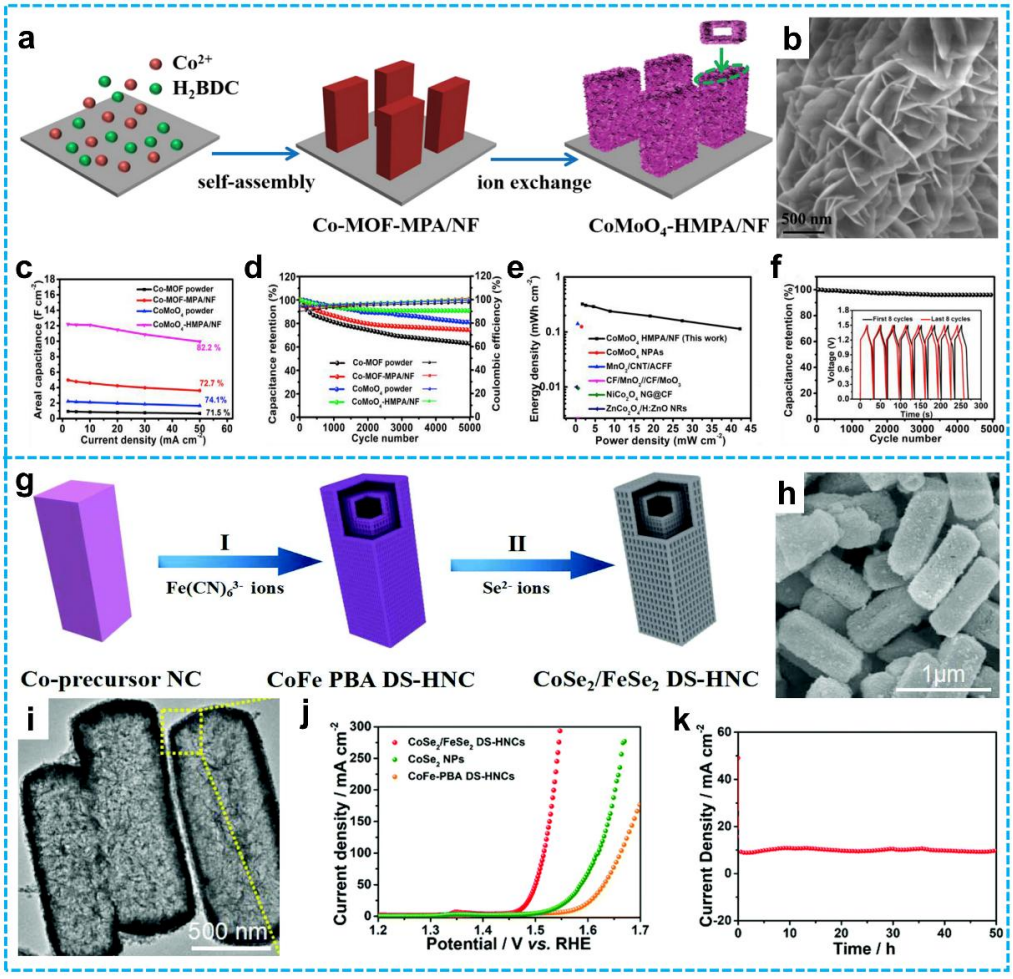

Figure 6 a) Schematic illustration of the synthesis process for $CoMoO_4$-HMPA/NF composite; b) SEM images of $CoMoO_4$-HMPA/NF; c) Areal capacitances versus current densities; d) Cycling performance and coulombic efficiency comparisons among $CoMoO_4$-HMPA/NF, $CoMoO_4$ powder, Co-MOF-MPA/NF, and Co-MOF powder; e) Energy and power density plots of the $CoMoO_4$-HMPA/NF//AC asymmetric supercapacitor (ASC), alongside literature data; f) Cycling stability of the $CoMoO_4$-HMPA/NF//AC ASC device [88]. Copyright 2019, Elsevier. g) Schematic diagram depicting the stepwise ion exchange strategy for synthesizing $CoSe_2/FeSe_2$ DS-HNCs; h) SEM, i) TEM images of the as-obtained $CoSe_2/FeSe_2$ DS-HNCs; j) LSV curves for OER testing of $CoSe_2/FeSe_2$ DS-HNCs, $CoSe_2$ NPs and CoFe-PBA DS-HNCs; k) Chronoamperometric response of $CoSe_2/FeSe_2$ DS-HNCs at a constant potential of 1.47 V [56]. Copyright 2019, Royal Society of Chemistry.

temperature ligand exchange first produced a mesoporous double-shell hollow intermediate, $Co_2[Fe(CN)_6]$. Subsequent selenium ion exchange yielded the target $CoSe_2/FeSe_2$ DS-HNCs. The synergistic effect between the unique double-shell hollow nanostructure and high-oxidation-state Co^{3+} species endowed the material with exceptional oxygen evolution reaction (OER) performance in 1M KOH. Notably, it achieved a current density of 10 $mA \cdot cm^{-2}$ at a low overpotential of 240 mV (**Figure 6j**) and demonstrated electrochemical durability exceeding 50 hours (**Figure 6k**), significantly surpassing single-component selenides and some precious-metal benchmarks. This work provides a novel strategy for designing multicomponent, precious-metal-free electrocatalysts and highlights the critical roles of double-shell hollow architectures and high-oxidation-state species in enhancing OER kinetics and stability [56].

Beyond binary systems, more intricate multishell structures are accessible through ion exchange strategies. Guan et al. demonstrated this using a stepwise approach [89]. Onion-like Co_3O_4 served as the precursor. An initial anion exchange reaction converted it into onion-like Co_4S_3. A subsequent cation exchange reaction then

yielded onion-like hollow-structured nickel-cobalt sulfide ($NiCo_2S_4$) particles. When evaluated as battery electrodes, these particles exhibited high specific capacitance (1016 $F \cdot g^{-1}$ at 2 $A \cdot g^{-1}$) and excellent cycling stability (87% capacity retention after 10, 000 cycles). Hybrid supercapacitors (HSCs) constructed with $NiCo_2S_4$ as the positive electrode and activated carbon as the negative electrode delivered an energy density of 42.7 $Wh \cdot k \cdot g^{-1}$ and outstanding cycling stability (only 8% capacity degradation after 10, 000 cycles). This performance is attributed to the complex multishell hollow architecture, coupled with the high specific surface area and conductive active sites provided by the nickel-cobalt composite [89].

2.3.5 Thermally Induced Matter Repositioning

Thermally induced material repositioning (TIMR) represents a versatile and directed synthesis strategy for hollow structures, exploiting the controlled non-equilibrium shrinkage behavior of materials during high-temperature processing [90]. The core mechanism arises from temperature gradients generated during the thermal decomposition of precursor components, which drive directional mass transport. Specifically, when metal-organic or inorganic composite precursors undergo heating, decomposition of organic/inorganic constituents releases gaseous products. An initial metal oxide shell forms, constraining contraction of the outer region, while the incompletely decomposed inner core experiences heterogeneous shrinkage under continued thermal exposure. This differential shrinkage ultimately leads to shell detachment, forming multi-shell architectures.

A defining characteristic of this approach is the utilization of precursors with uniformly distributed metal species within a thermally decomposable organic matrix. Crucially, shell layer number and spacing can be precisely modulated through parameters such as heating rate and precursor composition, eliminating the requirement for templating agents. This strategy demonstrates particular efficacy for synthesizing complex hollow multi-metal oxides [91].

Wang et al. employed quasi-hollow MnCo-glycolate precursors via air annealing to synthesize mesoporous hollow $MnCo_2O_4$ (MCO-II) [92]. Subsequent compositing with graphene oxide (GO) and argon reduction yielded a 3D sandwich-like graphene nanocomposite (MCO-27.2G) featuring double-shell hollow $MnCo_2O_4$ spheres and a reduced graphene oxide (rGO) network (**Figure 7a-c**). This architecture delivered exceptional performance as a lithium-ion battery anode: a capacity retention of 703 $mAh \cdot g^{-1}$ (80%) after 100 cycles at 200 $mA \cdot g^{-1}$ (**Figure 7e**), and a capacity of 538 $mAh \cdot g^{-1}$ at 1000 $mA \cdot g^{-1}$ (**Figure 7d**). These advantages are attributed to the volume buffering effect of the double-shell structure and the conductive support synergy of the rGO network [93].

Zhou et al. leveraged differential core-shell shrinkage during thermal decomposition of $Co_{0.33}Mn_{0.67}CO_3$ microcubes to synthesize double-shelled $CoMn_2O_4$ hollow microboxes (**Figure 7f**, **h-k**) [11]. The resultant material exhibited a high initial discharge capacity (1282 $mAh \cdot g^{-1}$, **Figure 7g**) and superior cycling stability (624 $mAh \cdot g^{-1}$ retention after 50 cycles at 200 $mA \cdot g^{-1}$, **Figure 7l**). Performance enhancements stem from the nanostructure-promoted conversion reactions and the hollow framework's capacity to accommodate volume changes [94].

Zhao et al. synthesized porous Ni-Co-Mn oxide prisms via coprecipitation and calcination exhibited a high specific surface area (96.53 $m^2 \cdot g^{-1}$) and mesoporous structure (average pore size: 18.37 nm) [95]. As a supercapacitor electrode, it achieved a high specific capacitance (1623.5 $F \cdot g^{-1}$ at 1.0 $A \cdot g^{-1}$) and excellent cycling stability (97.8% retention after 5000 cycles). Furthermore, flexible solid-state asymmetric supercapacitors incorporating this material demonstrated a volumetric energy density of 0.885 $mWh \cdot cm^{-3}$ and power density of 48.9 $mW \cdot cm^{-3}$, alongside robust mechanical stability under bending.

Du et al. utilized pure and PdO-loaded double-shelled $ZnSnO_3$ to form hollow microspheres via coprecipitation and calcination. Characterization confirmed that the 4 wt% PdO-loaded sensor exhibited a high response (30.8 to 100 ppm n-propanol), rapid response/recovery kinetics (1s/25s) at 140°C, excellent repeatability, and long-term stability. This superior sensing performance originates from the unique double-shell morphology and the combined catalytic/sensing functionalities of PdO [96].

Although the hard-templating method excels in controlling structural morphology and shell uniformity, its multi-step synthesis process—including template preparation, functionalization, deposition, and removal—significantly increases process complexity and cost. Moreover, template removal often involves strong acids (e.g., HF) or high-temperature calcination, which are not only hazardous but may also damage the shell structure or introduce impurities. Despite its applicability to various materials (e.g., SiO_2, PS), this method exhibits notable limitations in terms of sustainability and large-scale production. The soft-templating approach, leveraging self-assembly behavior, offers excellent control over pore structures, particularly for hierarchical pores and flexible frameworks. Yet the templates used (e.g., surfactants, micelles) often exhibit poor stability under reaction

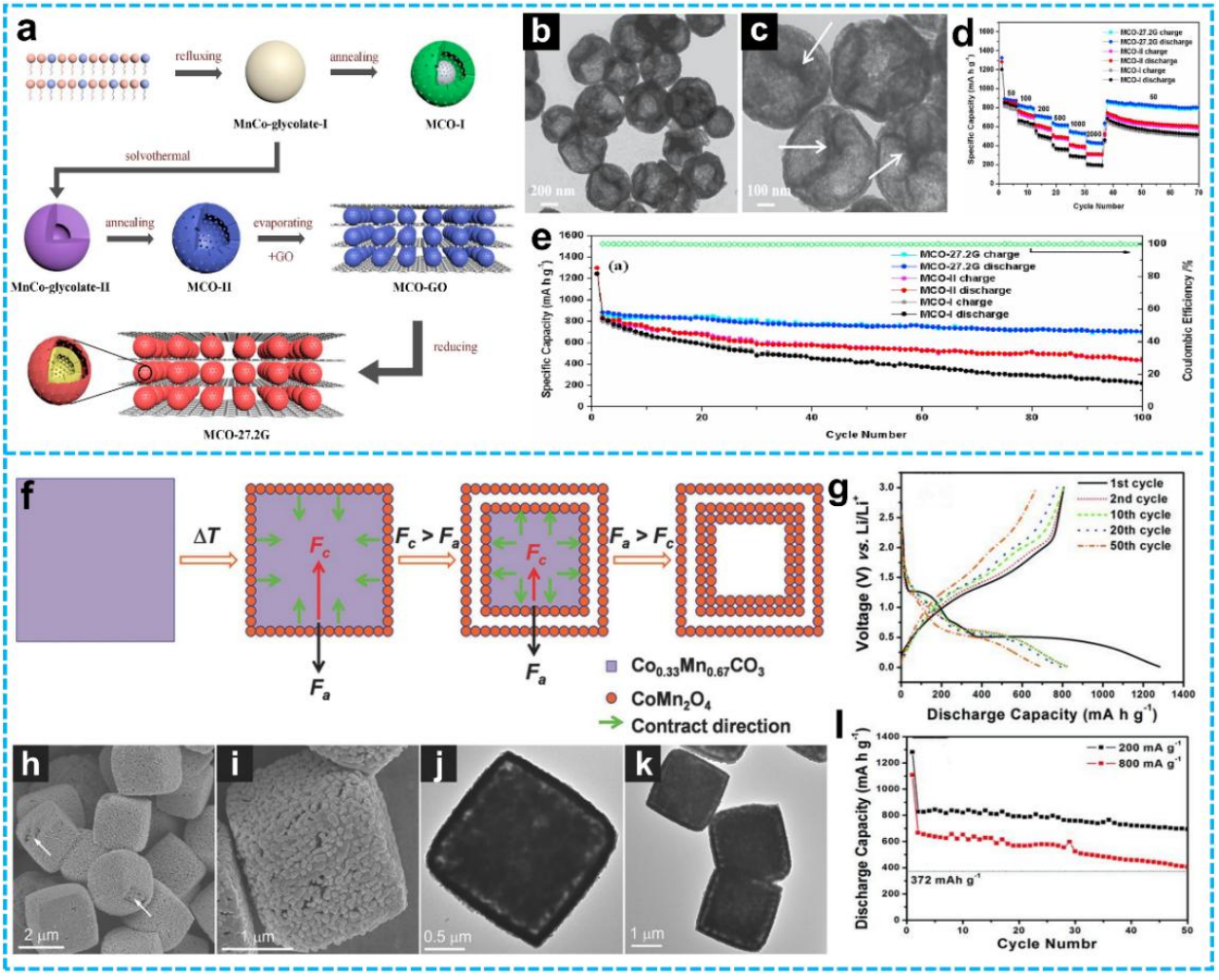

Figure 7 a) Schematic illustration of the typical synthesis routes for yolk-shell MCO-I spheres, mesoporous hollow MCO-II spheres, and MCO-27.2G nanocomposite; b-c) TEM images of mesoporous hollow MCO-II spheres; d) Rate capability of yolk-shell MCO-I spheres, mesoporous hollow MCO-II spheres, and MCO-27.2G nanocomposite electrodes at current densities ranging from 50 to 2000 mA·g^{-1}; e) Cycling performance at 200 mA·g^{-1} [93]. Copyright 2018, Elsevier. f) Schematic diagram of the synthesis of double-shelled $CoMn_2O_4$ hollow microcubes; g) discharge/charge profiles; FESEM (h-i), TEM (j-k) images of double-shelled $CoMn_2O_4$ hollow microcubes; l) Cycling stability of double-shelled $CoMn_2O_4$ hollow microcubes in the voltage window of 0.01-3.0 V vs. Li/Li$^+$ at current densities of 200 and 800 mA·g^{-1} [94]. Copyright 2011, John Wiley and Sons.

conditions and are susceptible to disruption by introduced precursors, limiting their applicability in novel material systems such as multicomponent or heterogeneous structures. Although breakthroughs have been made via cooperative assembly strategies, the generalizability and reproducibility of this method remain challenging. Template-free methods are favored for their simplicity and environmental benefits by avoiding template use, yet each variant has significant limitations: Selective etching highly depends on the chemical heterogeneity within the precursor. If the stability gradient is insufficient, uniform etching becomes difficult, potentially leading to structural irregularity or collapse. Ostwald ripening can facilitate structural evolution from solid to multi-shelled architectures, but requires extended reaction times (up to tens of hours) and is highly sensitive to parameters such as temperature and concentration, making control challenging. The Kirkendall effect, which utilizes diffusion differences to form cavities, is applicable to diverse material systems. However, it requires a significant difference in diffusion rates between components; otherwise, ideal hollow structures may not form, and diffusion asymmetry can cause shell fracture. Ion exchange can construct hollow structures in multinary metal compounds, but the process often

induces structural reorganization or collapse, especially when large ion size differences compromise mechanical stability. Thermally induced mass relocation can form multi-shell structures through uneven shrinkage during heat treatment. However, high temperatures may cause particle sintering, pore closure, or reduction of active sites, adversely affecting the final performance.

Table 2 Comparison of hollow structure preparation methods.

Method type	Method name	Advantage	Disadvantage	Typical application areas
Hard template method	Hard template	Controllable structure, uniform morphology, wide applicability, and good repeatability	Complicated steps, complex template preparation and removal, possible introduction of impurities, high cost	Catalysis, drug delivery, energy storage
Soft template method	Soft template	Adjustable pore structure, suitable for complex multi-level porous materials, mild conditions	Low template stability, sensitivity to reaction conditions, and difficulty in use in multi-component systems	Photocatalysis, battery electrodes, adsorbent materials
Template-free method	Selective etching	No need for templates, simple steps, and the ability to prepare multi shell structures	Dependent on the chemical differences of precursors and difficult to control	Catalysis, sensors
	Ostwald ripening	Template required, controllable number of shell layers, suitable for various metal oxides	Long reaction time and complex kinetic control	Gas sensing, biocatalysis, batteries
	Kirkendall effect	Suitable for various materials (metals, oxides, sulfides, etc.), controllable cavity formation	High requirements for diffusion rate and possible formation of non ideal structures	Gas sensing, electrochemical energy storage
	Ion exchange	Capable of preparing multi-component compounds with diverse structures, suitable for complex hollow structures	The ion exchange process is difficult to control and may lead to structural collapse	Supercapacitors, electrocatalysts
	Thermally induced matter repositioning	Capable of preparing multi shell hollow structures, template free, suitable for multi metal oxides	High temperature treatment may lead to sintering or structural damage	Lithium-ion batteries, supercapacitors

Current synthetic methods for hollow structures each possess distinct features, while also exhibiting inherent limitations. Future research should focus on developing green, highly efficient, and precisely controllable synthesis strategies integrating *in situ* characterization techniques with computational simulations to drive the evolution of this strategy towards truly precise and predictable synthesis to achieve the ultimate goal of facilitating their more extensive utilization in various domains, including catalysis, energy, and sensing.

3 Energy Storage and Conversion Applications

Hollow-structured materials represent a significant advancement in energy storage and conversion technologies due to their inherent structural advantages. Their three-dimensional frameworks integrate high specific surface area, tunable porosity, and low density, establishing an exceptional structural paradigm for efficient energy management.

In energy storage systems, hollow architectures effectively mitigate electrode volume expansion during cycling, substantially enhancing structural integrity and extending cycle life of batteries (lithium-ion/sodium-ion) [97]. Concurrently, the internal void space accommodates greater active material loading, while shortened ion diffusion pathways improve reaction kinetics and energy density [98]. The interconnected hollow channels facilitate rapid electrolyte ion transport in supercapacitors. Combined with abundant electrochemically accessible surface sites, this enables the delivery of exceptionally high power density [99].

In energy conversion applications, the confined interior spaces enable precise modulation of catalytic reaction pathways. For instance, in electrocatalytic processes (e.g., oxygen reduction reaction (ORR) and hydrogen evolution reaction (HER)), thin walls maximize active site exposure, optimizing reactant adsorption and product desorption. This enhances energy conversion efficiency in devices such as fuel cells and water electrolyzers [100]. Furthermore, the multifunctionality achievable through composite hollow structures synergistically enhances electrical conductivity and chemical stability, providing a robust platform for designing high-durability electrocatalysts and electrodes [101].

These collective attributes position hollow-structured

materials as a pivotal strategy for overcoming the intrinsic limitations of conventional energy materials, demonstrating considerable potential for advancing next-generation energy storage devices and renewable energy conversion technologies.

3.1 Energy Storage

3.1.1 Lithium-ion Batteries

Lithium-ion batteries (LIBs) represent highly efficient electrochemical energy storage systems. Their operation relies on the reversible insertion and extraction of lithium ions between a cathode and an anode, facilitated by an ion-conducting electrolyte [102]. Key advantages include high energy density, lightweight design, and environmental friendliness, establishing LIBs as the dominant power source for portable electronics and a critical technology for electric vehicles and smart grids [103]. However, the energy density of conventional LIB systems is approaching theoretical limits, insufficient for demanding high-range applications [104]. Concurrently, high-capacity anode materials (e.g., silicon, tin, transition metal oxides - TMOs) undergo substantial volume fluctuations during cycling. This induces material pulverization, interfacial instability, and rapid capacity degradation, presenting critical bottlenecks for practical implementation [105, 106].

Hollow-structured materials offer a promising approach to mitigate these challenges. Their internal voids effectively accommodate mechanical stresses from volume expansion, minimize dimensional changes, prevent electrode fracturing, and inhibit agglomeration of nanostructured electroactive materials. Furthermore, thin shells shorten lithium-ion diffusion paths, enhancing reaction kinetics, while porous shells increase active site exposure and improve electrolyte penetration efficiency [107].

Transition metal oxides (TMOs), operating via conversion-reaction mechanisms, exhibit high specific capacities—typically two- to threefold greater than graphite [108]. Significant research has therefore focused on complex hollow architectures of TMOs (e.g., Co_3O_4, CoO, Ni_2O_3, Mn_3O_4) [109-111].

Huang et al. synthesized ultra-fine Co_3O_4 hollow nanoparticles (< 20 nm) uniformly embedded within a mesoporous carbon nanowall using a MOF-template strategy involving chemical etching and coordination bonding, followed by a two-step annealing process (**Figure 8a-b**) [110]. This structure confers multiple benefits: i) Internal cavities buffer volume expansion during lithiation/delithiation, preventing structural collapse. ii) Nanoscale dimensions and homogeneous dispersion increase active interfacial sites and shorten Li^+ diffusion paths, enabling a specific capacity of 420 $mA{\cdot}h{\cdot}g^{-1}$ at 5 $A{\cdot}g^{-1}$ (**Figure 8c**). The porous carbon framework enhances electron transport, facilitates electrolyte infiltration/ion migration, and physically confines Co_3O_4 nanoparticles, suppressing agglomeration and maintaining integrity. Synergistically, this yielded a high specific capacity (1120 $mA{\cdot}h{\cdot}g^{-1}$ at 0.2 $A{\cdot}g^{-1}$ over 100 cycles, **Figure 8d**) and excellent rate capability (reversible capacity fluctuation rate < 63% between 0.1-5 $A{\cdot}g^{-1}$), significantly outperforming pure Co_3O_4 nanoboxes (48% capacity retention after 300 cycles).

Kang et al. developed Co_3O_4/CeO_2 heterostructures via one-step microwave synthesis of MOF precursors (**Figure 8f-g**) to address the dual challenges of large volume changes and low intrinsic conductivity in Co_3O_4 [111]. Optimizing the Co^{2+}/Ce^{3+} molar ratio revealed the 5 Co_3O_4/CeO_2 composite (5:1 Co/Ce) exhibited superior performance: i) A reversible specific capacity of 1131.2 $mA{\cdot}h{\cdot}g^{-1}$ after 100 cycles at 100 $mA{\cdot}g^{-1}$ (**Figure 8i**), markedly higher than single-phase Co_3O_4 (538.6 $mA{\cdot}h{\cdot}g^{-1}$). ii) High-rate capacity retention of 835.3 $mA{\cdot}h{\cdot}g^{-1}$ at 2000 $mA{\cdot}g^{-1}$ (**Figure 8h**). The enhancement stems from CeO_2 synergy (**Figure 8e**): acting as an inert support buffering Co_3O_4 volume expansion, forming interfaces that shorten Li^+ diffusion paths and enhance conductivity, and the MOF-derived mesoporous structure improving electrolyte access/active site exposure. Interfacial capacitive contributions further boost reversible capacity. This work provides novel design insights for rare-earth-modified heterostructures.

Tabassum et al. reported a generalized pyrolysis-oxidation method (**Figure 8j**) to synthesize core-shell hollow TMO nanoparticles (e.g., CoO, Ni_2O_3, Mn_3O_4) encapsulated within boron/nitrogen co-doped graphitic nanotubes (BNG) as Core-Shell TMO@BNG Nanotubes (**Figure 8k**) [109]. Designed as high-performance LIB anodes, the TMO@BNG leverages structural synergies. Notably, CoO@BNG demonstrated rate capabilities of 1451, 1215, 1008, 670, 631, 520, and 247 $mA{\cdot}h{\cdot}g^{-1}$ from 0.1 to 3 $A{\cdot}g^{-1}$ (**Figure 8l**); exceptional cyclic stability (96% capacity retention after 480 cycles at 1.75 $A{\cdot}g^{-1}$). This performance arises from the hollow TMO buffering volume expansion and the BNG providing high conductivity, large surface area for electrolyte penetration, and SEI film stabilization (**Figure 8m**).

Beyond TMOs, silicon-based materials are highly promising anodes due to an exceptional theoretical capacity (~4200 $mA{\cdot}h{\cdot}g^{-1}$), nearly tenfold higher than graphite. However, severe lithiation-induced volume expansion causes pulverization, electrode collapse,

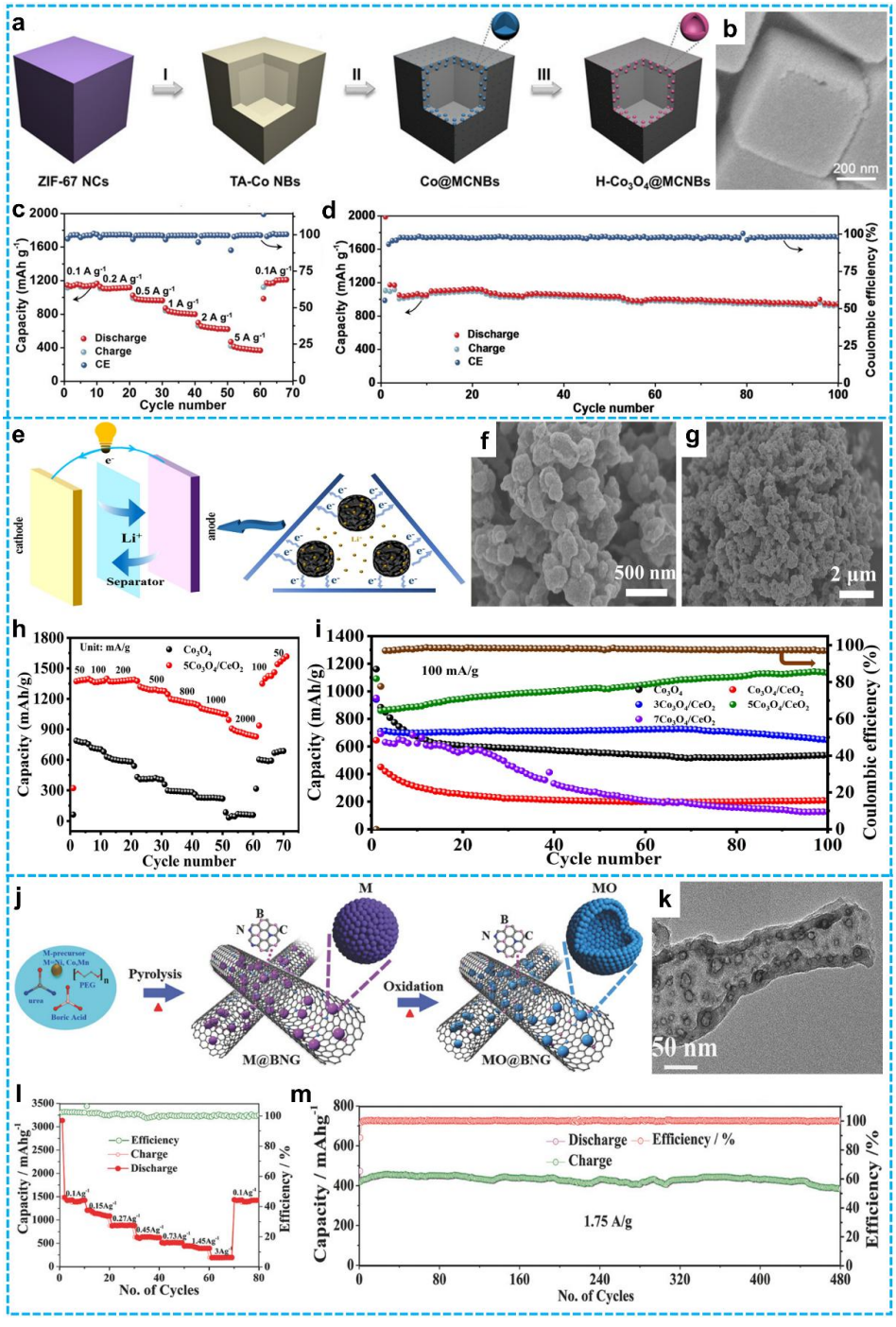

Figure 8 a) Schematic illustration of the formation process of H-Co_3O_4@MCNBs; b) FESEM images of H-Co_3O_4@MCNBs; c) Rate capability and coulombic efficiency profiles at different current densities; d) Cycling stability at 0.2 $A \cdot g^{-1}$ and the associated Coulombic efficiency [110]. Copyright 2020, John Wiley and Sons. e) Schematic of a lithium-ion battery; Li^+ shuttles between cathode and anode via separator; Left: overall battery structure with electron flow powering a device; Right: enlarged view of anode showing Li^+ and e^- movement, key for anode electrochemical reactions during charge-discharge; f-g) SEM images of 5 Co_3O_4/CeO_2; h) rate performance of Co_3O_4 and 5 Co_3O_4/CeO_2; i) Cycling performance of as-prepared samples at 100 $mA \cdot g^{-1}$ [111]. Copyright 2021, Elsevier. j) Synthesis schematic of MO@BNG (MO: CoO, Ni_2O_3, Mn_3O_4) nanotubes; k) TEM image of CoO@BNG nanotubes of hollow CoO nanoparticle; l) Storage capacity of CoO@BNG nanotubes at various current densities; m) Long-term cycling stability of CoO@BNG at a high current density of 1.75 $A \cdot g^{-1}$ [109]. Copyright 2018, John Wiley and Sons.

conductive network failure, exacerbated interfacial reactions, and unstable SEI growth [112]. Nanostructuring, particularly hollow structures (porous Si, core-shell, yolk-shell), effectively buffers stress and accommodates expansion. Nevertheless, inherent low particle density and potential pore collapse during electrode calendaring or cycling can diminish the benefits of hollow designs. Addressing this, the Li team engineered a high-density, crack-resistant Si-C microparticle [113]. Its key feature is a dual-layer carbon matrix: i) An inner porous carbon layer (mesopore volume 62.53 $m^2 \cdot g^{-1}$) buffers Si expansion. ii) An outer dense carbon layer (specific surface area 3.58 $m^2 \cdot g^{-1}$) prevents electrolyte penetration. This "in-situ pore generation" design achieves a high tap density (0.86 $g \cdot cm^{-3}$, 473% improvement over traditional hollow structures), 96.2% capacity retention after 200 cycles, and minimal electrode expansion (18.6% vs. ~ 50% industry standard). Full cells pairing this anode with $LiFePO_4$ exhibit an 18.3% increase in energy density compared to graphite-based cells, demonstrating significant progress towards high-energy-density batteries via optimized hollow structure engineering.

3.1.2 Lithium-Sulfur Batteries

Lithium-sulfur (Li-S) batteries represent a promising next-generation high-energy-density storage technology. Their core advantage lies in the sulfur cathode's exceptionally high theoretical specific capacity (1, 675 $mA \cdot h \cdot g^{-1}$), coupled with abundant raw materials, low cost, and environmental benignity, positioning them as potential replacements for conventional lithium-ion batteries (LIBs). However, significant challenges impede their practical implementation: i) The inherently insulating properties of sulfur and its discharge products (Li_2S_2/Li_2S) result in poor electrical conductivity and severely limit the utilization of the active material [114]. ii) Soluble lithium polysulfide intermediates (LiPSs, Li_2S_n, $4 \leq n \leq 8$), generated during the redox processes, shuttle between the electrodes, leading to irreversible active material loss, rapid capacity fade, and poor cycling stability. iii) The substantial volumetric expansion (~80%) occurring during repeated lithiation/delithiation cycles induces significant mechanical stress within the electrode, resulting in structural degradation [115].

Hollow carbon nanostructures (HCNs) represent a promising mitigation strategy, leveraging their inherent structural advantages as high surface area, tunable porosity, and mechanical resilience, which providing a versatile platform for addressing these challenges. The high void volume enables efficient encapsulation of sulfur within its internal cavity. Optimized pore structures accommodate volume changes during cycling via a buffering effect. The carbon shell functions as a physical barrier, effectively suppressing the dissolution and migration of lithium polysulfides (LiPS), thereby mitigating the shuttle effect. Enhanced kinetics arise from the mesoporous channels facilitating Li^+ diffusion and improving the conductivity of the encapsulated sulfur, thus boosting electrochemical utilization efficiency [116].

Pioneered by the Nazar group's demonstration of LiPS confinement using ordered mesoporous carbon (CMK-3) [117], structural engineering of carbon hosts has become central to Li-S research. This field has diversified into a multi-dimensional innovation system. Hollow carbon nanospheres encapsulate sulfur within their sealed cavities, effectively confining sulfur and mitigating its volume changes during cycling [118]. Hierarchical carbon nanocages incorporate three-dimensionally interconnected porous structures, facilitating rapid ion diffusion and electrolyte penetration [119]. Aligned carbon nanotube (CNT) arrays utilize their inherent axial electrical conductivity to significantly enhance the overall electrode conductivity [120]. Micro/mesoporous carbons exploit the synergistic effects of their multi-scale porosity to achieve high sulfur loading and retention in high-capacity cathodes [116]. Porous graphene facilitates the design of ultra-thin and potentially flexible electrodes due to its extended single-atom-layer structure [121].

Through pore topology optimization and dimensional control, these materials provide synergistic solutions to sulfur's low conductivity and LiPS shuttling. Despite their benefits, non-polar carbon materials exhibit insufficient chemical interactions with polar LiPSs, limiting their confinement efficacy primarily to physical barriers, effective mainly in short-term cycling. To enhance LiPS anchoring for extended cycle life, two primary strategies are widely pursued [122]:

Heteroatom-doped carbon matrices: Introducing electron-donating heteroatoms (e.g., N, O, S) significantly enhances LiPS chemisorption via dipole-dipole coupling with Li^+. For instance, Zhang et al. synthesized hydrophilic graphene@graphite-phase nitrogen-doped carbon (GCN) nanosheets with a hierarchical porous structure (macropores ~60 nm, mesopores ~3 nm) using oil-phase microemulsion templating (**Figure 9a**). Sulfur (82 wt%) was *in situ* encapsulated within the GCN pore walls (**Figure 9d, e**). Pyridinic N moieties within the GCN/ g-C_3N_4 matrix engage in Lewis acid-base interactions with Li atoms in Li_2S_n, providing strong chemisorption to suppress dissolution [123, 124]. Concurrently, the

graphene framework ensures high conductivity and mechanical integrity. This "physical-chemical dual confinement" design buffers volume expansion via macropores while enhancing anchoring via mesopores and N-doping. Consequently, the S/GCN cathode delivered 612 mA·h·g^{-1} at 10 C (**Figure 9b**), retained 86% capacity after 800 cycles at 0.3 C (decay rate: 0.017% per cycle; **Figure 9f**), and exhibited near-100% coulombic efficiency with minimal capacity decay across varied rates, demonstrating exceptional reversibility and rate capability (**Figure 9c**) [125].

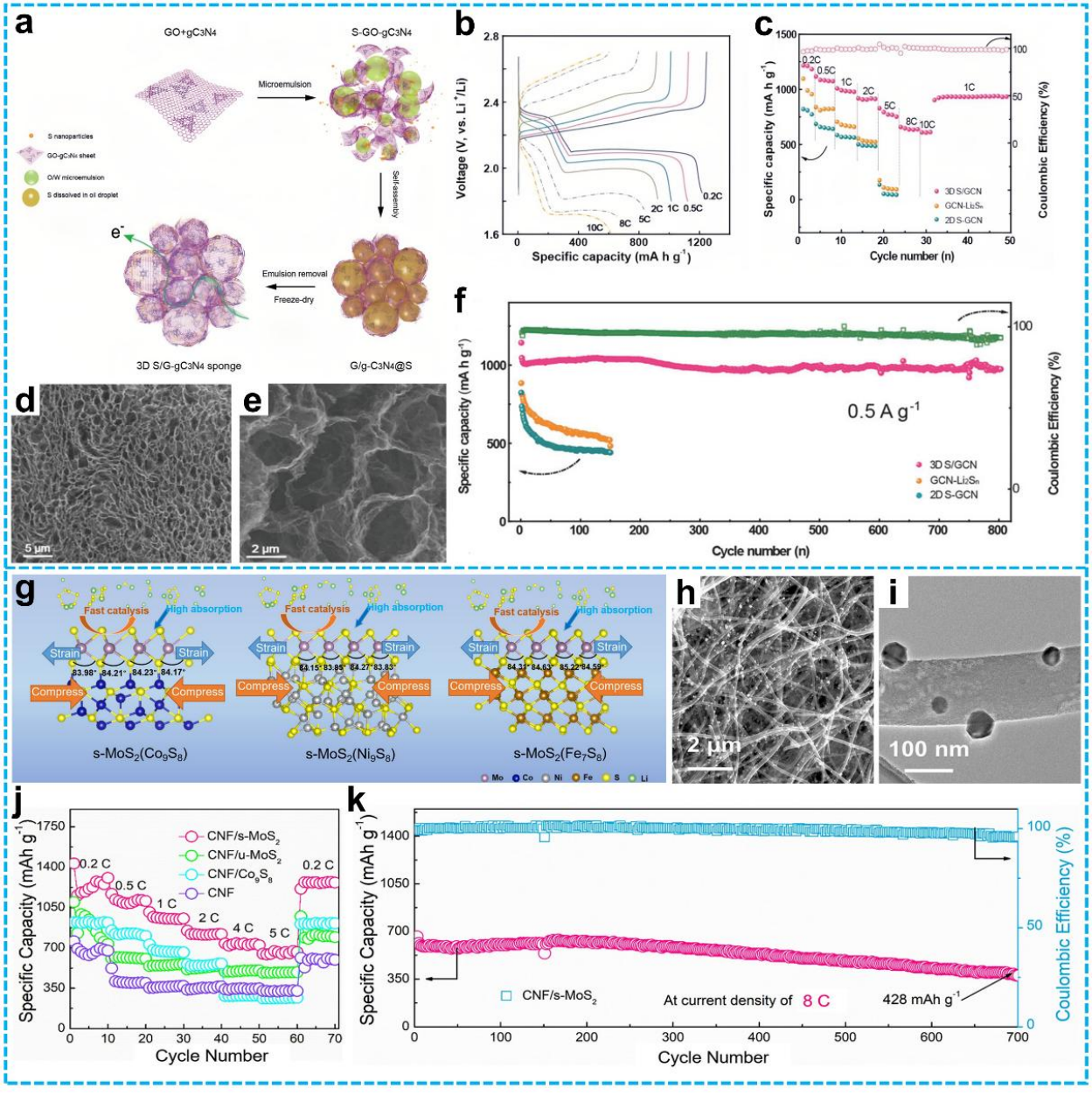

Figure 9 a) Schematic diagram of the preparation process for S/GCN hybrid sponges; b) Galvanostatic charge-discharge (GCD) voltage profiles of the S/GCN cathode at various charge-discharge rates; c) Rate performance of S/GCN, GCN-Li_2Sn, and S-GCN electrodes (Coulombic efficiency data correspond to the S/GCN cathode); d) Cross-sectional morphology and e) high-resolution SEM image of S/GCN; f) Long-term cycling stability of S/GCN, GCN-Li_2S_n, and S-GCN cathodes at a low current density of 0.5 A·g^{-1} (0.3 C) [125]. Copyright 2018, John Wiley and Sons. g) Ball-and-stick models depicting strained MoS_2 adsorbed on Co_9S_8, Ni_9S_8, and Fe_7S_8 surfaces; h) SEM and i) low-magnification TEM images of CNF/s-MoS_2(Co_9S_8) composites; j) Rate performance of the cells from 0.2 C to 5 C; k) Long-term cycling stability of the CNF/s-MoS_2 electrode over 700 cycles at 8 C [130]. Copyright 2022, Elsevier.

Polar hosts based on transition metal compounds: Materials like metal sulfides [126], oxides [127], and MXenes [128] offer enhanced LiPS fixation through Lewis acid-base coordination, polar interactions, and sulfur-chain bridging. Molybdenum disulfide (MoS_x) distinguishes itself due to its layered structure, high intrinsic conductivity (10-100 S/cm), rapid Li^+ diffusion ($D_{Li^+}\approx10^{-8}cm^2/s$), and strong LiPS affinity (adsorption energy > 2.5 eV) [129]. Zhang et al. employed strain engineering to modulate MoS_2 surface structure, synthesizing core-shell nanoparticles (metal sulfide core / strained MoS_2 (s-MoS_2) shell) via electrospinning (**Figures 9h, i**). Strain enlarged the S-Mo-S bond angle and shifted the d-band center closer to the Fermi level, boosting both LiPS adsorption and catalytic conversion kinetics (**Figure 9g**). The resulting CNF/s-MoS_2 cathodes achieved high reversible capacities (1290 $mA\cdot h\cdot g^{-1}$ at 0.2 C; 657 $mA\cdot h\cdot g^{-1}$ at 5 C; **Figure 9j**) and outstanding stability (0.05% decay per cycle after 700 cycles at 8 C; **Figure 9k**), exemplifying the potential of strain-engineered core-shell designs [130].

3.1.3 Supercapacitors

Supercapacitors as an emerging class of electrochemical energy storage systems, exhibit substantial promise due to their high power density, rapid charge-discharge kinetics, and exceptional cycle stability [131-137]. Crucially, they bridge the performance gap between traditional capacitors and batteries, achieving energy density enhancements spanning multiple orders of magnitude, which makes them particularly suitable for applications requiring short-term, high-power output, such as electric vehicle start-stop systems and grid frequency regulation [132]. However, limitations persist, primarily low energy density (typically < 10 $Wh\cdot kg^{-1}$) and insufficient utilization of active materials, hindering broader application.

Hollow nanostructured materials present a promising strategy to address these challenges. Their unique structural design offers key advantages: i) Enhanced accessible reaction sites promote higher energy density; ii) Porous shell structures facilitate efficient electrolyte penetration and significantly shorten ion diffusion pathways, leading to elevated power density. Critically, in complex multi-shelled architectures, the outer shell represents as a protective barrier against electrochemical degradation and mechanical attrition of inner components, ensuring superior cycling stability through structural reinforcement [10].

Supercapacitors are categorized into three primary types based on energy storage mechanisms : electric double-layer capacitors (EDLCs) relying on interfacial charge separation, pseudocapacitors utilizing surface Faradaic redox reactions, and hybrid devices combining both mechanisms. Pseudocapacitors are distinguished from EDLCs by their Faradaic charge storage, which endows them with superior specific capacity and energy density [138]. Consequently, significant research focuses on transition metal oxide-based pseudocapacitive materials, such as NiO [139], Co_3O_4, and MnO_x [140, 141]. A fundamental limitation of these single-metal systems, however, is inadequate intrinsic electrical conductivity, resulting in compromised cyclic stability and rate capability.

To overcome this limitation, ternary metal oxides have emerged as a promising alternative, leveraging multi-metal synergistic effects, abundant active sites, and optimized charge transport properties [142, 143]. Among these, $NiCo_2O_4$ and $MnCo_2O_4$ demonstrate significant potential. Researchers continuously optimize their electrochemical performance through innovative synthesis: Hao et al. synthesized eggshell-structured $NiCo_2O_4$ (**Figure 10a**), achieving a high specific capacitance of 835.7 $F\cdot g^{-1}$ at 0.5 $A\cdot g^{-1}$ (**Figure 10b**) and exceptional cycling stability (93% retention after 10, 000 cycles at 10 $A\cdot g^{-1}$; **Figure 10c**) [144]. Yang et al. developed a hollow $NiCo_2O_4$ architecture (**Figure 10d**), delivering 1229 $F\cdot g^{-1}$ at 1.0 $A\cdot g^{-1}$ and maintaining 83.6% capacity at 25 $A\cdot g^{-1}$ (**Figure 10e**) [145]. Similarly, MOF-templated $MnCo_2O_4$ nanocages (**Figure 10f**) exhibited a superior specific capacitance of 1763 $F\cdot g^{-1}$ and 95% retention after 4500 cycles (**Figure 10g**) [146]. These findings underscore the critical role of structural engineering, particularly hollow designs with tunable shell permeability and internal void space, in enhancing electrochemical performance [10, 147 -150].

Despite progress with single-phase hollow structures, the rational design of complex hybrid architectures remains underexplored. Addressing this, Shi et al. developed $NiCo_2O_4/MnCo_2O_4$ composite yolk-shell hollow spheres (YSHS) (**Figure 10i, j**) using nickel-manganese-cobalt glycerate templates combined with selective etching and pyrolysis (**Figure 10h**). This distinctive hierarchical architecture confers multifaceted advantages: an ultra-high specific capacitance of 1636 $F\cdot g^{-1}$ at 4.0 $A\cdot g^{-1}$; robust rate capability (57.4% retention at 20 $A\cdot g^{-1}$; **Figure 10k**); and exceptional cycling stability (only 10% decay after 6000 cycles at 15 $A\cdot g^{-1}$; **Figure 10l**). When integrated into solid-state asymmetric supercapacitors, the device delivered a high energy density of 62.8 $Wh\cdot kg^{-1}$ at 1650.4 $W\cdot kg^{-1}$, retaining 23.2 $Wh\cdot kg^{-1}$ even at an ultra-high power density of 12367.7 $W\cdot kg^{-1}$ [99]. This performance highlights its strong suitability for high-power electrochemical energy storage.

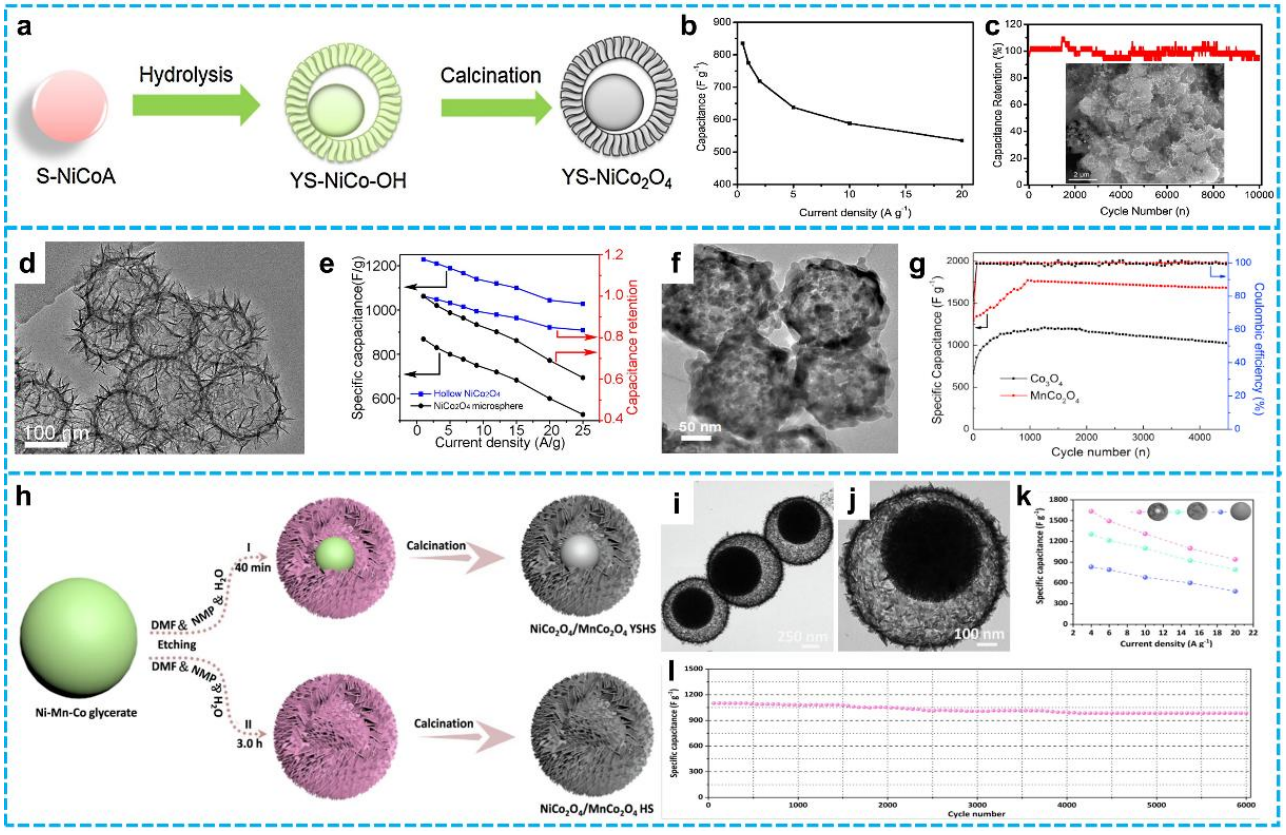

Figure 10 a) Diagram of the formation processes of YS-$NiCo_2O_4$; b) the capacitance and c) the cycle life at 10 $A \cdot g^{-1}$ and SEM image of YS-$NiCo_2O_4$ after 10, 000 cycles in inset [144]. Copyright 2018, Elsevier. d) TEM image of hollow $NiCo_2O_4$ nanospheres; e) The specific capacitances and capacitance retentions of the hollow $NiCo_2O_4$ nanospheres and $NiCo_2O_4$ microspheres [145]. Copyright 2018, Elsevier. f) TEM image of the as-obtained nanocage $MnCo_2O_4$; g) Coulombic efficiency of the two electrodes at the density of 1 $A \cdot g^{-1}$ [146]. Copyright 2017, Elsevier. h) Schematic illustration of the process for controllable synthesizing $NiCo_2O_4/MnCo_2O_4$ hollow structures; i-j) TEM images of $NiCo_2O_4/MnCo_2O_4$ YSHS; k) Specific capacitance of $NiCo_2O_4/MnCo_2O_4$ SS, HS and YSHS at current density 4.0-20 $A \cdot g^{-1}$; l) Cycling performance of $NiCo_2O_4/MnCo_2O_4$ YSHS at 15 $A \cdot g^{-1}$ over 6000 continuous charge-discharge [99]. Copyright 2023, Elsevier.

3.2 Energy Conversion

3.2.1 Electrocatalysis

Sustainable energy technologies have consistently constituted a critical research frontier. A central challenge in modern energy conversion systems is the rational design of highly efficient and durable electrocatalysts to drive critical electrochemical reactions [151-158], including the hydrogen evolution reaction (HER) [159], oxygen evolution reaction (OER) [160], oxygen reduction reaction (ORR) [161], and methanol oxidation reaction (MOR) [48].

Conventional precious metal electrocatalysts (e.g., Pt, Ru), while exhibiting excellent activity, suffer from scarcity and prohibitive costs, constraining large-scale deployment [162, 163]. Furthermore, issues such as inadequate stability, limited mass transport efficiency, and insufficient active site exposure necessitate urgent resolution. Consequently, extensive research has focused on developing cost-effective transition metal-based alternatives, particularly transition metal oxides (TMOs) [101, 164 -166]. Yet the widespread application of TMOs is hindered by their intrinsically poor electrical conductivity, which impedes efficient electron transport and significantly compromises electrocatalytic performance, notably in OER [101, 166, 167].

Hollow nanostructures represent a promising strategy to address key electrocatalyst limitations: i) Functional integration. Spatially segregated compartments within hierarchical hollow architectures facilitate the integration of otherwise incompatible catalytic functionalities or the encapsulation of distinct reactive species, enabling complex cascade reactions. ii) Enhanced selectivity. Tailoring shell pore architecture allows for molecular sieving, while modulating the chemical affinity at the

shell interface can control reactant diffusion pathways, thereby systematically improving catalytic selectivity. iii) Maximized active sites: The inherent large specific surface area of hollow nanostructures significantly increases catalyst loading density and expands the accessible interface between active sites and reactant molecules. iv) Efficient mass transport: Ultrathin shell structures with optimized thickness promote rapid ion and molecular transport, minimizing diffusion resistance in electrochemical environments [168].

Rational optimization of TMO electronic properties is therefore critical for enhancing OER activity. Heteroatom doping or establishing strong coupling between active sites effectively modulates electronic configurations and activates catalytic centers, improving electronic transport and charge transfer kinetics [169].

Xu et al. synthesized mesoporous CoMn and CoMnSe nanobundles via hydrothermal methods (**Figure 11a**). Mn incorporation into cobalt oxides concurrently tunes electronic structure and induces nanobuckled morphology. The resulting self-supported Co_1Mn_1 bimetallic oxide achieves exceptional OER activity, requiring an ultralow overpotential of 221 mV at 10 mA·cm^{-2} (**Figure 11b**). The nanobranched Co_1Mn_1Se further exhibits superior HER performance (overpotential: 87.3 mV at 10 mA·cm^{-2}; **Figure 11c**), surpassing most reported non-noble metal catalysts. Leveraging these complementary activities, a water electrolyzer employing Co_1Mn_1 oxide (anode) and Co_1Mn_1Se (cathode) attained 10 mA·cm^{-2} at 1.60 V in 1.0 M KOH (**Figure 11d, e**) with stable 36-hour operation (**Figure 11f**), demonstrating high-efficiency overall water splitting [167].

In parallel, Lu's team developed a bifunctional Co@N-C/PCNF electrocatalyst (i.e., Co nanoparticles encapsulated in N-doped hollow porous carbon nanofibers) via ultra-rapid high-temperature impact synthesis (**Figures 11g-j**). Synergy between Co-N-C active sites and the porous carbon framework (**Figures 11k-p**) confers outstanding bifunctionality: OER overpotential of 289 mV at 10 mA·cm^{-2} and ORR half-wave potential of 0.85 V. The Co-N-C moieties optimize adsorption/desorption kinetics and reduce activation barriers by modulating the local electronic environment. When deployed in aqueous zinc-air batteries (AZABs; **Figure 11q**), the catalyst delivers a peak power density of 292 mW·cm^{-2} (**Figure 11r**). Flexible AZABs incorporating this material successfully power wearable electronics, underscoring its practical utility in portable energy systems [170].

3.2.2 Photocatalysis

Photocatalysis represents an advanced oxidation process, has garnered significant research interest due to its inherent advantages of high efficiency [171-176], cost-effectiveness, and minimal secondary pollution, which finds diverse applications, including hydrogen generation [177, 178], CO_2 photoreduction [179-183], heavy metal detoxification, biodegradation, and air purification.

While specific reaction mechanisms vary, the fundamental photocatalytic process universally involves three critical stages (**Scheme 4**) [184]:

i) Light absorption: Photocatalysts absorb photons, promoting electrons from the valence band (VB) to the conduction band (CB), thereby generating electron-hole pairs. This photoexcitation governs the spectral response range and energy conversion efficiency. Common photocatalysts like TiO_2 and ZnS primarily absorb ultraviolet light, though visible light absorption is highly desirable. Enhancing light harvesting efficiency is crucial for improving quantum yield and catalytic performance in applications such as pollutant mineralization, water splitting, and CO_2 reduction. Consequently, optimizing light absorption characteristics—particularly broadening the response range and enhancing visible light utilization—represents a core research objective. Strategies include material design, structural modulation, and surface engineering [185].

ii) Charge separation and migration: The photogenerated electron-hole pairs must rapidly separate to prevent recombination within the catalyst bulk or on its surface. This separation can be facilitated by internal electric fields, grain boundary effects, or surface modifications. Efficient separation and subsequent migration of carriers to the catalyst surface are pivotal determinants of photocatalytic activity. Yet the significant recombination losses occur during transit or upon surface arrival, dissipating energy as heat or light. Minimizing recombination is therefore essential for enhancing overall efficiency [186].

iii) Surface redox reactions: Effectively separated charge carriers participate in redox reactions at the photocatalyst surface. Photoexcited electrons typically reduce adsorbed oxidants (e.g., O_2, H_2O), while holes oxidize adsorbed reductants (e.g., organic pollutants, H_2O). The specific reactions depend on the donor-acceptor properties of the adsorbed species. Long-lived carriers exhibit greater potential to drive targeted redox pathways, enabling pollutant degradation or solar fuel synthesis [187].

Nonetheless, the practical deployment of photocatalytic materials remains encumbered by significant limitations: i) Narrow spectral response. Many catalysts (e.g., TiO_2) are primarily UV-active,

limiting solar energy utilization. ii) Rapid charge recombination. High recombination rates lead to low quantum efficiencies. iii) Limited active sites. Agglomeration of nanoparticles reduces specific surface area and accessible reaction sites, hindering scalability [188].

The synergistic optimization of these is critical for driving thermodynamically unfavorable reactions using light energy. Key strategies include selecting appropriate photocatalysts, optimizing surface properties, and enhancing charge separation efficiency to improve reaction rates and selectivity.

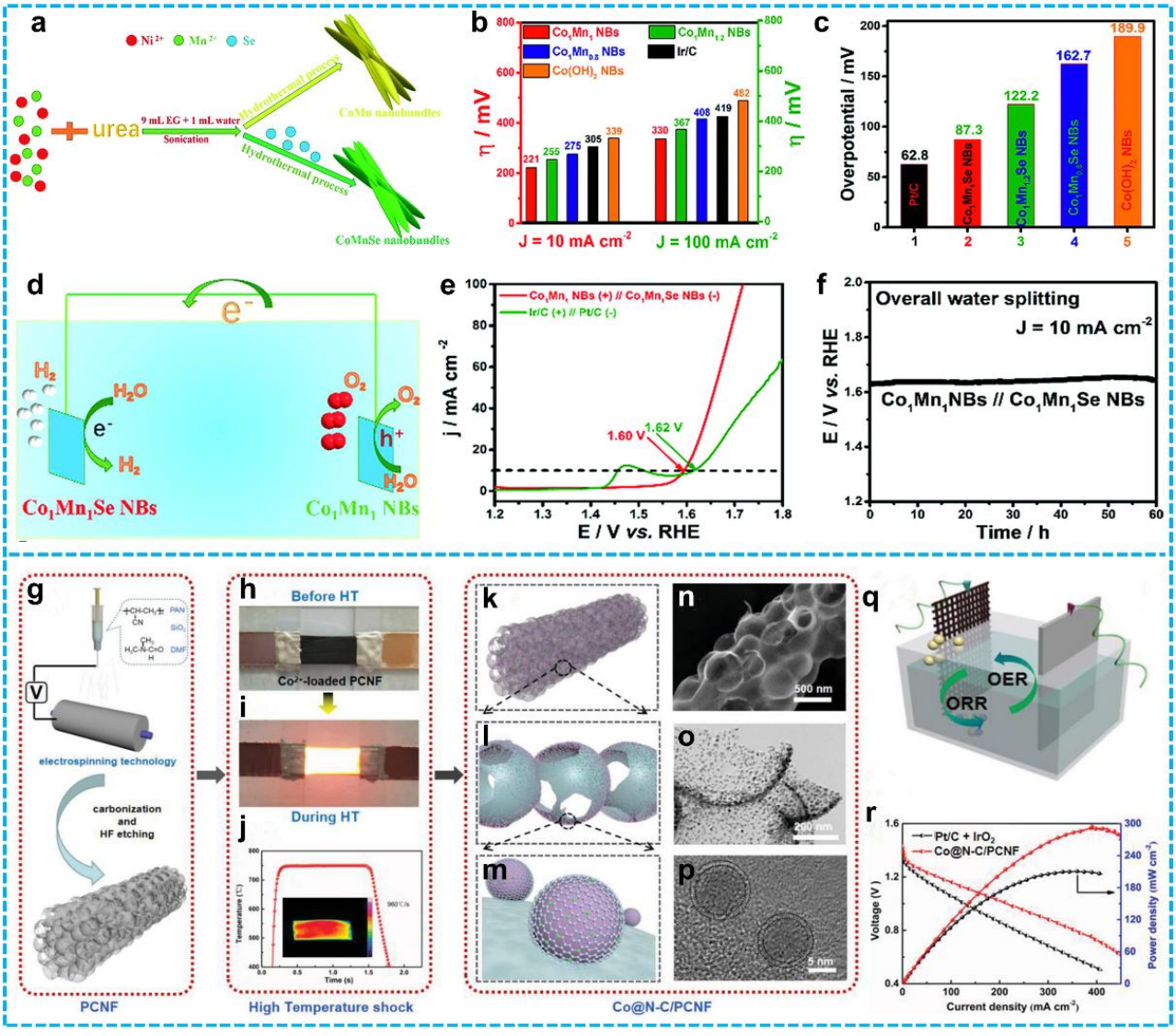

Fig 11. a) Schematic representation of the synthetic methodology for CoMn and CoMnSe nanobundles; b) Overpotential values at current densities of 10 and 100 mA·cm^{-2} and c) Overpotentials at a current density of 10 mA·cm^{-2} for Co_1Mn_1Se NBs, $Co_1Mn_{1.2}Se$ NBs, $Co_1Mn_{0.8}Se$ NBs, Pt/C, and $Co(OH)_2$ NBs; d) Schematic diagram of the overall water electrolysis process; e) Polarization curves for the Co_1Mn_1 NBs (+)//Co_1Mn_1Se NB (−) electrode pair and the Ir/C (+)//Pt/C (−) pair in 1.0 M KOH solution at a scan rate of 5 mV·s^{-1}; f) Continuous chronopotentiometry (CP) measurement of the Co_1Mn_1 NBs (+)//Co_1Mn_1Se NB (−) couple over 36 hours [167]. Copyright 2018, Royal Society of Chemistry. g) Schematic representation of the high-temperature (HT) shock synthesis of PCNF; h-i) Photographic sequences depicting the heating procedures employed in the fabrication of Co@N-C/PCNF; j) Temperature profile during the HT shock process, with an inset showing the temperature distribution map; k-m) Structural modeling of distinct components in Co@N-C/PCNF, accompanied by n) SEM, o) TEM, and p) HRTEM images that characterize the selected structural features of the Co@N-C/PCNF composite; q) Schematic illustration of the AZAB configuration; r) Corresponding discharge polarization curves and power density profiles [170]. Copyright 2023, John Wiley and Sons.

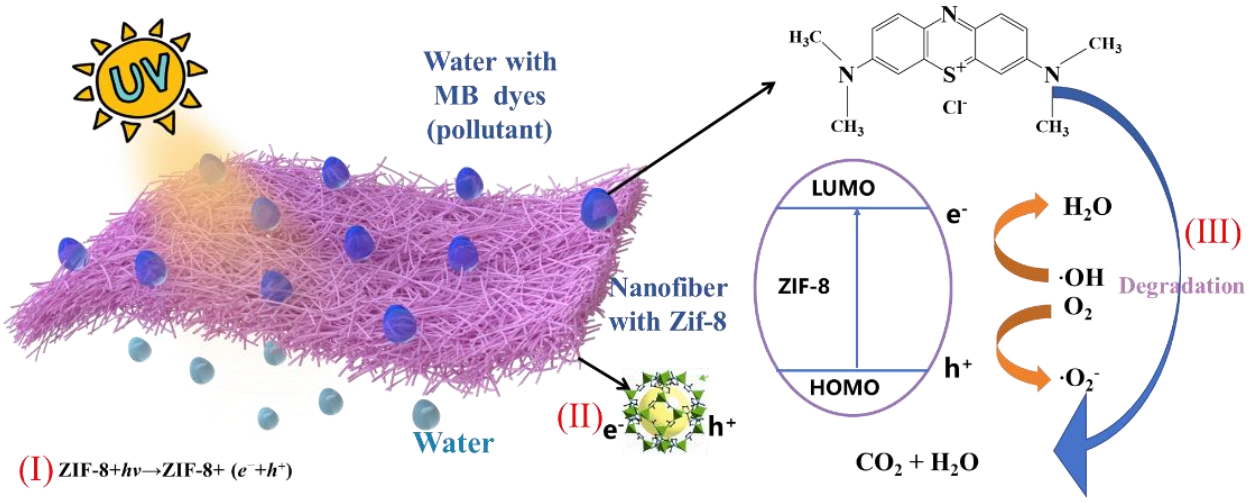

Scheme 4 Steps of the photocatalytic reaction process. (I) Light absorption generates electron-hole pairs; (II) Separation of excited charges and transfer of electrons and holes to the photocatalyst surface; (III) Utilization of surface charges for redox reactions.

Hollow structures offer a promising solution by leveraging unique geometric designs. Their multi-shell or cavity configurations enhance light harvesting through multiple internal reflections, extending the photon path length and improving capture efficiency [49]. This concept pioneered by Li, Lu et al. in 2007 using hierarchical sphere-in-sphere TiO_2, demonstrated enhanced UV photon utilization and significantly improved phenol degradation [189]. Furthermore, the high specific surface area of hollow structures provides abundant active sites, while thin shell layers shorten carrier migration distances, suppressing recombination. For instance, Fe_3O_4@TiO_2 core-shell hollow structures exhibit superior RhB degradation compared to P25 TiO_2 and enable facile magnetic separation [190]. Hollow structure design combined with non-metallic element doping is an effective strategy for tailoring the electronic structure and bandgap of photocatalysts, significantly boosting efficiency [191].

Graphitic carbon nitride (g-C_3N_4), a metal-free semiconductor, has attracted considerable attention due to its low cost, earth abundance, suitable bandgap, and excellent chemical stability [192]. Numerous non-metal doped g-C_3N_4 catalysts and heterostructures now surpass pristine g-C_3N_4 in performance [191].

Liu et al. reported the fabrication of a highly efficient three-dimensional hollow porous carbon nitride (CPCN) catalyst via synergistic morphological engineering and *in situ* carbon doping (**Figures 12a-c**). The resultant CPCN material exhibited a significantly enhanced diclofenac degradation rate of $20.3\times10^{-3}\cdot min^{-1}$ under visible light irradiation (**Figure 12d**) and superior hydrogen evolution performance at a rate of 16.69 $mmol\cdot g^{-1}\cdot h^{-1}$ (**Figure 12e**). Structural characterization combined with density functional theory (DFT) simulations revealed that the hierarchical 3D hollow porous architecture imparts CPCN with a large specific surface area and abundant exposed active sites, concurrently enhancing substrate adsorption kinetics and structural integrity. Furthermore, *in situ* carbon doping modulated the optical absorption properties of CPCN, thereby promoting efficient charge carrier separation and migration. These synergistic structural and compositional modifications collectively contribute to the exceptional photocatalytic performance of the CPCN catalyst [193].

Similarly, Zheng et al. achieved precise optimization of graphitic carbon nitride (g-C_3N_4) structure and properties through controlled precursor composition and synthesis methodology. As illustrated in **Figure 12f**, samples were prepared via distinct routes: (U) urea thermal polymerization, yielding a porous structure from gaseous decomposition products; (M) direct thermal polymerization of melamine, resulting in a dense layered structure with minimal porosity; (MC) thermal decomposition of a melamine-cyanuric acid supramolecular complex, where cyanuric acid templating generated an open porous framework with a specific surface area (52.2 $m^2\cdot g^{-1}$) and pore volume (0.37 $cm^3\cdot g^{-1}$) increased 8.0-fold and 6.6-fold, respectively, relative to M; ($MCB_{0.07}$) carbon-doped MC via barbituric acid incorporation into the supramolecular framework via hydrogen bonding, followed by N-site carbon doping

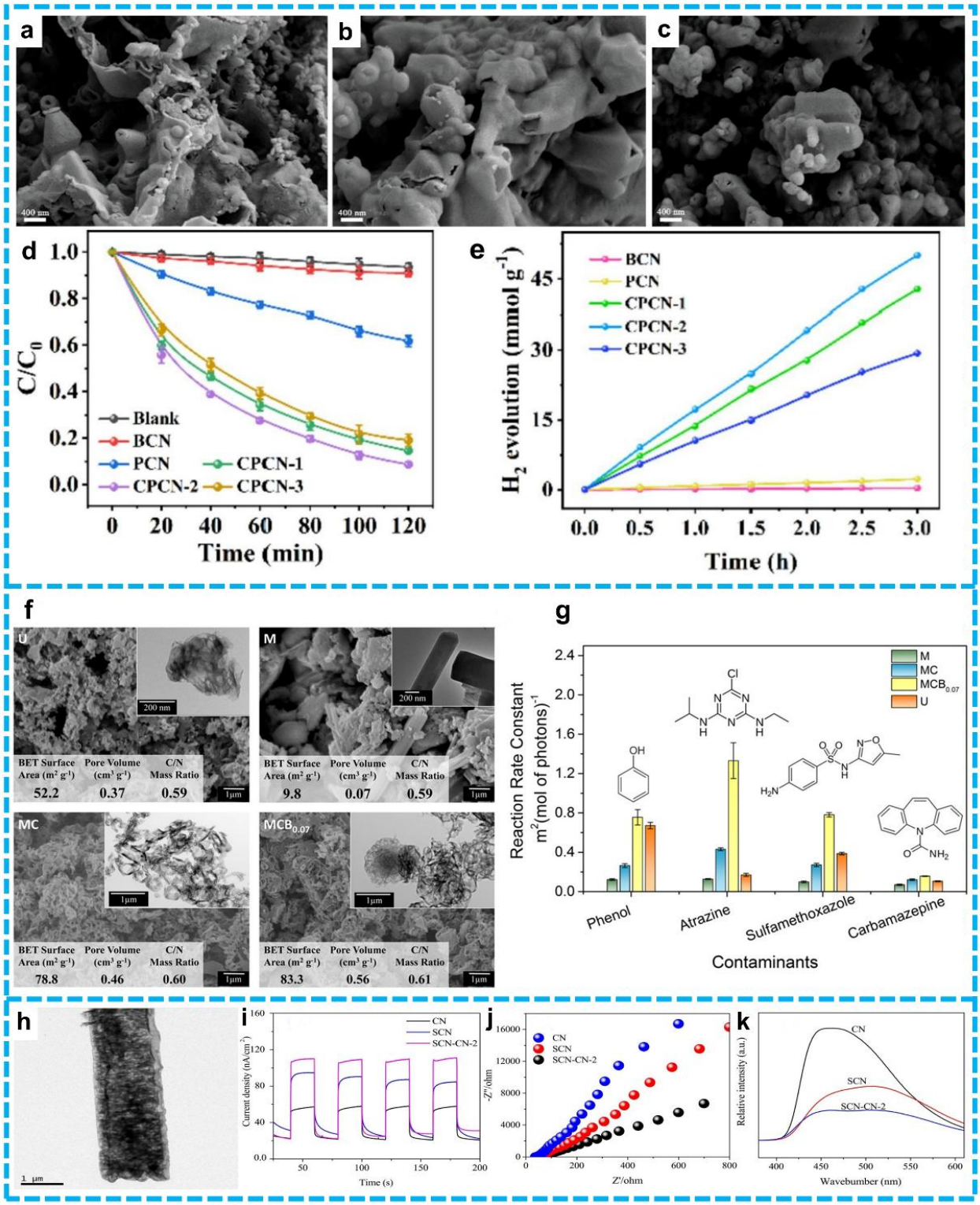

Figure 12 SEM images of a) CPCN-1, b) CPCN-2, c) CPCN-3; d) Photocatalytic degradation of DCF by the as-prepared samples; e) H_2 generation of the BCN, PCN and CPCN catalysts [193]. Copyright 2022, Elsevier. f) SEM and TEM (insets) images of g-C_3N_4 samples U, M, MC, and $MCB_{0.07}$; g) Photocatalytic degradation rate constants of U, M, MC, and $MCB_{0.07}$ [194]. Copyright 2016, American Chemical Society. h) TEM images of SCN-CN-2, The photocurrent (i), EIS (j), and PL k) of as-prepared samples [195]. Copyright 2021, Elsevier.

during thermal polymerization, further increasing specific surface area (78.8 $m^2 \cdot g^{-1}$), pore volume (0.46 $cm^3 \cdot g^{-1}$), and the C/N mass ratio (0.61 vs. 0.60 for MC), confirming successful doping. These structural variations directly governed photocatalytic activity (**Figure 12g**): M exhibited the lowest degradation rates due to limited active site accessibility. The porous structure of MC enhanced pollutant adsorption and mass transfer, substantially increasing reaction kinetics relative to M. $MCB_{0.07}$ demonstrated synergistic optimization, combining the porous structure with carbon doping to enhance charge separation efficiency (evidenced by lower photoluminescence intensity versus MC), yielding degradation rate constants for atrazine and sulfamethoxazole of 0.59 and 0.61 $m^2 \cdot (mol\ photons)^{-1}$, respectively—nearly double those of MC (0.30 $m^2 \cdot (mol\ photons)^{-1}$)—and phenol degradation activity comparable to U (0.37 vs. 0.32 $m^2 \cdot (mol\ photons)^{-1}$). This study demonstrates that carbon doping enhances the photocatalytic oxidation capacity of g-C_3N_4 by modulating the band structure (e.g., inducing a more negative conduction band potential favorable for $\cdot O_2^-$ generation) and increasing surface defects, providing robust experimental support for non-metallic doping strategies in environmental remediation [194].

Furthermore, Liang et al. engineered a highly active hollow tubular g-C_3N_4 isostructural heterojunction (SCN-CN, **Figure 12h**) to augment visible-light harvesting and regulate directional charge transfer. Ultraviolet-visible diffuse reflectance spectroscopy (UV-Vis DRS), XPS band structure analysis, and DFT calculations collectively demonstrate that sulfur doping enhances visible-light absorption relative to pristine g-C_3N_4 (CN) and modifies the band structure, promoting photoexcited electron migration from CN to SCN and hole transfer from SCN to CN under visible light. Concurrently, the tubular architecture facilitates longitudinal electron transport along the tube axis, suppressing carrier recombination. Consequently, the SCN-CN-2 heterojunction achieved optimal charge separation efficiency, evidenced by the strongest photocurrent response (**Figure 12i**), smallest electrochemical impedance arc (**Figure 12j**), and lowest photoluminescence intensity (**Figure 12k**). The integrated experimental and theoretical approach systematically elucidated the optical characteristics, electronic structure, and charge transfer dynamics of SCN-CN. Rigorous evaluation under simulated visible light irradiation confirmed the enhanced photocatalytic degradation efficiency of SCN-CN towards model pollutants tetracycline hydrochloride (TCH) and rhodamine B (RHB) [195].

4. *In Situ* Testing Techniques Combined with First Principles Calculation in Hollow-structured Materials

Following the detailed elaboration on the various synthesis methods and application scenarios of hollow-structured materials in the preceding sections, it is equally critical to investigate the underlying mechanisms during their application. A profound understanding of these mechanisms enables the further rational functionalization and modification of the materials, enhancing their suitability for specific application requirements.

The exploration of these mechanisms necessitates the indispensable application of diverse characterization techniques. With the continuous development of material modification methods and the increasing complexity of chemical reaction systems, the demands placed on characterization techniques have become more stringent. Beyond ex situ characterization techniques such as X-ray diffraction (XRD), scanning electron microscopy (SEM), transmission electron microscopy (TEM), X-ray photoelectron spectroscopy (XPS), electrochemical impedance spectroscopy (EIS), photoluminescence (PL) spectrum, time-resolved photoluminescence (TRPL), ultraviolet-visible (UV-vis) spectrum, incident photon-to-current conversion efficiency (IPCE), DMPO spin-trapping electron paramagnetic resonance (EPR), surface photovoltage (SPV), and *in situ* diffuse reflectance infrared Fourier transform spectroscopy (DRIFTS), which characterize and determine the intrinsic state of materials. Various quasi *in situ* and *in situ* characterization techniques are becoming increasingly pivotal for exploring reaction mechanisms under real-time operating conditions. The following sections will partially detail the principles of corresponding *in situ* techniques combined with first principles calculation for mechanistic analysis, specifically addressing the application scenarios and reaction systems of hollow-structured materials discussed previously [196-200].

4.1 *In Situ* Irradiation X-ray Photoelectron Spectroscopy (ISI-XPS) Facilitates Exploration of Intrinsic Mechanisms

Scientific community has increasingly acknowledged the critical importance of elucidating the pathways of

photogenerated electrons at material interfaces during photocatalytic processes. A fundamental understanding of these charge carrier dynamics is indispensable for developing mechanistic insights into photocatalytic phenomena and establishing rational design principles for advanced photocatalyst architectures [201]. XPS is a surface-sensitive analytical method conventionally employed to probe element-specific chemical environments, inherently captures electronic structure modifications, and initially focused primarily on determining the directionality of electron flow across interfaces. In this context, in-situ irradiated X-ray photoelectron spectroscopy (ISI-XPS) has emerged as a particularly promising technique for the direct detection of photogenerated electron transfer dynamics [202, 203]. As comprehension of the technique matured, researchers recognized its utility for emerging research exploring parameters such as excitation wavelength, binding energy shifts, and quantitative electron transfer volumes suggests ISI-XPS holds significant potential for deeper exploration within the photocatalysis domain. To date, ISI-XPS has been successfully applied to characterize diverse systems, including hollow structured heterostructure catalysts. The fundamental insights derived from such studies are paramount for driving continuous innovation and accelerating the development of next-generation catalytic materials.

4.1.1 The ISI-XPS Instrument Fundamental Principles

During spectral acquisition, the sample surface is irradiated with photons of precisely defined energy. The core-level binding energy (E_{be}) of the emitted photoelectrons is derived directly from their measured kinetic energy (E_{ke}) using Einstein's photoelectric equation: $E_{be}=h\nu-E_{ke}$, where $h\nu$ is the energy of the incident monochromatic X-ray photon [204, 205]. A fraction of the photoelectrons generated near the sample surface are emitted into the vacuum. These electrons traverse the electron optics and are subsequently focused through the entrance slit of the spectrometer analyzer. The spectrometer is designed to measure the electron current (proportional to the number of electrons per unit time) as a function of kinetic energy. The resulting plot of electron intensity versus binding energy constitutes the XPS spectrum. X-ray irradiation is confined with the maximum information depth typically limited to approximately 10 nm. The most intense peak within an element's spectrum is designated as its characteristic peak, thereby providing definitive elemental identification.

The ISI-XPS analysis is performed utilizing a standard XPS instrument equipped with an integrated illumination accessory, as depicted in **Figure 13a-c**. The initial measurement is conducted under dark conditions to establish the baseline binding energy (BE). Subsequently, the excitation wavelength is then selected to correspond with the characteristic absorption wavelength of the sample material, enabling the commencement of in-situ testing. Irradiation of a semiconductor photocatalyst with photons possessing energy equal to or exceeding its bandgap induces electronic excitation. This process generates photogenerated charge carriers (electrons and holes), promoting electrons from the valence band to the conduction band and creating reactive species, leading to localized alterations in electron density (**Figure 13d-f**) [206].

The shielding effect theory provides the framework for interpreting BE shifts. An increase in electron density within the outer atomic layers attenuates the effective nuclear charge experienced by core-level electrons. This reduced electrostatic attraction consequently enhances the kinetic energy of the emitted photoelectrons. According to the Einstein's photoelectric equation ($E_{be}= h\nu -E_{ke}$), under constant excitation energy ($h\nu$), an increase in kinetic energy necessitates a concomitant decrease in binding energy. Conversely, a reduction in kinetic energy corresponds to an increase in binding energy. Consequently, variations in electron density manifest directly as shifts in core-level binding energies. Electron depletion (reduced electron density) results in a positive BE shift (increase), typically observed for the primary catalyst element. Conversely, electron accumulation (increased electron density) yields a negative BE shift (decrease). Analysis of these BE shifts` thus allows for the determination of the directionality of electron flow between the constituent materials under simulated illumination conditions.

4.1.2 The Application of ISI-XPS in Hollow-structured Materials

The use of multi-level structures can also serve to maximize the inhibition of photo-generated charge recombination and maximize the utilization of electrons.

Zhang et al. constructed a multi-level separation yolk-shell hollow structure (**Figure 14a, b**), $SiO_2/Ni_2P/rGO/Cd_{0.5}Zn_{0.5}S$ [208], for photo generated electrons, which maximized the inhibition of photo generated electron recombination. The photocatalytic performance test showed that the activity of this multi-level separation structure is about 14 times higher than that of pristine $Cd_{0.5}Zn_{0.5}S$ (**Figure 14c, d**). The stability test in Figure h also indicated that this structure can exist stably in catalytic reactions, and the hollow structure would not collapse with the progress of the reaction. The results of ISI-XPS testing indicated

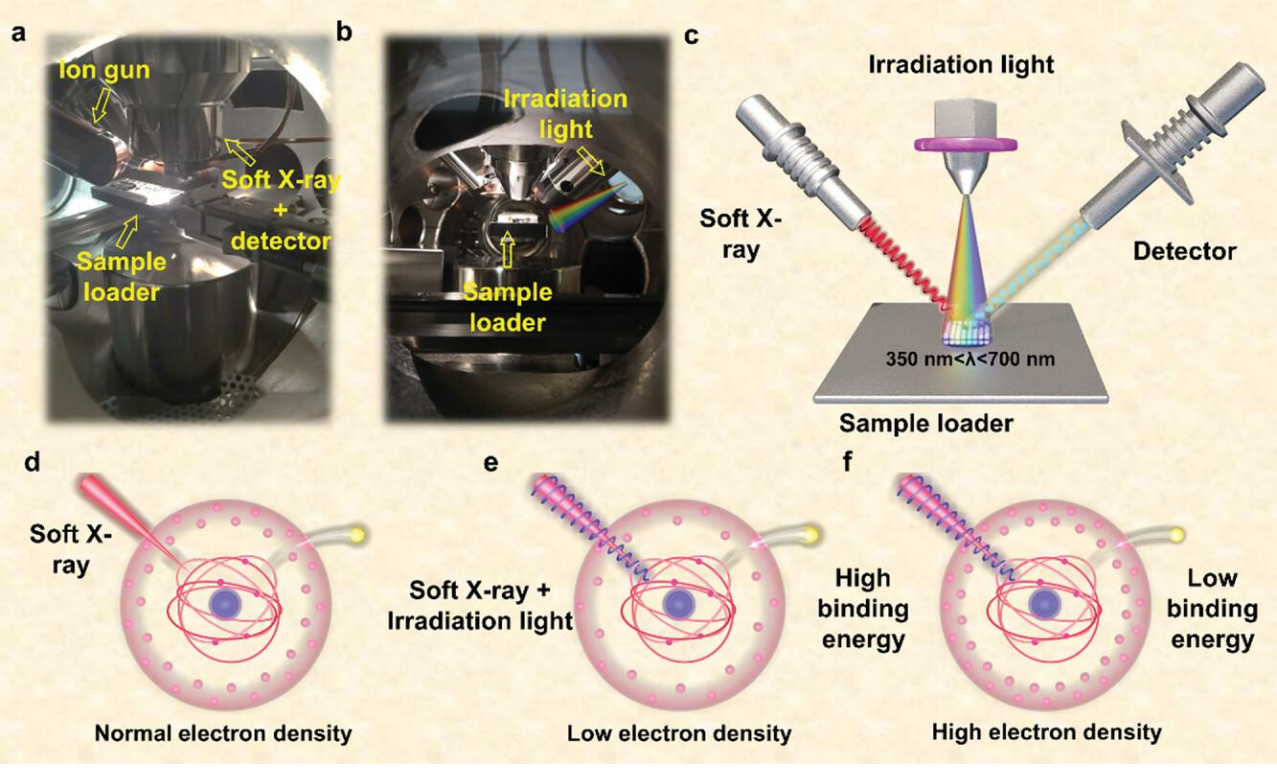

Figure 13 a) Front windows photographs of ISI-XPS device; b) Side windows photographs of ISI-XPS device; c) Schematic illustration of ISI-XPS device; d-f) Effect of electron density on binding energy [207]. Copyright 2022, John Wiley and Sons.

that the photo generated electrons generated by $Cd_{0.5}Zn_{0.5}S$ flow towards Ni_2P through rGO (**Figure 14e-g**), achieving the separation of photo generated charge carriers. The energy level structure verifies the migration direction of electrons (**Figure 14i**), and **Figure 14j** shows the mechanism by which this multi-level structure enhances catalytic activity.

Li et al. established a g-C_3N_4/SnO_2 as a model heterostructure photocatalyst to investigate the relationship between binding energy and incident wavelength [209]. The morphology characterization represented g-C_3N_4 was coated at the surface of SnO_2 nanoparticles (**Figure 15a, e**). After verifying the synthesis of photocatalyst, the ISI-XPS equipped with a continuous tunable wavelength light source was carried out. **Figure 15b-d** showed the results of Sn 3d in SnO_2, composite photocatalyst and calibrated results of composite photocatalyst, respectively. It could be seen that the change in binding energy increased as the wavelength got shorter. In this situation, a Boltzmann function was proposed to describe the relationship between binding energy changes and irradiated wavelength (**Figure 15g**). Besides, in **Figure 15f**, an asymptotic function model was also offered to describe the relationship between binding energy and element valence states, achieving preliminary research on electron quantification. This study is the inaugural investigation into the alterations in binding energy as a function of light sources with disparate wavelengths. It has uncovered the intrinsic correlation between binding energy, valence state, and wavelength.

4.2 *In Situ* Surface Attenuated Total Reflection Fourier Transform Infrared Spectroscopy (ATR-FTIR) Combining with First Principles Calculation Facilitates Exploration of Intrinsic Mechanisms.

Researchers have elucidated diverse perspectives on electrocatalytic mechanisms from both thermodynamic and kinetic viewpoints, employing a variety of advanced techniques. *In situ* spectroscopy further serves as a critical experimental approach, enabling real-time monitoring of dynamic evolution in catalyst surface structures and intermediate species during electrocatalytic processes. This capability makes it an indispensable tool for unraveling the fundamental reaction mechanisms in electrocatalysis. First-principles calculations, particularly those based on

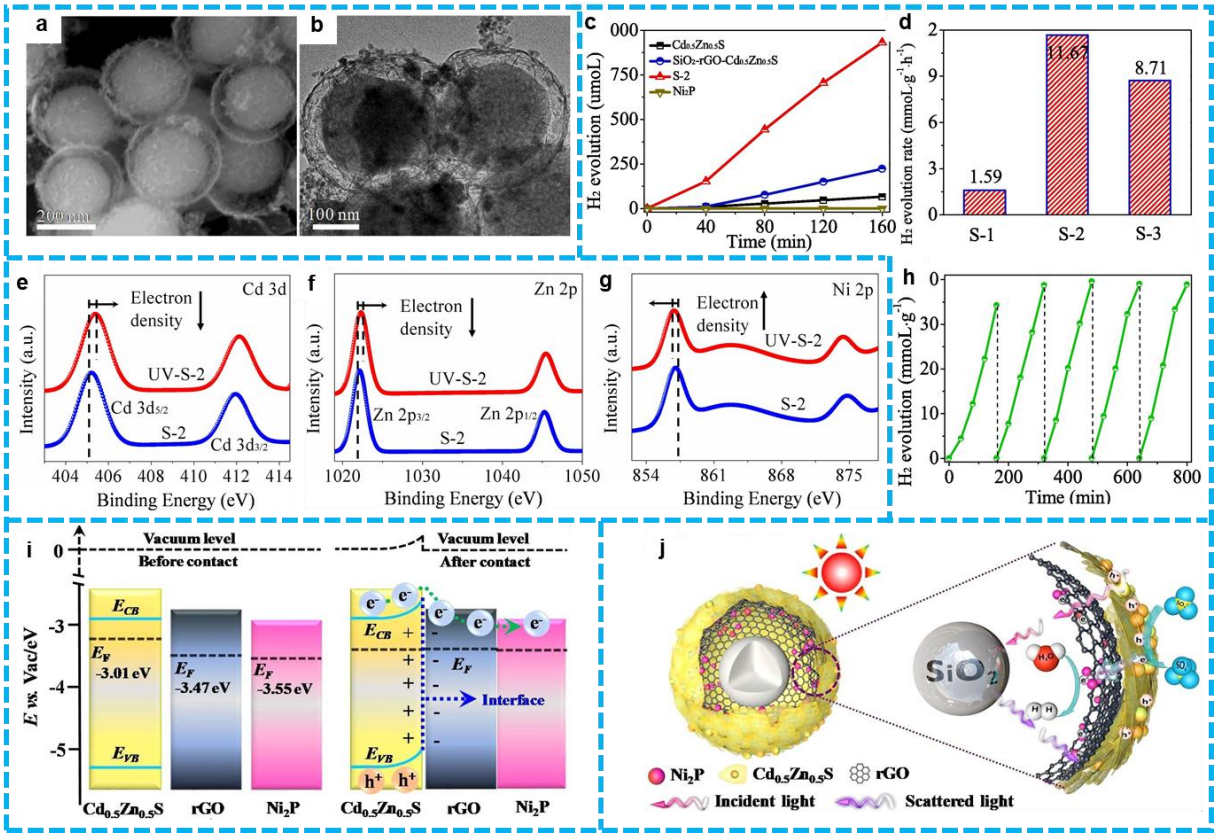

Figure 14 a) The SEM and b) TEM images of as-prepared yolk-shell structural $SiO_2/Ni_2P/rGO/Cd_{0.5}Zn_{0.5}S$ sample; c) The time dependent H_2 evolution over different samples; d) the H_2 production rate of different ration composites; h) recycling test over the S-2 composite under visible light irradiation, e-g) High-resolution XPS spectra of the S-2 composite in the dark and under LED irradiation (λ=365 nm): Cd 3d, Zn 2p and Ni 2p; i) Band structure diagram of the $Cd_{0.5}Zn_{0.5}S$, rGO and Ni_2P; j) Photocatalytic mechanism of H_2 generation in the yolk-shell structural $SiO_2/Ni_2P/rGO/Cd_{0.5}Zn_{0.5}S$ nanoreactor [208]. Copyright 2021, Elsevier.

density functional theory (DFT) [1, 210, 211], have become an indispensable and powerful tool in modern materials science and catalysis research. Rooted in the fundamental principles of quantum mechanics, this approach relies on no empirical parameters and predicts various material properties solely based on atomic species and spatial arrangements. It allows researchers to probe the intrinsic characteristics of materials and chemical reaction processes at the atomic and electronic levels, thereby enabling the rational design of material functions and offering profound insights into catalytic mechanisms.

4.2.1 ATR-FTIR Fundamental Principles

ATR-FTIR is a highly sensitive detection technique developed based on the surface enhanced infrared absorption (SEIRA) effect. The SEIRA effect refers to the phenomenon in which metal island films significantly enhance the infrared absorption intensity of surface-adsorbed molecules [212]. It was first observed by Hartstein et al. during their study of the adsorption behavior of p-nitrobenzoic acid molecules on Au and Ag Island films [213]. The electromagnetic field mechanism postulates that when incident infrared light irradiates a rough metal surface, the free electrons on the metal surface oscillate under the influence of the optical electric field, giving rise to localized surface plasmon resonance (LSPR). This results in a significant enhancement of the local electromagnetic field intensity at the metal surface. The localized electromagnetic field is polarized perpendicularly to the metal surface and its strength decays exponentially with increasing distance from the surface. As a consequence, the effective enhancement distance of the SEIRS effect is limited to within 10 nm. This characteristic precisely enables SEIRAS to minimize interference from the bulk solution. This surface selection rule allows SEIRAS to elucidate the orientation of molecules adsorbed on the surface [214, 215]. The core of the chemical enhancement mechanism lies in the interaction between adsorbed molecules and

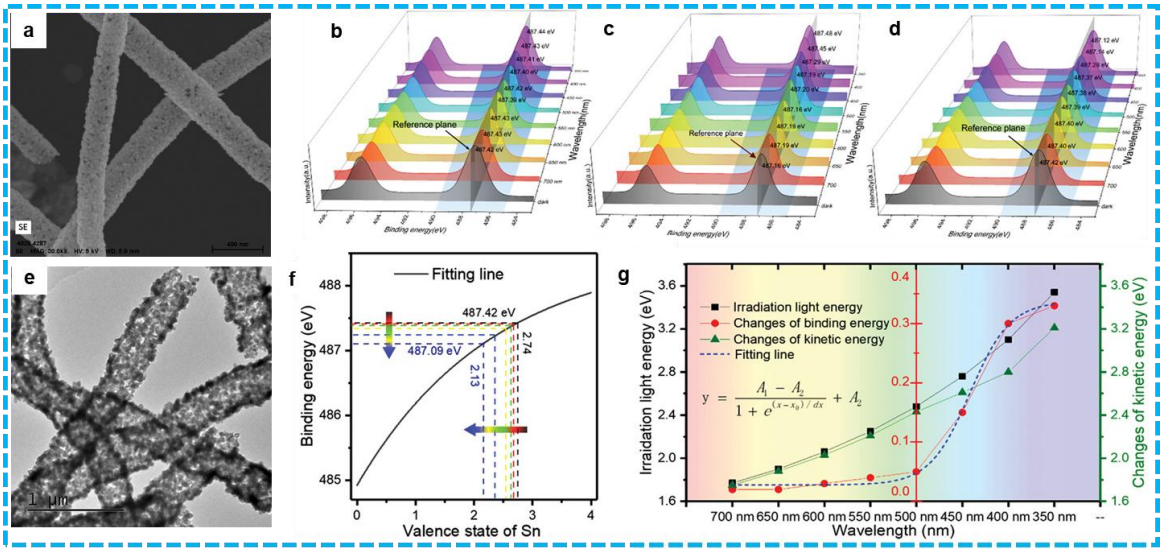

Figure 15 a) The SEM image of g-C_3N_4/SnO_2; e) HRTEM of g-C_3N_4/SnO_2; b) ISI-XPS result of g-C_3N_4/SnO_2 before charge compensation; c) ISI-XPS result of SnO_2; d) ISI-XPS result of g-C_3N_4/SnO_2 after charge compensation; f) The fitting curve of the relation between binding energy and valence state of Sn element in g-C_3N_4/SnO_2; g) Relationship of irradiation light energy, changes of binding energy, and kinetic energy of Sn $3d_{5/2}$ in g-C_3N_4/SnO_2. [209]. Copyright 2023, Elsevier.

atoms on the metal surface. Resonance occurs when the energy of the incident light matches the energy difference required for this charge transfer process. This leads to an increase in the vibrational dipole moment of the adsorbed molecules, thereby enhancing the infrared absorption signal [216].

SEIRAS has attracted significant attention owing to its unique technical advantages, including high sensitivity, the ability to determine molecular orientation, minimal interference from electrolyte solutions, and the compatibility of metallic thin films as working electrodes in electrochemical systems. These attributes have established SEIRAS as a powerful tool for investigating electrochemical interfaces, and it is now widely applied in studies of electrocatalysis, electrode reaction mechanisms, and surface adsorption processes.

To leverage the SEIRA effect in practical research, various operational modes of SEIRAS have been developed, including transmission mode [217], external reflection mode [218], and attenuated total reflection (ATR) mode [219]. The attenuated total reflection (ATR) mode employs a high-refractive-index crystal (e.g., ZnSe, Si, or Ge) as an internal reflection element. When infrared light is directed onto the crystal surface at an angle greater than the critical angle, total internal reflection occurs. During this process, an evanescent wave penetrates into the sample and interacts with molecules adsorbed on the nanostructured metal surface, thereby enhancing the infrared absorption signal, as depicted in **Figure 16** [220].

Compared to transmission and external reflection SEIRAS techniques, ATR offers effective suppression of solvent interference, lower background absorption, reduced detection limits, higher signal-to-noise ratio, and superior sensitivity. Owing to these advantages, ATR-FTIR has been widely adopted in studies of electrochemical systems [212]. A schematic diagram of the *in situ* ATR-FTIR experimental setup is shown in **Figure 17**.

4.2.2 The Application of SEIRAS Combining with First Principles Calculation for Elucidation of Catalytic Mechanisms

Conventional electrochemical techniques, such as Tafel slope analysis, exhibit limitations in distinguishing subtle differences in microscopic pathways during catalytic processes. In contrast, SEIRAS capitalizes on the localized surface plasmon resonance (LSPR) effect of metallic thin films to significantly enhance the infrared signals of adsorbed species, thereby facilitating the detection of intermediates even at low surface coverages [223]. Furthermore, SEIRAS can be coupled with an electrochemical workstation to monitor in real time the vibrational characteristics of intermediates adsorbed on the electrode surface (e.g., *H, *OH), providing critical insights into the reaction mechanism [224].

Structural engineering has been demonstrated as an effective strategy to enhance the performance of catalysts [225, 226]. Wang et al. [227] developed a facile galvanic replacement strategy to synthesize octahedral

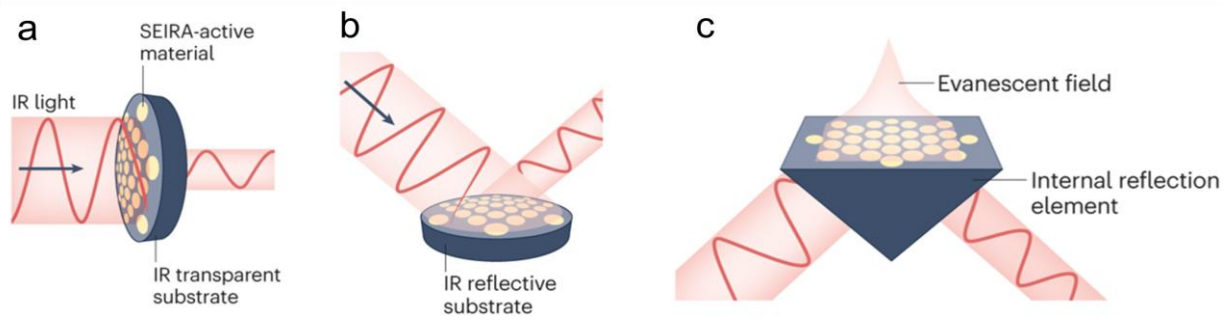

Figure 16 Schematic illustration of the three primary SEIRAS techniques: a) transmission mode, b) external reflection mode, and c) attenuated total reflection (ATR) mode [221].

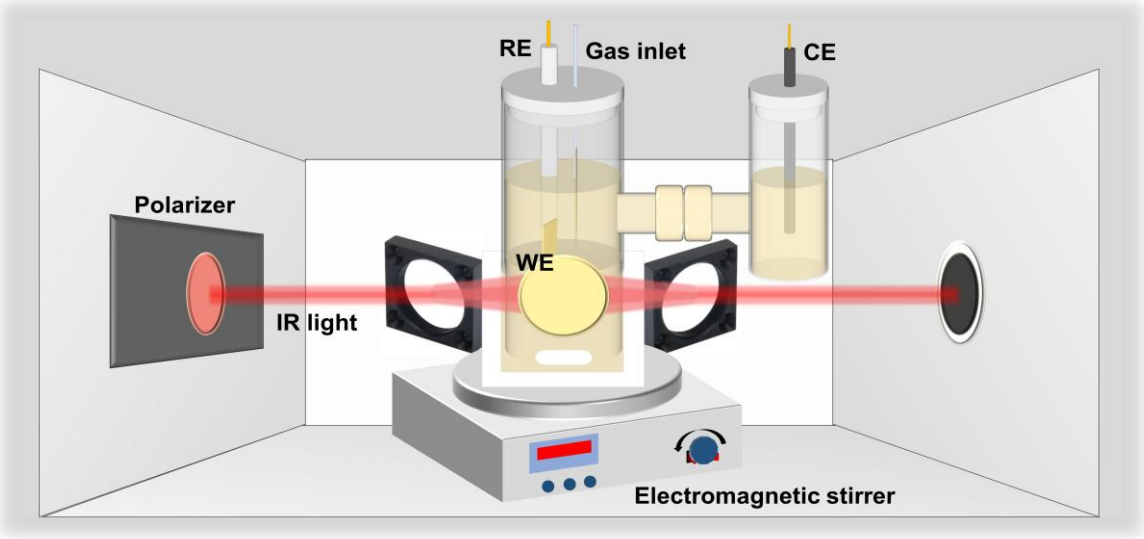

Figure 17 Schematic diagram of an *in situ* electrochemical ATR-FTIR setup equipped with stirring capability [222].

PdRuCu nanocages (NCs) (**Figure 18a**) using Cu_2O octahedra as templates, offering dual advantages: (1) significantly improved atom utilization efficiency, thereby reducing overall catalyst costs [228]; and (2) simultaneous accessibility of both external surfaces and internal cavities to reactant molecules, which not only maximizes the electrochemically active surface area but also promotes mass transport, ultimately accelerating kinetics [229]. *In situ* FTIR reveals that the introduction of Ru favors OH adsorption, thereby promoting CO oxidation in **Figure 18b-c**. This work presents a simple yet effective strategy for designing high-performance catalysts with superior efficiency and low production costs, offering significant potential for practical applications. Density functional theory (DFT) calculations indicate that the co-adsorption of CO and OH species on PdRuCu NCs enables electron interaction between OH and CO species in **Figure 18d-h**, facilitating the formation of CO_2 through synergistic effect. **Figure 18e** presents the free energy landscape (ΔG) for the Langmuir-Hinshelwood type CO oxidation mechanism on both catalytic surfaces. Thermodynamic analysis reveals spontaneous chemisorption of reactants, with CO exhibiting stronger binding affinity on Pd_3Cu_4 ($\Delta G = -1.2$ eV) compared to Pd_3RuCu_4, while OH species show preferential stabilization on the Ru-modified surface ($\Delta G = -0.8$ eV). This reduced kinetic bottleneck correlates with the experimentally observed enhancement in FAOR activity, where the Ru-alloyed Pd catalyst achieves a high current efficiency at 0.3 V vs RHE. The attenuated CO binding strength (−0.8 eV vs −1.2 eV) coupled with optimized OH activation energetics creates a synergistic effect that simultaneously mitigates CO poisoning while accelerating the CO_2 desorption kinetics.

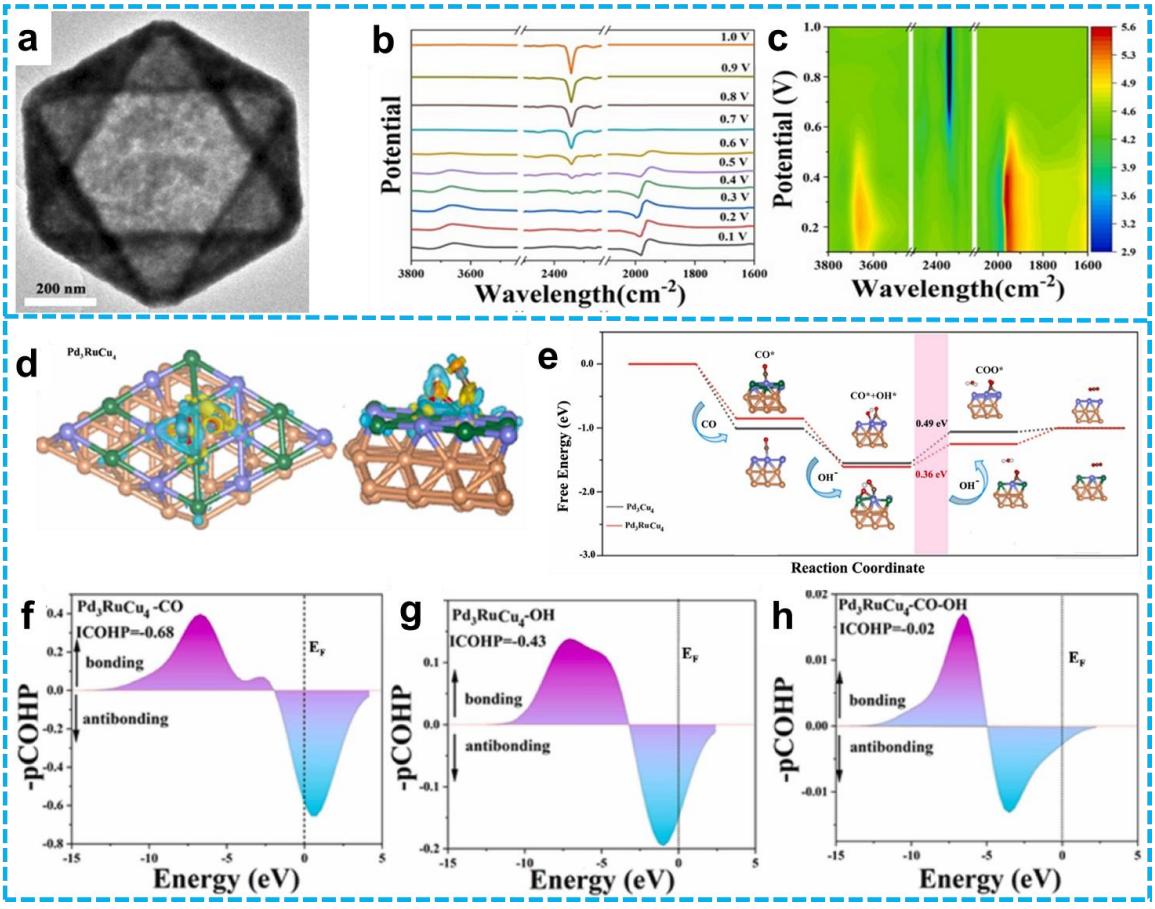

Figure 18 a) TEM images of Pd_3RuCu_4 NCs; *In situ* FTIR spectral analysis of adsorbed species on Pd_3RuCu_4 NCs: b) FTIR spectra and c) contour maps of OH, CO, and CO_2 adsorption; d) Local charge density difference of CO co-adsorbed with OH; e) Energy profile comparison for CO oxidation to CO_2; f) Crystal orbital Hamilton population (pCOHP) analysis: g) CO adsorption, h) OH adsorption. [227]. Copyright 2025, Elsevier.

Zhang et al. [230] strategically engineered atomically dispersed cobalt-copper diatomic pairs anchored on CeO_2 hollow nanostructures (**Figure 19a**) to systematically investigate the interplay among coordination architecture, metal-support interactions, and their collective influence on OER/ORR. The influence of the mechanism pathway on the adsorption of reaction intermediates is measured by *in situ* Fourier transform infrared (FTIR) spectroscopy. The *in situ* FT-IR spectra of CoCu@CeO_2 for OER (in 1.0 m KOH) and ORR (in O_2-saturated 0.1 m KOH solution) are shown in **Figure 19b-c**. During OER, an infrared absorbed peak of *OOH (at ≈1230 cm^{-1}) appeared under anodic potentials and gradually enhanced when the voltage applied changed from 1.2 to 1.8 V. The increase of *OOH intermediates corroborated the traditional four-step adsorbate evolution mechanism reaction pathway of the CoCu@CeO_2 catalyst. In addition, under ORR operating conditions, there are four absorption peaks. As the applied voltage decreases, the intensity of the peak at 1180 cm^{-1} increases gradually, suggesting that the coupling of *OOH species is a dynamic process. The absence of peroxo-like oxygen (*O—O*) at ≈1090 cm^{-1} confirms that CoCu@CeO_2 catalysts follow the $4e^-$ associative ORR pathway. This work proposes a novel mechanism for engineering dual-atom architectures through long-range electronic interactions, providing valuable insights into the advancement of advanced electrocatalysts for sustainable energy conversion systems. In **Figure 18d-g,** systematic DFT simulations further demonstrated that the LRS coupling between bimetallic centers induces significant electronic structure modifications, including optimized d-bandcenter positions and reduced energy barriers compared to single-atom counterparts. The synergistic

interplay between geometrically optimized active sites and enhanced metal-support charge transfer simultaneously facilitates oxygen intermediate adsorption/desorption kinetics. This atomic-level engineering of heteronuclear diatomic systems not only offers deep insights into long-range electronic correlations in oxide-supported catalysts but also establishes a novel framework for atomic-level catalyst design in advanced energy conversion technologies [231, 232].

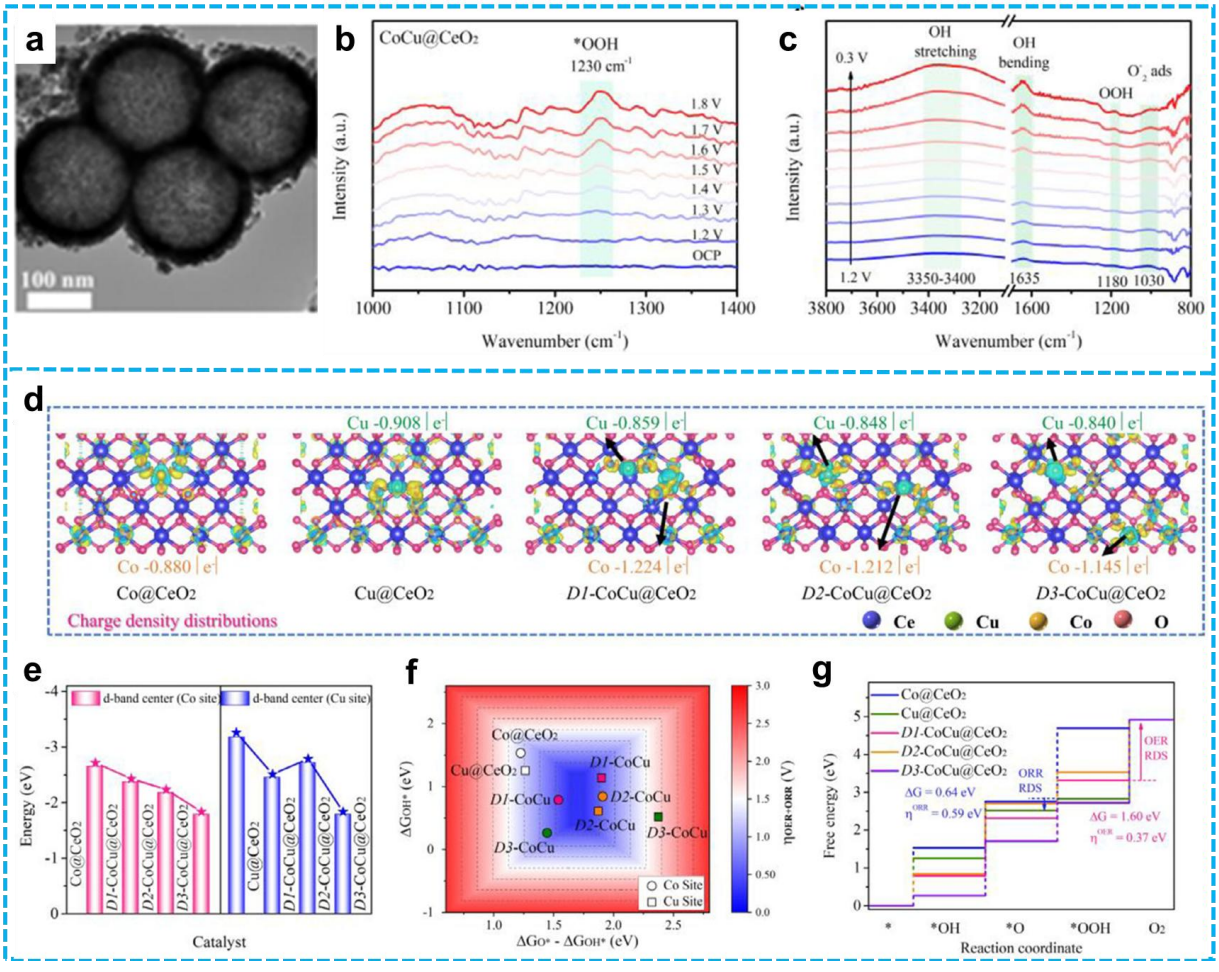

Figure 19 a) TEM images of $CoCu@CeO_2$; *In situ* FT-IR spectra of $CoCu@CeO_2$ for b) OER and c) ORR; Theoretical calculation: d) Charge density distributions and Bader charge at the Co and Cu sites; e) the d-band center at the Co and Cu sites for $Co@CeO_2$, $Cu@CeO_2$, D1-$CoCu@CeO_2$, D2-$CoCu@CeO_2$, and D3-$CoCu@CeO_2$; f) Calculated total theoretical overpotential (η^{total}) volcano plot with $\Delta G_{O^*}-\Delta G_{OH^*}$ and ΔG_{OH^*} as descriptors; g) Theoretical overpotential of the catalyst for OER (at Co site) and ORR (at Cu site) for $Co@CeO_2$, $Cu@CeO_2$, D1-$CoCu@CeO_2$, D2-$CoCu@CeO_2$, and D3-$CoCu@CeO_2$ [230]. Copyright 2025, John Wiley and Sons.

Furthermore, Zhang et al. [233] designed hybrid $Co_{2.5}Ru_{0.5}O_x$ hollow nanotubes (**Figure 20a**) with abundant Co_3O_{4-x}-RuO_{2-x} interfaces by a self-assembled electrospinning method, the *in situ* Fourier transform infrared spectroscopy revealed that the unique hollow nanotube structure allows OH^- reactants to be readily adsorbed on both exterior and inner nanotube surfaces, providing a driving force for activating interfacial lattice oxygen participation mechanism (LOM). **Figure 20b-c** displayed the operando FTIR spectra of hybrid $Co_{2.5}Ru_{0.5}O_x$ and single-phase Co_3O_4 under different OER potentials. It is noteworthy that the OH^- absorption band of hybrid $Co_{2.5}Ru_{0.5}O_x$ was the maximum and became larger with increasing voltages, providing strong evidence for its excellent OH^- adsorption capability. In conclusion, the unique porous hollow nanotube structure endowed the hybrid $Co_{2.5}Ru_{0.5}O_x$ with an excellent OH^- adsorption capability to accelerate the OER, which could serve as a beneficial driving force to activate the underlying interfacial LOM. Combined LOM mechanism experiments and density functional theory (DFT)

calculations demonstrated the exceptional interfacial LOM processes on the self-optimized Co-O-Ru motifs through an interfacial oxygen-vacancy pathway (**Figure 20d-h**).

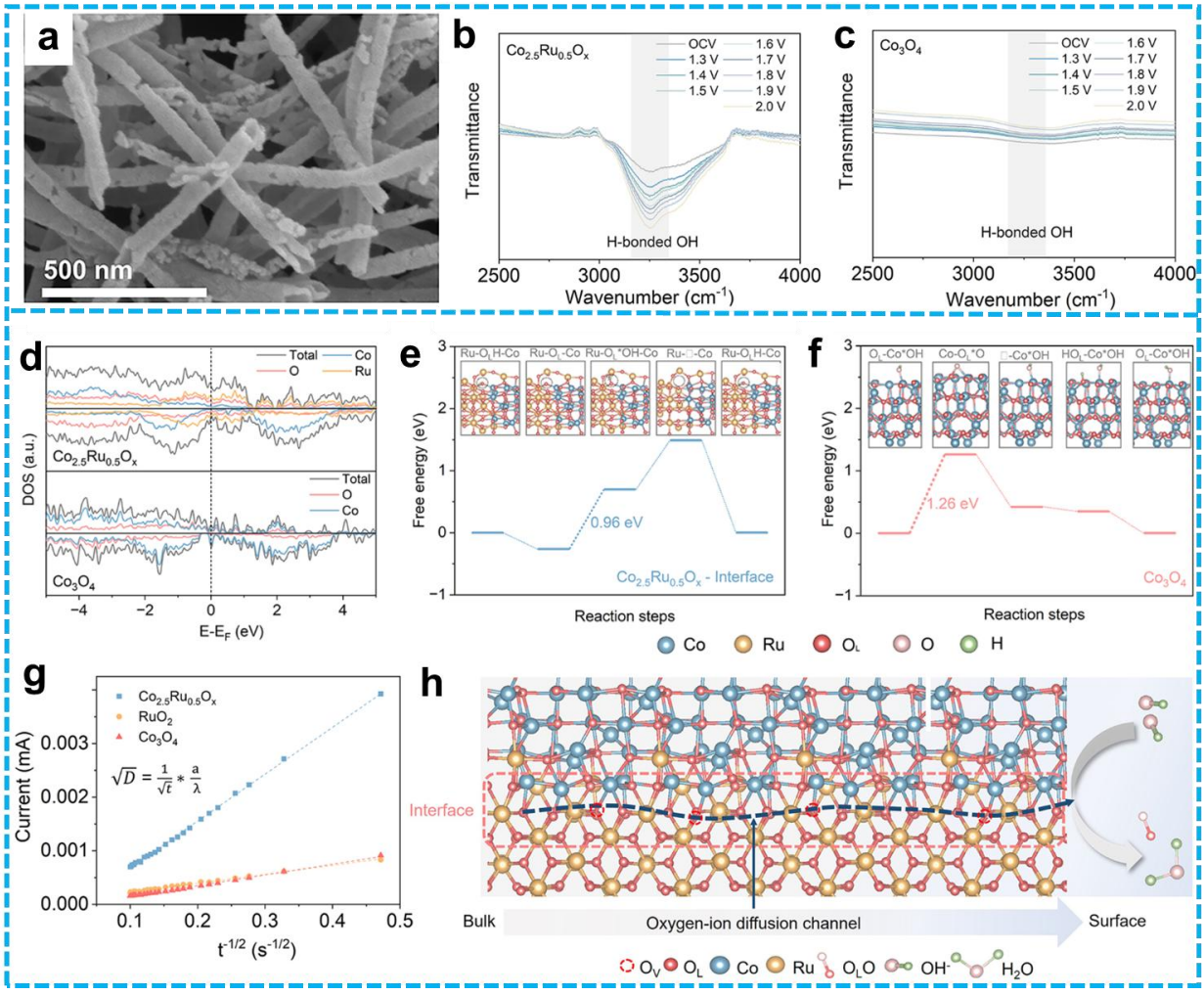

Figure 20 a) SEM image of hollow-nanotube hybrid $Co_{2.5}Ru_{0.5}O_x$ composites; b-c) *In situ* FTIR spectra of hollow-nanotube hybrid composites; d) DOS diagrams of hybrid $Co_{2.5}Ru_{0.5}O_x$ and Co_3O_4; Free energy diagram of the LOM pathway for e) hybrid $Co_{2.5}Ru_{0.5}O_x$ with Co-O-Ru interfaces and f) Co_3O_4; g) Chronoamperometry test of synthesized samples to calculate oxygen ion diffusion coefficients; h) Mechanistic diagram of lattice oxygen-ion diffusion at the Co_3O_{4-x}-RuO_{2-x} interface [233]. Copyright 2025, ACS Publications.

SEIRAS offers substantial experimental support for the investigation of electrocatalytic reaction mechanisms by virtue of its exceptional sensitivity and *in situ* characterization capability. This technique has proven particularly valuable in elucidating the behavior of adsorbed intermediate species. Evidence derived from SEIRAS-based studies has not only enhanced the fundamental comprehension of reaction pathways but has also provided a critical theoretical foundation for the rational design and development of novel, high-efficiency electrocatalysts, thereby accelerating progress within the field of electrocatalysis. High-throughput calculations can enhance the understanding of physical mechanisms by providing atomistic-level dynamic visualizations and quantitative energy descriptions. For surface catalytic reactions, such computations enable the simulation of different adsorption sites, elucidate reaction pathways and mechanisms, and evaluate catalyst performance descriptors. However, their accuracy is influenced by the choice of exchange-correlation functionals (e.g., the bandgap problem), the limited size of simulated systems (typically up to several hundred atoms), and short timescales (picoseconds to nanoseconds). Thus, they cannot fully replace experimental validation.

5. Summary and Outlook

Hollow nanostructures, distinguished by their intrinsic geometric advantages—including high specific surface area, tunable cavities, and reduced mass transfer lengths—alongside functional modularity, have emerged as transformative materials for energy storage and conversion [8, 210, 211, 234 -240]. This review systematically examines their design principles, synthetic methodologies, and application advancements in lithium-ion batteries, supercapacitors, lithium-sulfur batteries, and photo/electrocatalysis. Synergistic innovations in structural engineering and compositional design have effectively mitigated key challenges such as electrode volume expansion, polysulfide shuttling, and charge carrier recombination. Furthermore, hierarchical porosity, multi-shell configurations, and optimized heterointerfaces have significantly enhanced energy density and cycling stability. Nevertheless, critical challenges remain, including controllable synthesis, elucidation of structure-property relationships, and scalable implementation. Future research should prioritize:

i) Green, precise, and scalable synthesis: Develop green and low-cost templates (e.g., biomass-derived templates) or more intelligent template-free strategies. Explore novel synthetic techniques such as continuous-flow synthesis, microwave-assisted synthesis, and plasma-enhanced synthesis to achieve efficient, controllable, and scalable preparation. Integrate machine learning and artificial intelligence to optimize synthesis parameters through big data analysis, predict structure-property relationships, accelerate the discovery of new materials, and design synthesis pathways, thereby reducing trial-and-error costs [241-243].

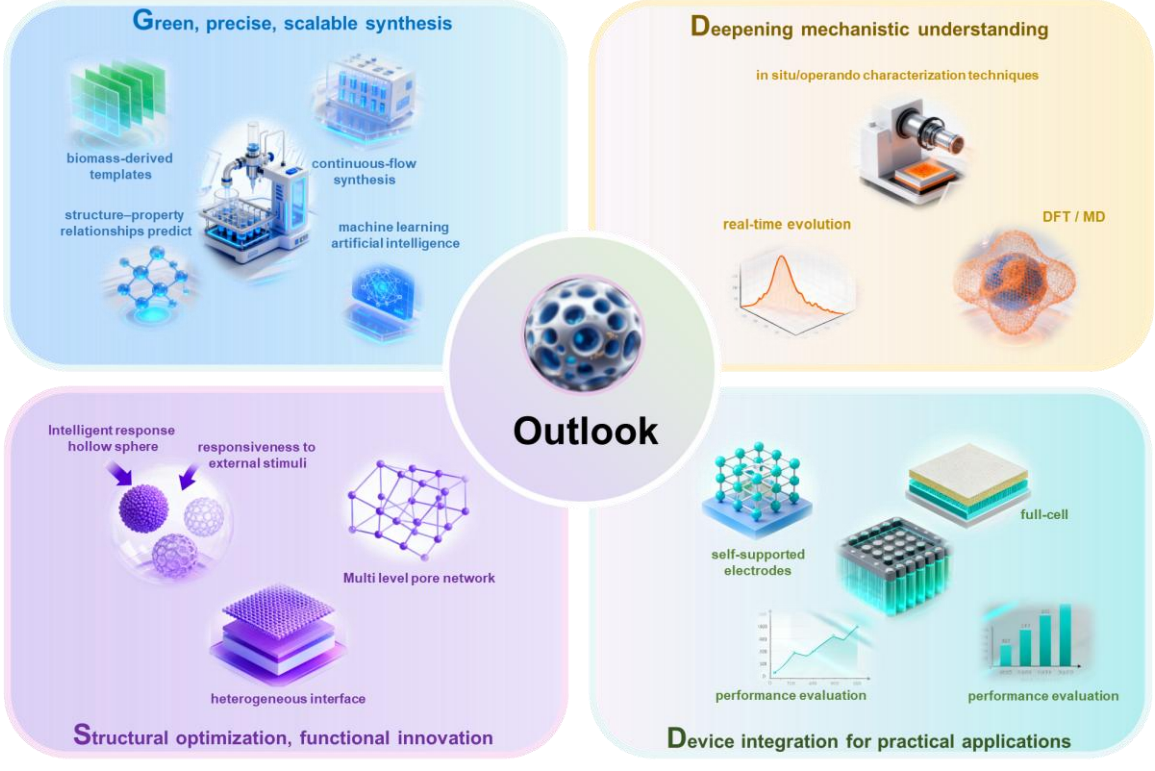

Figure 21 Outlook for future research on hollow structures.

ii) Structural optimization and functional innovation: Advance from simple "hollow" structures to intelligent and multifunctional architectures. For instance, design intelligent hollow structures with tunable shell permeability, self-healing capabilities, or responsiveness to external stimuli (light, heat, pH) [244]. Further refine the precise control of hierarchical porosity, gradient compositions, and heterogeneous interfaces to achieve synergistic effects among functional components.

iii) Deepening mechanistic understanding: Vigorously develop and utilize *in situ*/operando characterization techniques (e.g., *in situ* TEM, XRD, FTIR, SEM) to observe the real-time evolution of

structure, composition, and valence state of materials under working conditions, directly revealing failure mechanisms [245, 246]. Combine theoretical methods such as first-principles calculations (DFT) and molecular dynamics (MD) simulations to gain atomic- and electronic-level insights into mass/charge transfer processes and catalytic reaction mechanisms within hollow structures, providing theoretical guidance for precise design.

iv) Device integration for practical applications: Investigate methods to improve the tap density and electrode processing performance of hollow-structured materials, and explore the fabrication of self-supported electrodes that eliminate the need for inert binders. Enhance performance evaluation of hollow materials in full-cell/full-device configurations—rather than merely half-cell tests—focusing on overall energy density, cycle life, and safety under practical electrode coupling conditions [247-255].

Hollow-structured materials have emerged as a highly dynamic research direction in the field of energy. Future breakthroughs will hinge on close collaboration among chemistry, materials science, engineering, and theoretical computations to collectively address a series of scientific and technological challenges—from fundamental synthesis to practical applications—ultimately unlocking the socio-economic value of these high-performance materials.

CRediT author statement

Yiran Sun: Writing-original draft, Validation, Methodology, Investigation, Formal analysis, Data curation, Conceptualization.

Changqu Liu: Investigation, Formal analysis.

Shuqi Ji: Methodology, Investigation.

Jinbo Ni: Software, Data curation.

Xiangning Wu: Visualization.

Sembukuttiarachilage Ravi Pradip Silva: Validation, Resources.

Meng Cai: Supervision, Conceptualization.

Guosheng Shao: Supervision, Resources, Funding acquisition.

Peng Zhang: Supervision, Methodology, Funding acquisition, Conceptualization.

Acknowledgments

The work was supported by the National Natural Science Foundation of China (No. 52472110，U2004172, 51972287), the Central Plains Science and Technology Innovation Leading Talents (254200510052), the National Natural Science Foundation of Henan Province (No. 242300421008), and the Program for Science& Technology Innovation Talents in Universities of Henan Province (23HASTIT001).

Declaration of conflict of interest

The authors declare that they have no known competing financial interests or personal relationships that could have appeared to influence the work reported in this article. Peng Zhang is an Editorial Board Member of this journal and he was not involved in the editorial review or the decision to publish this article.

References

[1] Li Fangyi, Zhu Guihua, Jiang Jizhou, Yang Lang, Deng Fengxia, Arramel, Li Xin. A review of updated S-scheme heterojunction photocatalysts, Journal of Materials Science & Technology, 177 (2024) 142-180. https://doi.org/10.1016/j.jmst.2023.08.038.

[2] Zhu Ke, Li Xin, Chen Yuwen, Huang Yizhe, Yang Zhiyu, Guan Guoqing, Yan Kai. Recent advances on the spherical metal oxides for sustainable degradation of antibiotics, Coordination Chemistry Reviews, 510 (2024) 215813. https://doi.org/10.1016/j.ccr.2024.215813.

[3] Deng Fengxia, Jiang Jizhou, Sirés Ignasi. State-of-the-art review and bibliometric analysis on electro-Fenton process, Carbon Letters, 33 (2023) 17-34. http://doi.org/10.1007/s42823-022-00420-z.

[4] Li Neng, Yang Yufei, Shi Zuhao, Lan Zhigao, Arramel Arramel, Zhang Peng, Ong Wee-Jun, Jiang Jizhou, Lu Jianfeng. Shedding light on the energy applications of emerging 2D hybrid organic-inorganic halide perovskites, iScience, 25 (2022). http://doi.org/10.1016/j.isci.2022.103753.

[5] Zhou Hanghang, Ye Wenqiang, Jiang Jizhou, Wang Zheng. Recent advances on surface modification of non-oxide photocatalysts towards efficient CO_2 conversion, Carbon Letters, 34 (2024) 1569-1591. http://doi.org/10.1007/s42823-024-00748-8.

[6] Jiang Jizhou, Li Fangyi, Zou Jing, Liu Song, Wang Jiamei, Zou Yilun, Xiang Kun, Zhang Han, Zhu Guoyin, Zhang Yizhou, Fu Xianzhu, Hsu Jyh-Ping. Three-dimensional MXenes heterostructures and their applications, Science China Materials, 65 (2022) 2895-2910. http://doi.org/10.1007/s40843-022-2186-0.

[7] Li Fangyi, Jiang Jizhou, Wang Jiamei, Zou Jing, Sun Wei, Wang Haitao, Xiang Kun, Wu Pingxiu, Hsu Jyh-Ping. Porous 3D carbon-based materials: An emerging platform for efficient hydrogen production, Nano Research, 16 (2023) 127-145. http://doi.org/10.1007/s12274-022-4799-z.

[8] Jiang Jizhou, Li Fangyi, Ding Lei, Zhang Chengxun, Arramel, Li Xin. MXenes/CNTs-based hybrids: Fabrications, mechanisms, and modification strategies for energy and environmental applications, Nano Research, 17 (2024) 3429-3454. http://doi.org/10.1007/s12274-023-6302-x.

[9] Jiang Jizhou, Li Neng, Zou Jing, Zhou Xing, Eda Goki, Zhang Qingfu, Zhang Hua, Li Lain-Jong, Zhai Tianyou, T. S. Wee

Andrew. Synergistic additive-mediated CVD growth and chemical modification of 2D materials, Chemical Society Reviews, 48 (2019) 4639-4654. http://doi.org/10.1039/C9CS00348G.

[10] Wang Jiangyan, Cui Yi, Wang Dan. Design of hollow nanostructures for energy storage, conversion and production, Advanced Materials, 31 (2019) 1801993. https://doi.org/10.1002/adma.201801993.

[11] Zhou Liang, Zhuang Zechao, Zhao Huihui, Lin Mengting, Zhao Dongyuan, Mai Liqiang. Intricate Hollow structures: Controlled synthesis and applications in energy storage and conversion, Advanced Materials, 29 (2017) 1602914. https://doi.org/10.1002/adma.201602914.

[12] Cheng Hui, G Joseph, Shapter, Li Yongying, Gao Guo. Recent progress of advanced anode materials of lithium-ion batteries, Journal of Energy Chemistry, 57 (2021) 451-468. https://doi.org/10.1016/j.jechem.2020.08.056.

[13] Liu Yanan, Wei Zengyan, Zhong Bo, Wang Huatao, Xia Long, Zhang Tao, Duan Xiaoming, Jia Dechang, Zhou Yu, Huang, O- Xiaoxiao. N-Coordinated single Mn atoms accelerating polysulfides transformation in lithium-sulfur batteries, Energy Storage Materials, 35 (2021) 12-18. https://doi.org/10.1016/j.ensm.2020.11.011.

[14] Wang Yinglin, Ma Chao, Wang Chen, Cheng Pengfei, Xu Luping, Lv Li, Zhang Hua. Design of SnO_2@Air@TiO_2 hierarchical urchin-like double-hollow nanospheres for high performance dye-sensitized solar cells, Solar Energy, 189 (2019) 412-420. https://doi.org/10.1016/j.solener.2019.07.082.

[15] F. Aldosari Obaid, Hussain Ijaz. Unlocking the potential of TiO_2-based photocatalysts for green hydrogen energy through water-splitting: Recent advances, future perspectives and techno feasibility assessment, International Journal of Hydrogen Energy, 59 (2024) 958-981. https://doi.org/10.1016/j.ijhydene.2024.01.306.

[16] Wang Jiaming, Huang Ying, Du Xianping, Zhang Shuai, Zong Meng. Hollow 1D carbon tube core anchored in Co_3O_4@SnS_2 multiple shells for constructing binder-free electrodes of flexible supercapacitors, Chemical Engineering Journal, 464 (2023) 142741. https://doi.org/10.1016/j.cej.2023.142741.

[17] Liu Nian, Lu Zhenda, Zhao Jie, T Matthew, McDowell, Lee Hyun-Wook, Zhao Wenting, Cui Yi. A pomegranate-inspired nanoscale design for large-volume-change lithium battery anodes, Nature Nanotechnology, 9 (2014) 187-192. http://doi.org/10.1038/nnano.2014.6.

[18] Zhao Jian, Li Zhenyu, Wang Jinfeng, Li Quanxiang, Wang Xungai. Capsular polypyrrole hollow nanofibers: an efficient recyclable adsorbent for hexavalent chromium removal, Journal of Materials Chemistry A, 3 (2015) 15124-15132. http://doi.org/10.1039/C5TA02525G.

[19] Liu Jun, Liu Wei, Ji Shaomin, Wan Yanling, Gu Mingzhe, Yin Huaqi, Zhou Yichun. Iron Fluoride Hollow porous microspheres: Facile solution-phase synthesis and their application for Li-ion battery cathodes, Chemistry - A European Journal, 20 (2014) 5815-5820. https://doi.org/10.1002/chem.201304713.

[20] Xu Xiaobin, Nosheen Farhat, Wang Xun. Ni-decorated molybdenum carbide hollow structure derived from carbon-coated metal-organic framework for electrocatalytic hydrogen evolution reaction, Chemistry of Materials, 28 (2016) 6313-6320. http://doi.org/10.1021/acs.chemmater.6b02586.

[21] Li Zhao, Song Ming, Zhu Wenyou, Zhuang Wenchang, Du Xihua, Tian Lin. MOF-derived hollow heterostructures for advanced electrocatalysis, Coordination Chemistry Reviews, 439 (2021) 213946. https://doi.org/10.1016/j.ccr.2021.213946.

[22] Zhang Xu, Lu Wang, Tian Yuhan, Yang Shixuan, Zhang Qiang, Lei Da, Zhao Yingyuan. Nanosheet-assembled NiCo-LDH hollow spheres as high-performance electrodes for supercapacitors, Journal of Colloid and Interface Science, 606 (2022) 1120-1127. https://doi.org/10.1016/j.jcis.2021.08.094.

[23] Zhang Erhuan, Zhu Qianhong, Huang Junheng, Liu Jia, Tan Guoqiang, Sun Chengjun, Li Tao, Liu Shan, Li Yuemei, Wang Hongzhi, Wan Xiaodong, Wen Zhenhai, Fan Fengtao, Zhang Jiatao, Ariga Katsuhiko. Visually resolving the direct Z-scheme heterojunction in CdS@$ZnIn_2S_4$ hollow cubes for photocatalytic evolution of H_2 and H_2O_2 from pure water, Applied Catalysis B: Environmental, 293 (2021) 120213. https://doi.org/10.1016/j.apcatb.2021.120213.

[24] Wei Chenhao, He Mukun, Li Maoqing, Ma Xiao, Dang Wenlong, Liu Panbo, Gu Junwei. Hollow Co/NC@MnO_2 polyhedrons with enhanced synergistic effect for high-efficiency microwave absorption, Materials Today Physics, 36 (2023) 101142. https://doi.org/10.1016/j.mtphys.2023.101142.

[25] Zhao Yongpeng, Zuo Xueqing, Guo Yuan, Huang Hui, Zhang Hao, Wang Ting, Wen Ningxuan, Chen Huan, Cong Tianze, Muhammad Javid, Yang Xuan, Wang Xinnan, Fan Zeng, Pan Lujun. Structural engineering of hierarchical aerogels comprised of multi-dimensional gradient carbon nanoarchitectures for highly efficient microwave absorption, Nano-Micro Letters, 13 (2021) 144. http://doi.org/10.1007/s40820-021-00667-7.

[26] Luo Li, Huang Rui, Hu Wei, Yu Zhaoshi, Tang Zhixin, Chen Leqi, Zhang Yunhuai, Zhang Dan, Xiao Peng. Metal-organic framework-derived hollow $CoMn_2O_4$ nanocube catalysts for deep toluene oxidation, ACS Applied Nano Materials, 5 (2022) 8232-8242. http://doi.org/10.1021/acsanm.2c01329.

[27] Sun Bojing, Zhou Wei, Li Haoze, Ren Liping, Qiao Panzhe, Xiao Fang, Wang Lei, Jiang Baojiang, Fu Honggang. Magnetic Fe_2O_3/mesoporous black TiO_2 hollow sphere heterojunctions with wide-spectrum response and magnetic separation, Applied Catalysis B: Environmental, 221 (2018) 235-242. https://doi.org/10.1016/j.apcatb.2017.09.023.

[28] Fu Yuanlin, Li Yunlong, Fan Fuqiang, Chen Bingbing, Hou

Xiaojiao, Li Yuhang, Li Hui, Fu Yu, Qi Wei. Atomic-level dispersed Cu in NiFe-LDH hollow nanocages for highly efficient electrochemical nitrate reduction reaction, ACS Catalysis, 15 (2025) 6918-6928. http://doi.org/10.1021/acscatal.4c07320.

[29] Guan Xiaohui, Zhang Jiqing, Zhu Enze, Li Ruotong, Yang Liu, Liu Bao, Zhang Haifeng, Yin Penggang, Wang Guangsheng. Electron distribution regulation of nanoparticle assembled hollow structured Fe_3O_4@$ZnFe_2O_4$@NC/$Mo_2TiC_2T_x$ for high-performance aqueous zinc-ion batteries, Advanced Functional Materials, 35 (2025) 2418960. https://doi.org/10.1002/adfm.202418960.

[30] Chai Lulu, Wang Xian, Hu Yue, Li Xifei, Huang Shaoming, Pan Junqing, Qian Jinjie, Sun Xueliang. In-MOF-derived hierarchically hollow carbon nanostraws for advanced zinc-iodine batteries, Advanced Science, 9 (2022) 2105063. https://doi.org/10.1002/advs.202105063.

[31] Gao Yijun, Song Shanshan, He Fei, Kong Xianglong, Xiao Zhong, Cui Xianchang, Cao Linbo, Zhang Yumeng, Liu Zhiliang, Yang Piaoping. Controllable synthesis of hollow dodecahedral Si@C core-shell structures for ultrastable lithium-ion batteries, Small, 20 (2024) 2406489. https://doi.org/10.1002/smll.202406489.

[32] Wang Fengbo, Wang Lu, Wang Bin, Jing Zhongxin, Ding Dong, Yang Xiaofan, Kong Yueyue, Dou Jianmin, Mamoor Muhammad, Xu Liqiang. Cognate cobalt core-shell structure decorated nitrogen-doped hollow carbon bowls triggering advanced zinc-air battery, Advanced Functional Materials, 35 (2025) 2415326. https://doi.org/10.1002/adfm.202415326.

[33] Yang Yuan, Qiu Jianwei, Dai Linna, Hu Zhibiao, Lin Xiaohang, Hua Minghao, Si Pengchao. Zn-assisted low-temperature reconstruction of NiCo heterogeneous catalysts for lithium-oxygen batteries, Chemical Engineering Journal, 487 (2024) 150718. https://doi.org/10.1016/j.cej.2024.150718.

[34] Pi Yecan, Lin Hao, Meng Zhenyang, Qiu Ziming, Su Yichun, Hang Xinxin, Pang Huan. Self-template synthesis of PBA/MOF hollow nanocubes for aqueous battery, Chemical Engineering Journal, 499 (2024) 155618. https://doi.org/10.1016/j.cej.2024.155618.

[35] Li Haitao, Liu Jianchuan, Wang Yujie, Guo Chunsheng, Pi Yutong, Fang Qianrong, Liu Jian. Hollow covalent organic framework (COF) nanoreactors for sustainable photo/electrochemical catalysis, Coordination Chemistry Reviews, 523 (2025) 216240. https://doi.org/10.1016/j.ccr.2024.216240.

[36] Xiao Yawei, Li Haoyu, Yao Bo, Xiao Kai, Wang Yude. Hollow g-C_3N_4@Ag_3PO_4core-shell nanoreactor loaded with Au nanoparticles: Boosting photothermal catalysis in confined space, Small, 20 (2024) 2308032. https://doi.org/10.1002/smll.202308032.

[37] Tian Zhidong, Liang Yiqi, Chen Kai, Gao Jiyuan, Lu Zhiwen, Hu Xiang, Ding Yichun, Wen Zhenhai. Advanced hollow cubic FeCo-N-C cathode electrocatalyst for ultrahigh-power aluminum-air battery, Small, 20 (2024) 2310694. https://doi.org/10.1002/smll.202310694.

[38] Ma Hongwei, Yu Zhisheng, Li Haocheng, Guo Daying, Zhou Zheyang, Jin Huile, Wu Lianhui, Chen Xi'an, Wang Shun. Tandem carbon hollow spheres with tailored inner structure as sulfur immobilization for superior lithium-sulfur batteries, Advanced Functional Materials, 34 (2024) 2310301. https://doi.org/10.1002/adfm.202310301.

[39] Tian Yun, Wei Zhengyu, Li Fan, Li Songjie, Shao Lixiang, He Mengyuan, Sun Panfei, Li Yuanyuan. Enhanced multiple anchoring and catalytic conversion of polysulfides by SnO_2-decorated MoS_2 hollow microspheres for high-performance lithium-sulfur batteries, Journal of Materials Science & Technology, 100 (2022) 216-223. https://doi.org/10.1016/j.jmst.2021.06.002.

[40] Yan Zichao, Liang Yaru, Hua Weibo, Zhang Xia-Guang, Lai Weihong, Hu Zhe, Wang Wanlin, Peng Jian, Indris Sylvio, Wang Yunxiao, Chou Shu-Lei, Liu Huakun, Dou Shi-Xue. Multiregion janus-featured cobalt phosphide-cobalt composite for highly reversible room-temperature sodium-sulfur batteries, ACS Nano, 14 (2020) 10284-10293. http://doi.org/10.1021/acsnano.0c03737.

[41] Liang Zhenyan, Yang Mingzhi, Wang Shouzhi, Chang Bin, Tu Huayao, Shao Yongliang, Zhang Baoguo, Zhao Huaping, Lei Yong, Shen Jianxing, Wu Yongzhong, Hao Xiaopeng. Hollow submicrospheres of trimetallic selenides for high-capacity lithium and sodium ion batteries, Chemical Engineering Journal, 405 (2021) 126724. https://doi.org/10.1016/j.cej.2020.126724.

[42] Xie Fangxi, Zhang Lei, Gu Qinfen, Chao Dongliang, Jaroniec Mietek, Qiao Shi-Zhang. Multi-shell hollow structured Sb_2S_3 for sodium-ion batteries with enhanced energy density, Nano Energy, 60 (2019) 591-599. https://doi.org/10.1016/j.nanoen.2019.04.008.

[43] Yang Li-Ping, Lin Xi-Jie, Zhang Xing, Zhang Wei, Cao An-Min, Wan Li-Jun. General synthetic strategy for hollow hybrid microspheres through a progressive inward crystallization process, Journal of the American Chemical Society, 138 (2016) 5916-5922. http://doi.org/10.1021/jacs.6b00773.

[44] Zheng Dandan, Cao Xu-Ning, Wang Xinchen. Precise Formation of a Hollow Carbon Nitride Structure with a Janus Surface To Promote Water Splitting by Photoredox Catalysis, Angewandte Chemie International Edition, 55 (2016) 11512-11516. https://doi.org/10.1002/anie.201606102.

[45] Wang Yawen, Yu Le, Lou Xiong Wen. Formation of triple-shelled molybdenum-polydopamine hollow spheres and their conversion into MoO_2/carbon composite hollow spheres for lithium-ion batteries, Angewandte Chemie International Edition, 55 (2016) 14668-14672. https://doi.org/10.1002/anie.201608410.

[46] Ma Zhongyuan, Rui Kun, Zhang Qiao, Zhang Yao, Du Min, Li Desheng, Wang Qingqing, Huang Xiao, Zhu Jixin, Huang

Wei. Self-templated formation of uniform F-CuO hollow octahedra for lithium ion batteries, Small, 13 (2017) 1603500. https://doi.org/10.1002/smll.201603500.

[47] Dong Yue, Jia Baoquan, Fu Feiya, Zhang Heyou, Zhang Lina, Zhou Jinping. Fabrication of hollow materials by fast pyrolysis of cellulose composite fibers with heterogeneous structures, Angewandte Chemie International Edition, 55 (2016) 13504-13508. https://doi.org/10.1002/anie.201607455.

[48] Yu Le, Hu Han, Wu Hao Bin, Lou Xiong Wen. Complex hollow nanostructures: Synthesis and energy-related applications, Advanced Materials, 29 (2017) 1604563. https://doi.org/10.1002/adma.201604563.

[49] Qi Jian, Lai Xiaoyong, Wang Jiangyan, Tang Hongjie, Ren Hao, Yang Yu, Jin Quan, Zhang Lijuan, Yu Ranbo, Ma Guanghui, Su Zhiguo, Zhao Huijun, Wang Dan. Multi-shelled hollow micro-/nanostructures, Chemical Society Reviews, 44 (2015) 6749-6773. http://doi.org/10.1039/C5CS00344J.

[50] Wang Jiangyan, Tang Hongjie, Wang Huan, Yu Ranbo, Wang Dan. Multi-shelled hollow micro-/nanostructures: promising platforms for lithium-ion batteries, Materials Chemistry Frontiers, 1 (2017) 414-430. http://doi.org/10.1039/C6QM00273K.

[51] Wang Jiangyan, Tang Hongjie, Ren Hao, Yu Ranbo, Qi Jian, Mao Dan, Zhao Huijun, Wang Dan. pH-Regulated synthesis of multi-shelled manganese oxide hollow microspheres as supercapacitor electrodes using carbonaceous microspheres as templates, Advanced Science, 1 (2014) 1400011. https://doi.org/10.1002/advs.201400011.

[52] Guo Yuchen, Sun Jiaming, Tang Yuan, Jia Xiaofang, Nie Yu, Geng Zikang, Wang Chunyang, Zhang Junying, Tan Xin, Zhong Dichang, Ye Jinhua, Yu Tao. Efficient interfacial electron transfer induced by hollow-structured $ZnIn_2S_4$ for extending hot electron lifetimes, Energy & Environmental Science, 16 (2023) 3462-3473. http://doi.org/10.1039/D3EE01522J.

[53] Zhang Dingyue, Huang Gang, Zhang Hao, Zhang Ziqiang, Liu Yong, Gao Fan, Shang Zhoutai, Gao Caiqin, Zhou Yuhan, Fu Shihui, Wei Jingjiang, Terrones Mauricio, Wang Yanqing. Soft template-induced self-assembly strategy for sustainable production of porous carbon spheres as anode towards advanced sodium-ion batteries, Chemical Engineering Journal, 495 (2024) 153646. https://doi.org/10.1016/j.cej.2024.153646.

[54] Gao Hui, Zhang Xixi, Sun Gang, Li Chuanlin, Xu Xijin, Zhao Xian. Constructing hollowly bimetallic selenides as cathode for aqueous zinc battery with outstanding rate performance, Chemical Engineering Journal, 455 (2023) 140680. https://doi.org/10.1016/j.cej.2022.140680.

[55] Zhao Hao, Liu Guanhua, Liu Yunting, Zhou Liya, Ma Li, He Ying, Zheng Xiaobing, Gao Jing, Jiang Yanjun. Preparation of hollow spherical covalent organic frameworks via Oswald ripening under ambient conditions for immobilizing enzymes with improved catalytic performance, Nano Research, 16 (2023) 281-289. http://doi.org/10.1007/s12274-022-4769-5.

[56] Xu Chunyang, Li Qinghao, Shen Junling, Yuan Ze, Ning Jiqiang, Zhong Yijun, Zhang Ziyang, Hu Yong. A facile sequential ion exchange strategy to synthesize $CoSe_2/FeSe_2$ double-shelled hollow nanocuboids for the highly active and stable oxygen evolution reaction, Nanoscale, 11 (2019) 10738-10745. http://doi.org/10.1039/C9NR02599E.

[57] Zhu Youcai, Li Caiting, Liang Caixia, Li Shanhong, Liu Xuan, Du Xueyu, Yang Kuang, Zhao Jungang, Yu Qi, Zhai Yunbo, Ma Ying. Regulating CeO_2 morphologies on the catalytic oxidation of toluene at lower temperature: A study of the structure-activity relationship, Journal of Catalysis, 418 (2023) 151-162. https://doi.org/10.1016/j.jcat.2023.01.012.

[58] Caruso Frank, A Rachel, Caruso, Möhwald Helmuth. Nanoengineering of inorganic and hybrid hollow spheres by colloidal templating, Science, 282 (1998) 1111-1114. http://doi.org/10.1126/science.282.5391.1111.

[59] Li Yuzhang, Yan Kai, Lee Hyun-Wook, Lu Zhenda, Liu Nian, Cui Yi. Erratum: Growth of conformal graphene cages on micrometre-sized silicon particles as stable battery anodes, Nature Energy, 1 (2016) 16017. http://doi.org/10.1038/nenergy.2016.17.

[60] Wu Hui, Zheng Guangyuan, Liu Nian, J Thomas, Carney, Yang Yuan, Cui Yi. Engineering empty space between Si nanoparticles for lithium-ion battery anodes, Nano Letters, 12 (2012) 904-909. http://doi.org/10.1021/nl203967r.

[61] Zhao Meng-Qiang, Xie Xiuqiang, E. Ren Chang, Makaryan Taron, Anasori Babak, Wang Guoxiu, Gogotsi Yury. Hollow MXene spheres and 3D macroporous MXene frameworks for Na-ion storage, Advanced Materials, 29 (2017) 1702410. https://doi.org/10.1002/adma.201702410.

[62] Hye Hwang Sun, Yun Juyoung, Jang Jyongsik. Multi-shell porous TiO_2 hollow nanoparticles for enhanced light harvesting in dye-sensitized solar cells, Advanced Functional Materials, 24 (2014) 7619-7626. https://doi.org/10.1002/adfm.201401915.

[63] Tong Zhenwei, Yang Dong, Li Zhen, Nan Yanhu, Ding Fei, Shen Yichun, Jiang Zhongyi. Thylakoid-inspired multishell g-C_3N_4 nanocapsules with enhanced visible-light harvesting and electron transfer properties for high-efficiency photocatalysis, ACS Nano, 11 (2017) 1103-1112. http://doi.org/10.1021/acsnano.6b08251.

[64] Ding Yin, Hu Yong, Jiang Xiqun, Zhang Leyang, Yang Changzheng. Polymer-monomer pairs as a reaction system for the synthesis of magnetic Fe_3O_4-polymer hybrid hollow nanospheres, Angewandte Chemie International Edition, 43 (2004) 6369-6372. https://doi.org/10.1002/anie.200460408.

[65] Gu Dong, Bongard Hans, Deng Yonghui, Feng Dan, Wu Zhangxiong, Fang Yin, Mao Jianjiang, Tu Bo, Schüth Ferdi, Zhao Dongyuan. An aqueous emulsion route to synthesize mesoporous carbon vesicles and their nanocomposites, Advanced Materials, 22 (2010) 833-837. https://doi.org/10.1002/adma.200902550.

[66] Kim Seong Su, Zhang Wenzhong. Thomas J. Pinnavaia, Ultrastable mesostructured silica vesicles, Science, 282 (1998) 1302-1305. http://doi.org/10.1126/science.282.5392.1302.

[67] Li Yongjun, Li Xiaofang, Li Yuliang, Liu Huibiao, Wang Shu, Gan Haiyang, Li Junbo, Wang Ning, He Xiaorong, Zhu Daoben. Controlled self-assembly behavior of an amphiphilic bisporphyrin-bipyridinium-palladium complex:From multibilayer vesicles to hollow capsules, Angewandte Chemie International Edition, 45 (2006) 3639-3643. https://doi.org/10.1002/anie.200600554.

[68] Liu Jian. Sandy Budi Hartono, Yong Gang Jin, Zhen Li, Gao Qing Lu, Shi Zhang Qiao, A facile vesicle template route to multi-shelled mesoporous silica hollow nanospheres, Journal of Materials Chemistry, 20 (2010) 4595-4601. http://doi.org/10.1039/B925201K.

[69] Wang Guang-Hui, Hilgert Jakob. Felix Herrmann Richter, Feng Wang, Hans-Josef Bongard, Bernd Spliethoff, Claudia Weidenthaler, Ferdi Schüth, Platinum-cobalt bimetallic nanoparticles in hollow carbon nanospheres for hydrogenolysis of 5-hydroxymethylfurfural, Nature Materials, 13 (2014) 293-300. http://doi.org/10.1038/nmat3872.

[70] Wu Zhengcui, Zhang Miao, Yu Kuai, Zhang Shudong, Xie Yi. Self-assembled double-shelled ferrihydrite hollow spheres with a tunable aperture, Chemistry - A European Journal, 14 (2008) 5346-5352. https://doi.org/10.1002/chem.200701945.

[71] Zhang Yang, Yu Meihua, Zhou Liang, Zhou Xufeng, Zhao Qingfei, Li Hexing, Yu Chengzhong. Organosilica multilamellar vesicles with tunable number of layers and sponge-like walls via one surfactant templating, Chemistry of Materials, 20 (2008) 6238-6243. http://doi.org/10.1021/cm8011815.

[72] Thakur Anupma. Nithin Chandran B. S, Karis Davidson, Annabelle Bedford, Hui Fang, Yooran Im, Vaishnavi Kanduri, Brian C. Wyatt, Srinivasa Kartik Nemani, Valeriia Poliukhova, Ravi Kumar, Zahra Fakhraai, Babak Anasori, Step-by-step guide for synthesis and delamination of $Ti_3C_2T_x$ MXene, Small Methods, 7 (2023) 2300030. https://doi.org/10.1002/smtd.202300030.

[73] Yu Le, Wu Hao Bin, Lou Xiong Wen David. Self-templated formation of hollow structures for electrochemical energy applications, Accounts of Chemical Research, 50 (2017) 293-301. http://doi.org/10.1021/acs.accounts.6b00480.

[74] Liang Sun, Ziyu Zhang, Han Jiang, Xiaoyan Deng. Facile synthesis of magnetic mesoporous silica spheres for efficient removal of methylene blue via catalytic persulfate activation, Separation and Purification Technology, 256 (2021) 117801. https://doi.org/10.1016/j.seppur.2020.117801.

[75] Wang Hao, Gao Qiang, Li Haitao, Wang Guanshuai, Han Bo, Xia Kaisheng, Zhou Chenggang. Hydrous titania nanosheets constructed hierarchical hollow microspheres as a highly efficient dual-use decontaminant for elimination of heavy metal ions and organic pollutants, Chemical Engineering Journal, 381 (2020) 122638. https://doi.org/10.1016/j.cej.2019.122638.

[76] Cheng Yan, Ma Yongzhen, Dang Zhener, Hu Renrui, Liu Chenjiao, Chen Mi, Gao Lei, Lin Ying, Wang Tong, Chen Guanjun, Yang Haibo. The efficient absorption of electromagnetic waves by tunable N-doped multi-cavity mesoporous carbon microspheres, Carbon, 201 (2023) 1115-1125. https://doi.org/10.1016/j.carbon.2022.10.020.

[77] Ma Hongchao, Zhao Fanyue, Li Ming, Wang Pengyuan, Fu Yinghuan, Wang Guowen, Liu Xinghui. Construction of hollow binary oxide heterostructures by Ostwald ripening for superior photoelectrochemical removal of reactive brilliant blue KNR dye, Advanced Powder Materials, 2 (2023) 100117. https://doi.org/10.1016/j.apmate.2023.100117.

[78] Chu Yanting, Guo Lingyu, Xi Baojuan, Feng Zhenyu, Wu Fangfang, Lin Yue, Liu Jincheng, Sun Di, Feng Jinkui, Qian Yitai, Xiong Shenglin. Embedding $MnO@Mn_3O_4$ nanoparticles in an N-doped-carbon framework derived from Mn-organic clusters for efficient lithium storage, Advanced Materials, 30 (2018) 1704244. https://doi.org/10.1002/adma.201704244.

[79] Guo Ruyue, Bao Yan, Kang Qiaoling, Liu Chao, Zhang Wenbo, Zhu Qian. Solvent-controlled synthesis and photocatalytic activity of hollow TiO_2 microspheres prepared by the solvothermal method, Colloids and Surfaces A: Physicochemical and Engineering Aspects, 633 (2022) 127931. https://doi.org/10.1016/j.colsurfa.2021.127931.

[80] Weng Wangsuo, Lin Jun, Du Yichen, Ge Xufang, Zhou Xiaosi, Bao Jianchun. Template-free synthesis of metal oxide hollow micro-/nanospheres via Ostwald ripening for lithium-ion batteries, Journal of Materials Chemistry A, 6 (2018) 10168-10175. http://doi.org/10.1039/C8TA03161D.

[81] Ma Tiantian, Zheng Lingli, Zhao Yingqiang, Xu Yongshan, Zhang Jun, Liu Xianghong. Highly Porous Double-shelled hollow hematite nanoparticles for gas sensing, ACS Applied Nano Materials, 2 (2019) 2347-2357. http://doi.org/10.1021/acsanm.9b00228.

[82] Han Chunhua, Liu Fang, Liu Jinshuai, Li Qi, Meng Jiashen, Shao Bowen, He Qiu, Wang Xuanpeng, Liu Ziang, Mai Liqiang. Facile template-free synthesis of uniform carbon-confined V_2O_3 hollow spheres for stable and fast lithium storage, Journal of Materials Chemistry A, 6 (2018) 6220-6224. http://doi.org/10.1039/C8TA01695J.

[83] Xu Hou-Ming, Gu Chao, Wang Gang, Nan Pengfei, Zhang Jian-Ding, Shi Lei, Han Shi-Kui, Ge Binghui, Wang Yang-Gang, Li Jun, Yu Shu-Hong. Kirkendall effect-driven reversible chemical transformation for reconfigurable nanocrystals, Journal of the American Chemical Society, 146 (2024) 30372-30379. http://doi.org/10.1021/jacs.4c10252.

[84] Chu Shasha, Yang Chao, Su Xintai. Synthesis of NiO hollow nanospheres via Kirkendall effect and their enhanced gas sensing performance, Applied Surface Science, 492 (2019) 82-88. https://doi.org/10.1016/j.apsusc.2019.06.226.

[85] Wu Guoqing, Liang Xiaoyu, Zhang Lijuan, Tang Zhiyong,

Al-Mamun Mohammad, Zhao Huijun, Su Xintai. Fabrication of highly stable metal oxide hollow nanospheres and their catalytic activity toward 4-nitrophenol reduction, ACS Applied Materials & Interfaces, 9 (2017) 18207-18214. http://doi.org/10.1021/acsami.7b03120.

[86] Luo XiaShuang, Fu CeHuang, Shen ShuiYun, Luo LiuXuan, Zhang JunLiang. Free-templated synthesis of N-doped PtCu porous hollow nanospheres for efficient ethanol oxidation and oxygen reduction reactions, Applied Catalysis B: Environmental, 330 (2023) 122602. https://doi.org/10.1016/j.apcatb.2023.122602.

[87] Ni Chenghao, Hao Chen, Tan Jizheng, Cai Xing, Ling Guoyan, Wu Qianqian, Wu Jingbo, Wang Xiaohong. Fabrication of $Co_{1.5}Ni_{1.5}S_4$ and Prussian blue analogues composites with yolk-shell heterostructures as cathode and biomass derived carbon as anode for asymmetric supercapacitors, Journal of Cleaner Production, 466 (2024) 142844. https://doi.org/10.1016/j.jclepro.2024.142844.

[88] Li Qin, Li Yanli, Zhao Jing, Zhao Shihang, Zhou Jiaojiao, Chen Chen, Tao Kai, Liu Rui, Han Lei. Ultrathin nanosheet-assembled hollow microplate $CoMoO_4$ array derived from metal-organic framework for supercapacitor with ultrahigh areal capacitance, Journal of Power Sources, 430 (2019) 51-59. https://doi.org/10.1016/j.jpowsour.2019.05.011.

[89] Yuan Guan Bu, Yu Le, Wang Xiao, Song Shuyan, Lou Xiong Wen. Formation of onion-like $NiCo_2S_4$ particles via sequential ion-exchange for hybrid supercapacitors, Advanced Materials, 29 (2017) 1605051. https://doi.org/10.1002/adma.201605051.

[90] Michelle D. Regulacio, Wang Yong, Seh Zhi Wei, Han Ming-Yong. Tailoring porosity in copper-based multinary sulfide nanostructures for energy, Biomedical, Catalytic, and Sensing Applications, ACS Applied Nano Materials, 1 (2018) 3042-3062. http://doi.org/10.1021/acsanm.8b00639.

[91] Wang Xiaojing, Feng Ji, Bai Yaocai, Zhang Qiao, Yin Yadong, Synthesis. properties, and applications of hollow micro-/nanostructures, Chemical Reviews, 116 (2016) 10983-11060. http://doi.org/10.1021/acs.chemrev.5b00731.

[92] T. Lawal Abdulazeez, review A, Biosensors. Graphene-based nano composites and their applications. Bioelectronics, 141 (2019) 111384. https://doi.org/10.1016/j.bios.2019.111384.

[93] Wang Mengyi, Yu Xing, Hou Long, Gagnoud Annie, Fautrelle Yves, Moreau Rene, Li Xi. 3D sandwich-shaped graphene-based nanocomposite intercalated with double-shelled hollow $MnCo_2O_4$ spheres as anode materials for lithium-ion batteries, Chemical Engineering Journal, 351 (2018) 930-938. https://doi.org/10.1016/j.cej.2018.06.163.

[94] Zhou Liang, Zhao Dongyuan, Lou Xiong Wen. Double-shelled $CoMn_2O_4$ hollow microcubes as high-capacity anodes for lithium-ion batteries, Advanced Materials, 24 (2012) 745-748. https://doi.org/10.1002/adma.201104407.

[95] Zhao Jianbo, Li Man, Li Junru, Wei Chengzhen, He Yuyue, Huang Yixuan, Li Qiaoling. Porous Ni-Co-Mn oxides prisms for high performance electrochemical energy storage, Applied Surface Science, 425 (2017) 1158-1167. https://doi.org/10.1016/j.apsusc.2017.07.261.

[96] Du Liyong, Wang Dongxue, Gu Kuikun, Zhang Mingzhe. Construction of PdO-decorated double-shell $ZnSnO_3$ hollow microspheres for n-propanol detection at low temperature, Inorganic Chemistry Frontiers, 8 (2021) 787-795. http://doi.org/10.1039/D0QI01292K.

[97] Tian Hao, Tian Huajun, Yang Wu, Zhang Fan, Yang Wang, Zhang Qiaobao, Wang Yong, Liu, S. Jian, P Ravi, Silva, Liu Hao, Wang Guoxiu. Stable hollow-structured silicon suboxide-based anodes toward high-performance lithium-ion batteries, Advanced Functional Materials, 31 (2021) 2101796. https://doi.org/10.1002/adfm.202101796.

[98] Wang Deli, He Huan, Han Lili, Lin Ruoqian, Wang Jie, Wu Zexing, Liu Hongfang, L. Xin Huolin. Three-dimensional hollow-structured binary oxide particles as an advanced anode material for high-rate and long cycle life lithium-ion batteries, Nano Energy, 20 (2016) 212-220. https://doi.org/10.1016/j.nanoen.2015.12.019.

[99] Shi Zixu, Liu Yue, Zhang Yuchen, Sun Jun, Zheng Jingxing, Wei Chengzhen, Du Weimin, Liu Lin, Cheng Cheng. Designed synthesis of yolk-shelled $NiCo_2O_4$/$MnCo_2O_4$ hollow sphere with boosted performance for supercapacitors, Applied Surface Science, 611 (2023) 155758. https://doi.org/10.1016/j.apsusc.2022.155758.

[100] Wu Guodong, Li Pinjiang, Zhu Congxu, Lei Yan, Zhao Hongxiao, Li Tingting, Yue Hongwei, Dou Baoping, Gao Yuanhao, Yang Xiaogang. Amorphous titanium oxide passivated lithium titanium phosphate electrode for high stable aqueous lithium ion batteries with oxygen tolerance, Electrochimica Acta, 246 (2017) 720-729. https://doi.org/10.1016/j.electacta.2017.06.093.

[101] Li Zhao, Huang Feng, Song Ming, He Changchun, Zhuang Wenchang, Tian Lin. Advances in CoP electrocatalysts for water splitting, Materials Today Energy, 20 (2021) 100698. https://doi.org/10.1016/j.mtener.2021.100698.

[102] Khan F. M. Nizam Uddin, G Mohammad, Rasul, Sayem A. S. M.. Nirmal K. Mandal, Design and optimization of lithium-ion battery as an efficient energy storage device for electric vehicles: A comprehensive review, Journal of Energy Storage, 71 (2023) 108033. https://doi.org/10.1016/j.est.2023.108033.

[103] Liu Tao, Zhang Liuyang, Cheng Bei, Yu Jiaguo. Hollow carbon spheres and their hybrid nanomaterials in electrochemical energy storage, Advanced Energy Materials, 9 (2019) 1803900. https://doi.org/10.1002/aenm.201803900.

[104] Villevieille Claire. The numerous materials challenges related to post-Li-ion batteries, ACS Materials Letters, 7 (2025) 1057-1059. http://doi.org/10.1021/acsmaterialslett.5c00285.

[105] Fang Shan, Bresser Dominic, Passerini Stefano. Transition metal oxide anodes for electrochemical energy storage in lithium- and sodium-ion batteries, Advanced Energy Materials, 10 (2020) 1902485. https://doi.org/10.1002/aenm.201902485.

[106] Wu Lijun, Guo Shoujie, Pu Xiangjun, Yue Hongwei, Li Hao, Li Pinjiang, Li Wei, Cai Kun, Ding Wenjie, Li Longfei, Zhang Yange, Fa Wenjun, Yang Changchun, Zheng Zhi, He Weiwei, Cao Yuliang. $Na_{0.91}MnO_2$ with an extended layer structure and excellent pseudocapacitive behavior as a cathode material for sodium-ion batteries, ACS Applied Energy Materials, 5 (2022) 4505-4512. http://doi.org/10.1021/acsaem.1c04102.

[107] Zhu Yaqiong, Yang Xin, Xu Lekai, Jia Guanwei, Du Jiang. Hollow microscale and nanoscale structures as anode materials for lithium-ion batteries, Chemistry of Materials, 34 (2022) 9803-9822. http://doi.org/10.1021/acs.chemmater.2c02870.

[108] Poizot P., Laruelle S., Grugeon S., Dupont L., Tarascon J. M.. Nano-sized transition-metal oxides as negative-electrode materials for lithium-ion batteries, Nature, 407 (2000) 496-499. http://doi.org/10.1038/35035045.

[109] Tabassum Hassina, Zou Ruqiang, Mahmood Asif, Liang Zibin, Wang Qingfei, Zhang Hao, Gao Song, Qu Chong, Guo Wenhan, Guo Shaojun. A universal strategy for hollow metal oxide nanoparticles encapsulated into B/N Co-doped graphitic nanotubes as high-performance lithium-ion battery anodes, Advanced Materials, 30 (2018) 1705441. https://doi.org/10.1002/adma.201705441.

[110] Huang Yi, Fang Yongjin, Lu Xue Feng, Luan Deyan, Lou Xiong Wen. Co_3O_4 hollow nanoparticles embedded in mesoporous walls of carbon nanoboxes for efficient lithium storage, Angewandte Chemie International Edition, 59 (2020) 19914-19918. https://doi.org/10.1002/anie.202008987.

[111] Kang Ying, Zhang Yu-Hang, Shi Qi, Shi Hongwei, Xue Dongfeng, Shi Fa-Nian. Highly efficient Co_3O_4/CeO_2 heterostructure as anode for lithium-ion batteries, Journal of Colloid and Interface Science, 585 (2021) 705-715. https://doi.org/10.1016/j.jcis.2020.10.050.

[112] Su Xin, Wu Qingliu, Li Juchuan, Xiao Xingcheng, Lott Amber, Lu Wenquan, W Brian, Sheldon, Wu Ji. Silicon-based nanomaterials for lithium-ion batteries: A review, Advanced Energy Materials, 4 (2014) 1300882. https://doi.org/10.1002/aenm.201300882.

[113] Li Hao, Chen Zidong, Kang Zhirong, Liu Wei, Chen Yungui. High-density crack-resistant Si-C microparticles for lithium ion batteries, Energy Storage Materials, 56 (2023) 40-49. https://doi.org/10.1016/j.ensm.2022.12.045.

[114] Wei Yixin, Liu Changqu, Cai Meng, Hou Ruohan, Li Kaizhen, Yuan Jichao, Zhang Pengpeng, Shao Guosheng, Zhang Peng, n/a Small. (Electrospinning meets heterostructures in lithium-sulfur batteries, 2025) 2411838. https://doi.org/10.1002/smll.202411838.

[115] Shao Qinjun, Zhu Shengdong, Chen Jian. A review on lithium-sulfur batteries: Challenge, development, and perspective, Nano Research, 16 (2023) 8097-8138. http://doi.org/10.1007/s12274-022-5227-0.

[116] Luo Zhenya, Wu Yaqin, Xu Xupeng, Ju Wenqi, Lei Weixin, Wu Dazhuan, Pan Junan, Ouyang Xiaoping. Surface-coated AlF_3 nanolayers enable polysulfide confinement within biomass-derived nitrogen-doped hierarchical porous carbon microspheres for improved lithium-sulfur batteries, Journal of Colloid and Interface Science, 660 (2024) 657-668. https://doi.org/10.1016/j.jcis.2024.01.123.

[117] Ji Xiulei, Lee Kyu Tae, F Linda, Nazar. A highly ordered nanostructured carbon-sulphur cathode for lithium-sulphur batteries, Nature Materials, 8 (2009) 500-506. http://doi.org/10.1038/nmat2460.

[118] Saroha Rakesh, Ka Hye Seon, Dae Park Gi, Cho Chungyeon, Kang Dong-Won, Cho Jung Sang. Long-term stability of lithium-sulfur batteries via synergistic integration of nitrogen-doped graphitic carbon-coated cobalt selenide nanocrystals within porous three-dimensional graphene-carbon nanotube microspheres, Journal of Power Sources, 592 (2024) 233893. https://doi.org/10.1016/j.jpowsour.2023.233893.

[119] Li Zhenwen, Li Peng, Huang Zheng, Wang Dong, Ma Dongshen, Zheng Liyu, Lu Shaojie, Yue Qin. A novel mesoporous carbon pocket with single atom Cr sites for high performance Lithium-Sulfur battery, Chemical Engineering Journal, 496 (2024) 153642. https://doi.org/10.1016/j.cej.2024.153642.

[120] Wu Guozhi, Yang Jie, Li Shanqing, Zhu Ziwen, Sheng Tian, Joo Sang Woo, Huang Jiarui. Molybdenum carbide nanoparticles encapsulated in N-doped carbon nanotubes as a sulfur host for advanced Li-S battery, Electrochimica Acta, 468 (2023) 143157. https://doi.org/10.1016/j.electacta.2023.143157.

[121] Du Zhiming, Lei Zhiping, Yan Honglei, Wang Dongdong, Wang Jiancheng, Yan Jingchong, Li Zhan-Ku, Shui Hengfu, Ren Shibiao, Wang Zhicai, Kong Ying. HNO_3 pre-oxidation-tuned microstructures of porous carbon derived from high-sulfur coal for enhancing capture and catalytic conversion of polysulfides, Fuel, 326 (2022) 125066. https://doi.org/10.1016/j.fuel.2022.125066.

[122] Yu Jian, Xiao Jiewen, Li Anran, Yang Zhao, Zeng Liang, Zhang Qianfan, Zhu Yujie, Guo Lin. Enhanced multiple anchoring and catalytic conversion of polysulfides by amorphous MoS_3 nanoboxes for high-performance Li-S batteries, Angewandte Chemie International Edition, 59 (2020) 13071-13078. https://doi.org/10.1002/anie.202004914.

[123] Pang Quan, Liang Xiao, Yuen Kwok Chun, Kulisch Joern, F Linda, Nazar. A comprehensive approach toward stable lithium-sulfur batteries with high volumetric energy density, Advanced Energy Materials, 7 (2017) 1601630. https://doi.org/10.1002/aenm.201601630.

[124] Hou Yang, Wen Zhenhai, Cui Shumao, Feng Xinliang, Chen Junhong. Strongly coupled ternary hybrid aerogels of N-deficient porous graphitic-C_3N_4 nanosheets/N-doped graphene/NiFe-layered double hydroxide for solar-driven photoelectrochemical water oxidation, Nano Letters, 16 (2016) 2268-2277. http://doi.org/10.1021/acs.nanolett.

5b04496.

[125] Zhang Juan, Li Jin-Yi, Wang Wen-Peng, Zhang Xing-Hao, Tan Xing-Hua, Chu Wei-Guo, Guo Yu-Guo. Microemulsion assisted assembly of 3D porous S/graphene@g-C_3N_4 hybrid sponge as free-standing cathodes for high energy density Li-S batteries, Advanced Energy Materials, 8 (2018) 1702839. https://doi.org/10.1002/aenm.201702839.

[126] Ma Lianbo, Zhang Wenjun, Wang Lei, Hu Yi, Zhu Guoyin, Wang Yanrong, Chen Renpeng, Chen Tao, Tie Zuoxiu, Liu Jie, Jin Zhong. Strong capillarity, chemisorption, and electrocatalytic capability of crisscrossed nanostraws enabled flexible, high-rate, and long-cycling lithium-sulfur batteries, ACS Nano, 12 (2018) 4868-4876. http://doi.org/10.1021/acsnano.8b01763.

[127] Tu Shuibin, Zhao Xinxin, Cheng Mingren, Sun Pengfei, He Yongwu, Xu Yunhua. Uniform mesoporous MnO_2 nanospheres as a surface chemical adsorption and physical confinement polysulfide mediator for lithium-sulfur batteries, ACS Applied Materials & Interfaces, 11 (2019) 10624-10630. http://doi.org/10.1021/acsami.8b20044.

[128] Zhang Yan, Wang Faming, Liu Chaoqun, Wang Zhenzhen, Kang LiHua, Huang Yanyan, Dong Kai, Ren Jinsong, Qu Xiaogang. Nanozyme decorated metal-organic frameworks for enhanced photodynamic therapy, ACS Nano, 12 (2018) 651-661. http://doi.org/10.1021/acsnano.7b07746.

[129] Wu Jingyi, Li Xiongwei, Zeng Hongxia, Xue Yang, Chen Fangyan, Xue Zhigang, Ye Yunsheng, Xie Xiaolin. Fast electrochemical kinetics and strong polysulfide adsorption by a highly oriented MoS_2 nanosheet@N-doped carbon interlayer for lithium-sulfur batteries, Journal of Materials Chemistry A, 7 (2019) 7897-7906. http://doi.org/10.1039/C9TA00458K.

[130] Yue Zhang Chao, Zhang Chaoqi, Pan Jiang Long, Sun Guo Wen, Shi Zude, Li Canhuang, Chang Xingqi, Sun Geng Zhi, Yuan Zhou Jin, Cabot Andreu. Surface strain-enhanced MoS_2 as a high-performance cathode catalyst for lithium-sulfur batteries, eScience, 2 (2022) 405-415. https://doi.org/10.1016/j.esci.2022.07.001.

[131] Liang Zibin, Zhao Ruo, Qiu Tianjie, Zou Ruqiang, Xu Qiang. Metal-organic framework-derived materials for electrochemical energy applications, EnergyChem, 1 (2019) 100001. https://doi.org/10.1016/j.enchem.2019.100001.

[132] Li Qing, Xu Yuxia, Zheng Shasha, Guo Xiaotian, Xue Huaiguo, Pang Huan. Recent progress in some amorphous materials for supercapacitors, Small, 14 (2018) 1800426. https://doi.org/10.1002/smll.201800426.

[133] Li Tingting, Zhu Congxu, Yang Xiaogang, Gao Yuanhao, He Weiwei, Yue Hongwei, Zhao Hongxiao. Co_3O_4 nanoneedle@electroactive nickel boride membrane core/shell arrays: A novel hybrid for enhanced capacity, Electrochimica Acta, 246 (2017) 226-233. https://doi.org/10.1016/j.electacta.2017.06.054.

[134] Li Wei, Wu Ming, Shi Peng, Li Tingting, Yue Hongwei, Dong Zhenwei, Gao Yuanhao, Lou Xiaojie. Enhanced energy storage performance of advanced hybrid supercapacitors derived from ultrafine Ni-P@Ni nanotubes with novel three-dimensional porous network synthesized via reaction temperatures regulation, Electrochimica Acta, 331 (2020) 135440. https://doi.org/10.1016/j.electacta.2019.135440.

[135] Li Wei, Chen Tianqi, Li Ao, Shi Peng, Wu Ming, Li Tingting, Yue Hongwei, Chen Yifeng, Huang Baojun, Lou Xiaojie. High energy density hybrid supercapacitors derived from novel Ni_3Se_2 nanowires *in situ* constructed on porous nickel foam, Inorganic Chemistry Frontiers, 8 (2021) 1093-1101. http://doi.org/10.1039/D0QI01204A.

[136] Zheng Jinfeng, Lian Xiao, Wu Mingzai, Zheng Fangcai, Gao Yuanhao, Niu Helin. A synergistic strategy combing amorphous Ni_3S_4 quantum dots and zeolite imidazole framework nanosheets for enhanced supercapacitor performance, Colloids and Surfaces A: Physicochemical and Engineering Aspects, 623 (2021) 126710. https://doi.org/10.1016/j.colsurfa.2021.126710.

[137] Li Wei, Huang Zhongzheng, Jia Yaduo, Cui Yunlong, Shi Peng, Li Tingting, Yue Hongwei, Wang Jinxiao, He Weiwei, Lou Xiaojie. Sulfate assisted synthesis of α-type nickel hydroxide nanowires with 3D reticulation for energy storage in hybrid supercapacitors, Materials Chemistry Frontiers, 6 (2022) 94-102. http://doi.org/10.1039/D1QM01298C.

[138] Nakhanivej Puritut, Dou Qingyun, Xiong Peixun, Seok Park Ho. Two-dimensional pseudocapacitive nanomaterials for high-energy- and high-power-oriented applications of supercapacitors, Accounts of Materials Research, 2 (2021) 86-96. http://doi.org/10.1021/accountsmr.0c00070.

[139] Min Jie, Liu Jun, Lei Ming, Wang Wenjun, Lu Yakun, Yang Linyu, Yang Qian, Liu Gang, Su Nan. Self-assembly of parallelly aligned NiO hierarchical nanostructures with ultrathin nanosheet subunits for electrochemical supercapacitor applications, ACS Applied Materials & Interfaces, 8 (2016) 780-791. http://doi.org/10.1021/acsami.5b09997.

[140] Huang Ming, Li Zhao Xiao, Li Fei, Li Zhang Li, Xin Zhang Yu. Facile synthesis of ultrathin manganese dioxide nanosheets arrays on nickel foam as advanced binder-free supercapacitor electrodes, Journal of Power Sources, 277 (2015) 36-43. https://doi.org/10.1016/j.jpowsour.2014.12.005.

[141] Li Sumin, Yang Kang, Ye Pingwei, Ma Kairui, Zhang Zhao, Huang Qiang. Three-dimensional porous carbon/Co_3O_4 composites derived from graphene/Co-MOF for high performance supercapacitor electrodes, Applied Surface Science, 503 (2020) 144090. https://doi.org/10.1016/j.apsusc.2019.144090.

[142] Liu Shude, Ni Dixing, Li Hai-Feng, Hui Kwun Nam, Ouyang Chu-Ying, Jun Seong Chan. Effect of cation substitution on the pseudocapacitive performance of spinel cobaltite MCo_2O_4 (M = Mn, Ni, Cu, and Co), Journal of Materials Chemistry A, 6 (2018) 10674-10685. http://doi.org/10.1039/C8TA00540K.

[143] Guan Cao, Liu Ximeng, Ren Weina, Li Xin, Cheng

Chuanwei, Wang John. Rational Design of Metal-organic framework derived hollow $NiCo_2O_4$ arrays for flexible supercapacitor and electrocatalysis, Advanced Energy Materials, 7 (2017) 1602391. https://doi.org/10.1002/aenm.201602391.

[144] Wang Liang, Jiao Xinyan, Liu Peng, Ouyang Yu, Xia Xifeng, Lei Wu, Hao Qingli. Self-template synthesis of yolk-shelled $NiCo_2O_4$ spheres for enhanced hybrid supercapacitors, Applied Surface Science, 427 (2018) 174-181. https://doi.org/10.1016/j.apsusc.2017.07.221.

[145] Xu Kaibing, Yang Jianmao, Hu Junqing. Synthesis of hollow $NiCo_2O_4$ nanospheres with large specific surface area for asymmetric supercapacitors, Journal of Colloid and Interface Science, 511 (2018) 456-462. https://doi.org/10.1016/j.jcis.2017.09.113.

[146] Dong Yanying, Wang Ying, Xu Yanan, Chen Chengcheng, Wang Yijing, Jiao Lifang, Yuan Huatang. Facile synthesis of hierarchical nanocage $MnCo_2O_4$ for high performance supercapacitor, Electrochimica Acta, 225 (2017) 39-46. https://doi.org/10.1016/j.electacta.2016.12.109.

[147] Du Juan, Liu Lei, Yu Yifeng, Lv Haijun, Zhang Yue, Chen Aibing. Confined pyrolysis for direct conversion of solid resin spheres into yolk-shell carbon spheres for supercapacitor, Journal of Materials Chemistry A, 7 (2019) 1038-1044. http://doi.org/10.1039/C8TA10266J.

[148] Sun Yong-Gang, Piao Jun-Yu, Hu Lin-Lin, Bin De-Shan, Lin Xi-Jie, Duan Shu-Yi, Cao An-Min, Wan Li-Jun. Controlling the reaction of nanoparticles for hollow metal oxide nanostructures, Journal of the American Chemical Society, 140 (2018) 9070-9073. http://doi.org/10.1021/jacs.8b04948.

[149] Chang Xiaoya, Zang Lei, Liu Song, Wang Mengying, Guo Huinan, Wang Caiyun, Wang Yijing. *In situ* construction of yolk-shell zinc cobaltite with uniform carbon doping for high performance asymmetric supercapacitors, Journal of Materials Chemistry A, 6 (2018) 9109-9115. http://doi.org/10.1039/C8TA01759J.

[150] Kim Ju Hyeong, Dae Park Gi, Hyun Yang Su, Hoo Hong Jeong, Kim Jin Koo, Chan Kang Yun. Uniquely structured iron hydroxide-carbon nanospheres with yolk-shell and hollow structures and their excellent lithium-ion storage performances, Applied Surface Science, 542 (2021) 148637. https://doi.org/10.1016/j.apsusc.2020.148637.

[151] Guan Huijuan, Zhang Jun, Liu Yang, Zhao Yafei, Zhang Bing. Rapid quantitative determination of hydrogen peroxide using an electrochemical sensor based on PtNi alloy/CeO_2 plates embedded in N-doped carbon nanofibers, Electrochimica Acta, 295 (2019) 997-1005. https://doi.org/10.1016/j.electacta.2018.11.126.

[152] Li Tingting, Jing Tianyun, Jia Xiaotian, Guo Shoujie, Li Wei, Yue Hongwei, Luo Zhihui. Galvanic replacement mediated 3D porous PtCu nano-frames for enhanced ethylene glycol oxidation, Chemical Communications, 55 (2019) 14526-14529. http://doi.org/10.1039/C9CC06773F.

[153] Li Tingting, Yang Shaokang, Zuo Yunpeng, Li Wei, Yue Hongwei, Kment Štěpán, Chai Yang. Hydrogen bond stabilized β-$Ni(OH)_x$-SO_4 interlaminar materials for highly active supercapacitors, Inorganic Chemistry Frontiers, 10 (2023) 1001-1010. http://doi.org/10.1039/D2QI01992B.

[154] Hou Yujiao, Han Peilin, Zhang Like, Li Hao, Xu Zhihong. pH-controlled assembling of POM-based metal-organic frameworks for use as supercapacitors and efficient oxidation catalysts for various sulfides, Inorganic Chemistry Frontiers, 10 (2023) 148-157. http://doi.org/10.1039/D2QI01922A.

[155] Li Tingting, Jing Tianyun, Rao Dewei, Mourdikoudis Stefanos, Zuo Yunpeng, Wang Mengye. Two-dimensional materials for electrocatalysis and energy storage applications, Inorganic Chemistry Frontiers, 9 (2022) 6008-6046. http://doi.org/10.1039/D2QI01911F.

[156] Li Dapeng, Zhang Peng, Duan Jiangtao, Wu Yaxin, Ding Na, Wan Zhenyu, Chen Longqi, Xu Jingli, Ge Suxiang, Ma Juntao. Simultaneous activation of $KHSO_5$ and BuOOH by iron octacarboxyphthalocyanine loaded on fly ash microspheres to boost pollutant degradation, Journal of Industrial and Engineering Chemistry, 114 (2022) 242-253. https://doi.org/10.1016/j.jiec.2022.07.014.

[157] Yuan Rongrong, Gu Yue, Ren Hao, Liu Jia, Zhu Guangshan. Porous aromatic framework as an efficient metal-free electrocatalyst for non-enzymatic H_2O_2 sensing, Chemistry - A European Journal, 23 (2017) 9467-9471. https://doi.org/10.1002/chem.201701833.

[158] Mei Wanwan, Yang Xiaogang, Li Lei, Tong Yuping, Lei Yan, Li Pinjiang, Zheng Zhi. Rational electrochemical recycling of spent $LiFePO_4$ and $LiCoO_2$ batteries to Fe_2O_3/CoPi photoanodes for water oxidation, ACS Sustainable Chemistry & Engineering, 8 (2020) 3606-3616. http://doi.org/10.1021/acssuschemeng.9b06175.

[159] Li Yuanjian, Wang Wenyu, Huang Baojun, Mao Zhifei, Wang Rui, He Beibei, Gong Yansheng, Wang Huanwen. Abundant heterointerfaces in MOF-derived hollow CoS_2-MoS_2 nanosheet array electrocatalysts for overall water splitting, Journal of Energy Chemistry, 57 (2021) 99-108. https://doi.org/10.1016/j.jechem.2020.08.064.

[160] Jing Tianyun, Zhang Ning, Zhang Chaonan, Mourdikoudis Stefanos, Sofer Zdeněk, Li Wei, Li Pinjiang, Li Tingting, Zuo Yunpeng, Rao Dewei. Improving C-N-FeO_x oxygen evolution electrocatalysts through hydroxyl-modulated local coordination environment, ACS Catalysis, 12 (2022) 7443-7452. http://doi.org/10.1021/acscatal.2c01153.

[161] Yang Xiaogang, Zheng Zhi, Hu Jundie, Qu Jiafu, Ma Dekun, Li Jingsha, Guo Chunxian, Li Chang Ming. Observation of 4th-order water oxidation kinetics by time-resolved photovoltage spectroscopy, iScience, 24 (2021) 103500. https://doi.org/10.1016/j.isci.2021.103500.

[162] Wang Cheng, Xu Hui, Shang Hongyuan, Jin Liujun, Chen Chunyan, Wang Yuan, Yuan Mengyu, Du Yukou. Ir-doped Pd nanosheet assemblies as bifunctional electrocatalysts for

advanced hydrogen evolution reaction and liquid fuel electrocatalysis, Inorganic Chemistry, 59 (2020) 3321-3329. http://doi.org/10.1021/acs.inorgchem.0c00132.

[163] Xu Hui, Shang Hongyuan, Wang Cheng, Du Yukou. Ultrafine Pt-based nanowires for advanced catalysis, Advanced Functional Materials, 30 (2020) 2000793. https://doi.org/10.1002/adfm.202000793.

[164] Zheng Shasha, Li Qing, Xue Huaiguo, Pang Huan, Xu Qiang. A highly alkaline-stable metal oxide@metal-organic framework composite for high-performance electrochemical energy storage, National Science Review, 7 (2020) 305-314. http://doi.org/10.1093/nsr/nwz137.

[165] Liu Guanyu, Sheng Yuan, W. Ager Joel, Kraft Markus, Xu Rong. Research advances towards large-scale solar hydrogen production from water, EnergyChem, 1 (2019) 100014. https://doi.org/10.1016/j.enchem.2019.100014.

[166] Osgood Hannah, V Surya, Devaguptapu, Xu Hui, Cho Jaephil, Wu Gang, metal Transition, Co, Ni Fe. Mn) oxides for oxygen reduction and evolution bifunctional catalysts in alkaline media, Nano Today, 11 (2016) 601-625. https://doi.org/10.1016/j.nantod.2016.09.001.

[167] Xu Hui, Wei Jingjing, Zhang Ke, Zhang Min, Liu Chaofan, Guo Jun, Du Yukou. Constructing bundle-like Co-Mn oxides and Co-Mn selenides for efficient overall water splitting, Journal of Materials Chemistry A, 6 (2018) 22697-22704. http://doi.org/10.1039/C8TA07449F.

[168] Du Cheng, Li Ping, Zhuang Zhihua, Fang Zhongying, He Shuijian, Feng Ligang, Chen Wei. Highly porous nanostructures: Rational fabrication and promising application in energy electrocatalysis, Coordination Chemistry Reviews, 466 (2022) 214604. https://doi.org/10.1016/j.ccr.2022.214604.

[169] Wang Cheng, Shang Hongyuan, Li Jie, Wang Yuan, Xu Hui, Wang Chuanyi, Guo Jun, Du Yukou. Ultralow Ru doping induced interface engineering in MOF derived ruthenium-cobalt oxide hollow nanobox for efficient water oxidation electrocatalysis, Chemical Engineering Journal, 420 (2021) 129805. https://doi.org/10.1016/j.cej.2021.129805.

[170] Lu Qi, Wu Han, Zheng Xuerong, Chen Yanan, L Andrey, Rogach, Han Xiaopeng, Deng Yida, Hu Wenbin. Encapsulating cobalt nanoparticles in interconnected N-doped hollow carbon nanofibers with enriched Co N C moiety for enhanced oxygen electrocatalysis in Zn-Air batteries, Advanced Science, 8 (2021) 2101438. https://doi.org/10.1002/advs.202101438.

[171] Tie Weiwei. Surjya Sarathi Bhattacharyya, Tianci Ma, Shuangyi Yuan, Minghan Chen, Weiwei He, Seung Hee Lee, Improving photoexcited carrier separation through Z-scheme $W_{18}O_{49}$/BiOBr heterostructure coupling carbon quantum dots for efficient photoelectric response and tetracycline photodegradation, Carbon, 231 (2025) 119707. https://doi.org/10.1016/j.carbon.2024.119707.

[172] Tie Weiwei, Du Zhaoyu, Yue Hongwei. Surjya Sarathi Bhattacharyya, Zhi Zheng, Weiwei He, Seung Hee Lee, Self-assembly of carbon nanotube/graphitic-like flake/BiOBr nanocomposite with 1D/2D/3D heterojunctions for enhanced photocatalytic activity, Journal of Colloid and Interface Science, 579 (2020) 862-871. https://doi.org/10.1016/j.jcis.2020.06.088.

[173] Tie Weiwei, Zheng Zhao, Xu Chao, Zheng Zhi. Surjya Sarathi Bhattacharyya, Weiwei He, Seung Hee Lee, Facile synthesis of carbon nanotubes covalently modified with ZnO nanorods for enhanced photodecomposition of dyes, Journal of Colloid and Interface Science, 537 (2019) 652-660. https://doi.org/10.1016/j.jcis.2018.11.042.

[174] Ge Suxiang, Li Dapeng, Cui Zhankui, Zhang Yakun, Zhang Sen, Zhang Tianyi, Jia Gaoyang, He Weiwei, Zheng Zhi. Regulating the relative content of O^{2-} and OH for PCPNa degradation on BiOCl plates with controllable exposed crystal faces and surface oxygen vacancies, Separation and Purification Technology, 228 (2019) 115743. https://doi.org/10.1016/j.seppur.2019.115743.

[175] Ge Suxiang, Wang Yafei, Song Panting, Zhan Guangming, Liu Chunhui, Ding Xing, Li Dapeng, Mao Chengliang, Zheng Zhi, Zhang Lizhi. Photo-switchable In(III)-to-In(I) site on oxygen vacancy-laden BiOCl surface for selective degradation of monocyclic aromatic compounds, Separation and Purification Technology, 326 (2023) 124716. https://doi.org/10.1016/j.seppur.2023.124716.

[176] Liu Manying, Yang Kangni, Li Zhenyang, Fan Erchuang, Fu Huafeng, Zhang Like, Zhang Yange, Zheng Zhi. The O/S heteroatom effects of covalent triazine frameworks for photocatalytic hydrogen evolution, Chemical Communications, 58 (2022) 92-95. http://doi.org/10.1039/D1CC05619K.

[177] Li Lei, Yang Xiaogang, Lei Yan, Yu Haili, Yang Zhongzheng, Zheng Zhi, Wang Dunwei. Ultrathin Fe-NiO nanosheets as catalytic charge reservoirs for a planar Mo-doped $BiVO_4$ photoanode, Chemical Science, 9 (2018) 8860-8870. http://doi.org/10.1039/C8SC03297A.

[178] Wang Jiaji, Li Lei, Lei Yan, Zhang Yange, Li Pinjiang, Zhu Congxu, Wang Ke, Zheng Zhi, Yang Xiaogang. Facile chemical solution transportation for direct recycling of iron oxide rust waste to hematite films, ACS Sustainable Chemistry & Engineering, 6 (2018) 12232-12240. http://doi.org/10.1021/acssuschemeng.8b02581.

[179] Ma Minzhi, Fang Yuanxing, Huang Zeai, Wu Sixin, He Weiwei, Ge Suxiang, Zheng Zhi, Zhou Ying, Fa Wenjun, Wang Xinchen. Mechanistic insights into H_2O dissociation in overall photo-/electro-catalytic CO_2 reduction, Angewandte Chemie International Edition, 64 (2025) e202425195. https://doi.org/10.1002/anie.202425195.

[180] Ma Minzhi, Huang Zeai, Li Lina, Zhang Wenda, Guo Rui, Zhang Ruiyang, Fa Wenjun, Han Chunqiu, Cao Yuehan, Yu Shan, Zhou Ying. Modulating photogenerated electron density of Pr single-atom sites by coordination environment

engineering for boosting photoreduction of CO_2 to CH_3OH, Applied Catalysis B: Environmental, 330 (2023) 122626. https://doi.org/10.1016/j.apcatb.2023.122626.

[181] Ma Minzhi, Huang Zeai, Wang Rui, Zhang Ruiyang, Yang Tian, Rao Zhiqiang, Fa Wenjun, Zhang Fengying, Cao Yuehan, Yu Shan, Zhou Ying. Targeted H_2O activation to manipulate the selective photocatalytic reduction of CO_2 to CH_3OH over carbon nitride-supported cobalt sulfide, Green Chemistry, 24 (2022) 8791-8799. http://doi.org/10.1039/D2GC03226K.

[182] Xu Yanan, Gao Zhihong, Peng Li, Liu Kang, Yang Yang, Qiu Rongxing, Yang Shuliang, Wu Chenhao, Jiang Jiaheng, Wang Yanliang, Tan Wenjun, Wang Hongtao, Li Jun. A highly efficient $Cu/ZnO_x/ZrO_2$ catalyst for selective CO_2 hydrogenation to methanol, Journal of Catalysis, 414 (2022) 236-244. https://doi.org/10.1016/j.jcat.2022.09.011.

[183] Ma Minzhi, Huang Zeai, E Dmitry, Doronkin, Fa Wenjun, Rao Zhiqiang, Zou Yanzhao, Wang Rui, Zhong Yunqian, Cao Yuehan, Zhang Ruiyang, Zhou Ying. Ultrahigh surface density of Co-N_2C single-atom-sites for boosting photocatalytic CO_2 reduction to methanol, Applied Catalysis B: Environmental, 300 (2022) 120695. https://doi.org/10.1016/j.apcatb.2021.120695.

[184] Zhu Shasha, Wang Dunwei. Photocatalysis: Basic principles, diverse forms of implementations and emerging scientific opportunities, Advanced Energy Materials, 7 (2017) 1700841. https://doi.org/10.1002/aenm.201700841.

[185] Niu Kai-Kai, Luan Tian-Xiang, Cui Jing, Liu Hui, Xing Ling-Bao, Li Pei-Zhou. Red-light-based effective photocatalysis of a photosensitive covalent organic framework triggered singlet oxygen, ACS Catalysis, 14 (2024) 2631-2641. http://doi.org/10.1021/acscatal.3c05454.

[186] Chen Ruotian, Ren Zefeng, Liang Yu, Zhang Guanhua, Dittrich Thomas, Liu Runze, Liu Yang, Zhao Yue, Pang Shan, An Hongyu, Ni Chenwei, Zhou Panwang, Han Keli, Fan Fengtao, Li Can. Spatiotemporal imaging of charge transfer in photocatalyst particles, Nature, 610 (2022) 296-301. http://doi.org/10.1038/s41586-022-05183-1.

[187] Xue Zhong-Hua, Luan Deyan, Zhang Huabin, Lou Xiong Wen. Single-atom catalysts for photocatalytic energy conversion, Joule, 6 (2022) 92-133. https://doi.org/10.1016/j.joule.2021.12.011.

[188] Dong Qian, Chen Zhiwu, Zhao Bo, Zhang Yizeng, Lu Zhenya, Wang Xin, Li Jinliang, Chen Wei. *In situ* fabrication of niobium pentoxide/graphitic carbon nitride type-II heterojunctions for enhanced photocatalytic hydrogen evolution reaction, Journal of Colloid and Interface Science, 608 (2022) 1951-1959. https://doi.org/10.1016/j.jcis.2021.10.161.

[189] Li Hexing, Bian Zhenfeng, Zhu Jian, Zhang Dieqing, Li Guisheng, Huo Yuning, Li Hui, Lu Yunfeng. Mesoporous titania spheres with tunable chamber stucture and enhanced photocatalytic activity, Journal of the American Chemical Society, 129 (2007) 8406-8407. http://doi.org/10.1021/ja072191c.

[190] Li Wei, Deng Yonghui, Wu Zhangxiong, Qian Xufang, Yang Jianping, Wang Yao, Gu Dong, Zhang Fan, Tu Bo, Zhao Dongyuan. Hydrothermal etching assisted crystallization: A facile route to functional yolk-shell titanate microspheres with ultrathin nanosheets-assembled double shells, Journal of the American Chemical Society, 133 (2011) 15830-15833. http://doi.org/10.1021/ja2055287.

[191] Jiang Longbo, Yuan Xingzhong, Pan Yang, Liang Jie, Zeng Guangming, Wu Zhibin, Wang Hou. Doping of graphitic carbon nitride for photocatalysis: A review, Applied Catalysis B: Environmental, 217 (2017) 388-406. https://doi.org/10.1016/j.apcatb.2017.06.003.

[192] Feng Yiping, Chen Guang, Zhang Yijian, Li Daguang, Ling Chen, Wang Qiaoying, Liu Guoguang. Superhigh co-adsorption of tetracycline and copper by the ultrathin g-C_3N_4 modified graphene oxide hydrogels, Journal of Hazardous Materials, 424 (2022) 127362. https://doi.org/10.1016/j.jhazmat.2021.127362.

[193] Liu Dong, Li Chunling, Zhao Congyue, Zhao Qian, Niu Tianqi, Pan Likun, Xu Pengwei, Zhang Fengquan, Wu Weidong, Ni Tianjun. Facile synthesis of three-dimensional hollow porous carbon doped polymeric carbon nitride with highly efficient photocatalytic performance, Chemical Engineering Journal, 438 (2022) 135623. https://doi.org/10.1016/j.cej.2022.135623.

[194] Zheng Qinmin, P David, Durkin, E Justin, Elenewski, Sun Yingxue, A Nathan, Banek, Hua Likun, Chen Hanning, J Michael, Wagner, Zhang Wen, Shuai Danmeng. Visible-light-responsive graphitic carbon nitride: Rational design and photocatalytic applications for water treatment, Environmental Science & Technology, 50 (2016) 12938-12948. http://doi.org/10.1021/acs.est.6b02579.

[195] Liang Qinghua, Liu Xiaojuan, Wang Jiajia, Liu Yang, Liu Zhifeng, Tang Lin, Shao Binbin, Zhang Wei, Gong Shanxi, Cheng Min, He Qingyun, Feng Chengyang. In-situ self-assembly construction of hollow tubular g-C_3N_4 isotype heterojunction for enhanced visible-light photocatalysis: Experiments and theories, Journal of Hazardous Materials, 401 (2021) 123355. https://doi.org/10.1016/j.jhazmat.2020.123355.

[196] Gao Jiqiang, Liu Chunhui, Li Zhongjuan, Liang Haotian, Ao Yuhui, Zhao Jinbo, Wang Yuchao, Wu Yuanqi, Liu Yu. Catalytic C-C cleavage/alkyne-carbonyl metathesis sequence of cyclobutanones, Organic Letters, 22 (2020) 3993-3999. http://doi.org/10.1021/acs.orglett.0c01317.

[197] Liu Chunhui, Li Shi-Jun, Han Peilin, Qu Ling-Bo, Lan Yu. How to inverse the chemoselectivity of nucleophilic addition by using a Lewis acid/Brønsted base pair catalyst: A theoretical view, Molecular Catalysis, 499 (2021) 111318. https://doi.org/10.1016/j.mcat.2020.111318.

[198] Liu Chunhui, Han Peilin, Zhang Xusheng, Qiao Yan, Xu

Zhihong, Zhang Yange, Li Dapeng, Wei Donghui, Lan Yu. NHC-catalyzed transformation reactions of imines: Electrophilic versus nucleophilic attack, The Journal of Organic Chemistry, 87 (2022) 7989-7994. http://doi.org/10.1021/acs.joc.2c00621.

[199] Liu Chunhui, Han Peilin, Li Dapeng, Qu Ling-Bo, Qiao Yan, Lan Yu, of Mechanistic study. 4 + 3]cyclization of N, N′-cyclic azomethine imines with isatoic anhydrides under Brønsted acid catalysis, Molecular Catalysis, 525 (2022) 112300. https://doi.org/10.1016/j.mcat.2022.112300.

[200] Liu Chunhui, Zhang Xusheng, Han Peilin, Hou Yujiao, Zhang Shixing, Ge Suxiang, Li Dapeng, Jiang Yubo, Li Yongyuan. Theoretical studies on the competing mechanism and origin of diastereoselectivity of NHC-catalyzed intramolecular [3 + 2] annulations of ynals, The Journal of Physical Chemistry A, 129 (2025) 2725-2733. http://doi.org/10.1021/acs.jpca.4c08775.

[201] Chen X., Zhang X., Xiao X., Wang Z., Zhao J.. Recent developments on understanding charge transfer in molecular electron donor-acceptor systems, Angewandte Chemie International Edition, 62 (2023) e202216010. http://doi.org/10.1002/anie.202216010.

[202] Chen Yuwei, Yang Lixia, Li Chao, Wu Yuqiu, Lv Xiao, Wang Hairen, Qu Jun'e. *In situ* hydrothermal oxidation of ternary FeCoNi alloy electrode for overall water splitting, Energy & Environmental Materials, 7 (2024) e12590. https://doi.org/10.1002/eem2.12590.

[203] Zhang Fei, Li Yukun, Ding Bin, Shao Guosheng, Li Neng, Zhang Peng. Electrospinning photocatalysis meet *in situ* irradiated XPS: Recent mechanisms advances and challenges, Small, 19 (2023) 2303867. https://doi.org/10.1002/smll.202303867.

[204] Krishna D. Nanda Gopala. John Philip, Review on surface-characterization applications of X-ray photoelectron spectroscopy (XPS): Recent developments and challenges, Applied Surface Science Advances, 12 (2022) 100332. https://doi.org/10.1016/j.apsadv.2022.100332.

[205] Greczynski G., Hultman L.. X-ray photoelectron spectroscopy: Towards reliable binding energy referencing, Progress in Materials Science, 107 (2020) 100591. https://doi.org/10.1016/j.pmatsci.2019.100591.

[206] Zhang Jianjun, Zhang Liuyang, Wang Wang, Yu Jiaguo. *In situ* irradiated X-ray photoelectron spectroscopy investigation on electron transfer mechanism in S-scheme photocatalyst, The Journal of Physical Chemistry Letters, 13 (2022) 8462-8469. http://doi.org/10.1021/acs.jpclett.2c02125.

[207] Li Yukun, Wang Li, Zhang Fei, Zhang Wentao, Shao Guosheng, Zhang Peng. Detecting and quantifying wavelength-dependent electrons transfer in heterostructure catalyst via *in situ* irradiation XPS, Advanced Science, 10 (2023) 2205020. https://doi.org/10.1002/advs.202205020.

[208] Zhang Pengpeng, Xue Chao, Li Yukun, Guo Shuaiwei, Zhang Xilai, Zhang Peng, Shao Guosheng. Rational regulation on charge spatial separation and directional migration in the yolk-shell structural $SiO_2/Ni_2P/rGO/Cd_{0.5}Zn_{0.5}S$ nanoreactor for efficient photocatalytic H_2 evolution, Chemical Engineering Journal, 404 (2021) 126497. https://doi.org/10.1016/j.cej.2020.126497.

[209] Li Yukun, Zhang Yongshang, Hou Ruohan, Ai Yinyin, Cai Meng, Shi Zuhao, Zhang Peng, Shao Guosheng. Revealing electron numbers-binding energy relationships in heterojunctions via in-situ irradiated XPS, Applied Catalysis B: Environment and Energy, 356 (2024) 124223. https://doi.org/10.1016/j.apcatb.2024.124223.

[210] Song Ning, Jiang Jizhou, Hong Shihuan, Wang Yun, Li Chunmei, Dong Hongjun. State-of-the-art advancements in single atom electrocatalysts originating from MOFs for electrochemical energy conversion, Chinese Journal of Catalysis, 59 (2024) 38-81. https://doi.org/10.1016/S1872-2067(23)64622-4.

[211] Wang Jiamei, Jiang Jizhou, Li Fangyi, Zou Jing, Xiang Kun, Wang Haitao, Li Youji, Li Xin. Emerging carbon-based quantum dots for sustainable photocatalysis, Green Chemistry, 25 (2023) 32-58. http://doi.org/10.1039/D2GC03160D.

[212] Osawa Masatoshi. Dynamic processes in electrochemical reactions studied by surface-enhanced infrared absorption spectroscopy (SEIRAS), Bulletin of the Chemical Society of Japan, 70 (1997) 2861-2880. http://doi.org/10.1246/bcsj.70.2861.

[213] Hartstein A., Kirtley J. R., Tsang J. C.. Enhancement of the infrared absorption from molecular monolayers with thin metal overlayers, Physical Review Letters, 45 (1980) 201-204. http://doi.org/10.1103/PhysRevLett.45.201.

[214] Osawa Masatoshi, Ataka Ken-Ichi, Yoshii Katsumasa, Nishikawa Yuji. Surface-Enhanced Infrared Spectroscopy: The origin of the absorption enhancement and band selection rule in the infrared spectra of molecules adsorbed on fine metal particles, Appl. Spectrosc. , 47 (1993) 1497-1502. http://doi.org/10.1366/0003702934067478.

[215] Krauth O., Fahsold G., Pucci A.. Asymmetric line shapes and surface enhanced infrared absorption of CO adsorbed on thin iron films on MgO(001), The Journal of Chemical Physics, 110 (1999) 3113-3117. http://doi.org/10.1063/1.477907.

[216] M. Kosower Edward, Markovich Gil, Borz Galina. Surface-enhanced infrared absorption of p-nitrobenzoic acid on planar silver halide fiber, The Journal of Physical Chemistry B, 108 (2004) 12873-12876. http://doi.org/10.1021/jp048192y.

[217] Aroca R. F., Ross D. J., Domingo C.. Surface-enhanced infrared spectroscopy, Appl Spectrosc, 58 (2004) 324a-338a. http://doi.org/10.1366/0003702042475420.

[218] Nishikawa Yuji, Fujiwara Kunihiro, Ataka Kenichi, Osawa Masatoshi. Surface-enhanced infrared external reflection spectroscopy at low reflective surfaces and its application to surface analysis of semiconductors, glasses, and polymers, Analytical Chemistry, 65 (1993) 556-562. http://doi.org/

10.1021/ac00053a011.

[219] Ataka Kenichi, Heberle Joachim. Use of surface enhanced infrared absorption spectroscopy (SEIRA) to probe the functionality of a protein monolayer, Biopolymers, 82 (2006) 415-419. http://doi.org/10.1002/bip.20501.

[220] Martin I., Goormaghtigh E., Ruysschaert J. M.. Attenuated total reflection IR spectroscopy as a tool to investigate the orientation and tertiary structure changes in fusion proteins, Biochimica et Biophysica Acta (BBA) - Biomembranes, 1614 (2003) 97-103. http://doi.org/https://doi.org/10.1016/S0005-2736(03)00167-6.

[221] Kozuch Jacek, Ataka Kenichi, Heberle Joachim. Surface-enhanced infrared absorption spectroscopy, Nature Reviews Methods Primers, 3 (2023) 70. http://doi.org/10.1038/s43586-023-00253-8.

[222] Yang Xuan, Nash Jared, Oliveira Nicholas, Yan Yushan, Xu Bingjun. Understanding the pH dependence of underpotential deposited hydrogen on platinum, Angewandte Chemie International Edition, 58 (2019) 17718-17723. https://doi.org/10.1002/anie.201909697.

[223] Yang Chang, An Lulu, Mi Zhensheng, Wang Guangzhe, Zhang Chenhao, Kong Weijie, Yang Junhao, Xiao Li, Zhuang Lin, Wang Deli. Unconventional-phase engineering of RuGa intermetallics for boosting alkaline hydrogen-electrode reactions, Journal of Materials Chemistry A, 13 (2025) 7158-7167. http://doi.org/10.1039/D4TA08846H.

[224] Zhu Shangqian, Qin Xueping, Xiao Fei, Yang Shuangli, Xu Yuan, Tan Zhuo, Li Jiadong, Yan Jiawei, Chen Qing, Chen Mingshu, Shao Minhua. The role of ruthenium in improving the kinetics of hydrogen oxidation and evolution reactions of platinum, Nature Catalysis, 4 (2021) 711-718. http://doi.org/10.1038/s41929-021-00663-5.

[225] Shen Tao, Zhang Jingjing, Chen Ke, Deng Shaofeng, Wang Deli. Recent progress of palladium-based electrocatalysts for the formic acid oxidation reaction, Energy & Fuels, 34 (2020) 9137-9153. http://doi.org/10.1021/acs.energyfuels.0c01820.

[226] Chen Aicheng, Ostrom Cassandra. Palladium-based nanomaterials: Synthesis and electrochemical applications, Chemical Reviews, 115 (2015) 11999-12044. http://doi.org/10.1021/acs.chemrev.5b00324.

[227] Wang Wenlan, Kang Jinwei, Song Linna, Xu Shiqin, Zhang Qixian, Yuan Junhua. Porous octahedral PdRuCu nanocages for highly efficient electrochemical oxidation of formic acid, Journal of Alloys and Compounds, 1038 (2025) 182752. https://doi.org/10.1016/j.jallcom.2025.182752.

[228] Liu Juanjuan, Zou Shihui, Xiao Liping, Fan Jie. Well-dispersed bimetallic nanoparticles confined in mesoporous metal oxides and their optimized catalytic activity for nitrobenzene hydrogenation, Catalysis Science & Technology, 4 (2014) 441-446. http://doi.org/10.1039/C3CY00689A.

[229] Sun Lizhi, Lv Hao, Feng Ji, Guselnikova Olga, Wang Yanzhi, Yamauchi Yusuke, Liu Ben. Noble-metal-based hollow mesoporous nanoparticles: Synthesis strategies and applications, advanced materials, 34 (2022) 2201954. https://doi.org/10.1002/adma.202201954.

[230] Zhang Lili, Lei Yuanting, Wang Xiaochen, Lv Enyu, Li Jinzhan, Zhang Ning, Wang Dan, Zhao Yafei, Shang Huishan, Zhang Bing. Synergistic long-range interaction of Co-Cu dual-atom sites on hollow CeO_2 nanostructures for bifunctional oxygen electrocatalysis, Advanced Functional Materials, n/a (2025) e11730. https://doi.org/10.1002/adfm.202511730.

[231] Feng Chen, Zhang Zhirong, Wang Dongdi, Kong Yuan, Wei Jie, Wang Ruyang, Ma Peiyu, Li Hongliang, Geng Zhigang, Zuo Ming, Bao Jun, Zhou Shiming, Zeng Jie. Tuning the electronic and steric interaction at the atomic interface for enhanced oxygen evolution, Journal of the American Chemical Society, 144 (2022) 9271-9279. http://doi.org/10.1021/jacs.2c00533.

[232] Hu Yang, Zheng Yao, Jin Jing, Wang Yantao, Peng Yong, Yin Jie, Shen Wei, Hou Yichao, Zhu Liu, An Li, Lu Min, Xi Pinxian, Yan Chun-Hua. Understanding the sulphur-oxygen exchange process of metal sulphides prior to oxygen evolution reaction, Nature Communications, 14 (2023) 1949. http://doi.org/10.1038/s41467-023-37751-y.

[233] Zhang Haijuan, Xu Hengyue, Chen Jie, Guan Daqin, Hu Zhiwei, Xu Xiaomin, Lin Zezhou, Sun Hainan, Sun Xiao, Tang Jiayi, Pao Chih-Wen, Chen Chien-Te, Zhou Wei, Wang Chunchang, Guo Youmin, Shao Zongping. Self-optimized interfacial Co-O-Ru motifs of hollow nanotube composites Trigger Interfacial Lattice Oxygen Participation and Diffusion, ACS Nano, 19 (2025) 25917-25929. http://doi.org/10.1021/acsnano.5c05834.

[234] Li N., Yang Y., Shi Z., Lan Z., Arramel A., Zhang P., Ong W. J., Jiang J., Lu J.. Shedding light on the energy applications of emerging 2D hybrid organic-inorganic halide perovskites, iScience, 25 (2022) 103753. http://doi.org/10.1016/j.isci.2022.103753.

[235] Najafi Leyla, Bellani Sebastiano, Oropesa-Nuñez Reinier, Prato Mirko, Martín-García Beatriz, Brescia Rosaria, Bonaccorso Francesco, nanotube-supported Carbon. $MoSe_2$ holey flake: Mo_2C ball hybrids for bifunctional pH-universal water splitting, ACS Nano, 13 (2019) 3162-3176. http://doi.org/10.1021/acsnano.8b08670.

[236] Subagyo Riki, Yudhowijoyo Azis. Novia Amalia Sholeha, Sutrisno Salomo Hutagalung, Didik Prasetyoko, Muhammad Danang Birowosuto, Arramel Arramel, Jizhou Jiang, Yuly Kusumawati, Recent advances of modification effect in Co_3O_4-based catalyst towards highly efficient photocatalysis, Journal of Colloid and Interface Science, 650 (2023) 1550-1590. https://doi.org/10.1016/j.jcis.2023.07.117.

[237] Wang Ying, Zhang Zizhong, Zhang Lina, Luo Zhongbin, Shen Jinni, Lin Huaxiang, Long Jinlin, C. S. Wu Jeffrey, Fu Xianzhi, Wang Xuxu, Li Can. Visible-light driven overall conversion of CO_2 and H_2O to CH_4 and O_2 on 3D-SiC@2D-MoS_2 heterostructure, Journal of the American Chemical

Society, 140 (2018) 14595-14598. http://doi.org/10.1021/jacs.8b09344.

[238] Zou Jing, Wu Jing, Wang Yizhou, Deng Fengxia, Jiang Jizhou, Zhang Yizhou, Liu Song, Li Neng, Zhang Han, Yu Jiaguo, Zhai Tianyou, N Husam, Alshareef. Additive-mediated intercalation and surface modification of MXenes, Chemical Society Reviews, 51 (2022) 2972-2990. http://doi.org/10.1039/D0CS01487G.

[239] Li Fangyi, Anjarsari Yulianti, Wang Jiamei, Azzahiidah Rifda, Jiang Jizhou, Zou Jing, Xiang Kun, Ma Huijuan, Arramel. Modulation of the lattice structure of 2D carbon-based materials for improving photo/electric properties, Carbon Letters, 33 (2023) 1321-1331. http://doi.org/10.1007/s42823-022-00380-4.

[240] Bai Saishuai, Yang Meiqing, Jiang Jizhou, He Xiaomiao, Zou Jing, Xiong Zhiguo, Liao Guodong, Liu Song. Recent advances of MXenes as electrocatalysts for hydrogen evolution reaction, npj 2D Materials and Applications, 5 (2021) 78. http://doi.org/10.1038/s41699-021-00259-4.

[241] Peng Pan, Zhong Yifan, Zhou Cong, Tao Yongsheng, Li Dandan, Lu Qingquan. Unlocking the nucleophilicity of strong alkyl C-H bonds via Cu/Cr catalysis, ACS Central Science, 9 (2023) 756-762. http://doi.org/10.1021/acscentsci.2c01389.

[242] Wang Xue, Jin Xueyang, Xie Zhiyu, Zhang Hongyang, Liu Tiantian, Zheng Hongbo, Luan Xiaoyi, Sun Yan, Fang Wenjie, Chang Wenqiang, Lou Hongxiang. Benzamidine conjugation converts expelled potential active agents into antifungals against drug-resistant fungi, Journal of Medicinal Chemistry, 66 (2023) 13684-13704. http://doi.org/10.1021/acs.jmedchem.3c01068.

[243] Wang Xue, Jin Xueyang, Zhao Fabao, Xu Zejun, Tan Wenzhuo, Zhang Jiaozhen, Xu Yuliang, Luan Xiaoyi, Fang Min, Xie Zhiyu, Chang Wenqiang, Lou Hongxiang. Structure-based optimization of novel sterol 24-C-methyltransferase inhibitors for the treatment of candida albicans infections, Journal of Medicinal Chemistry, 67 (2024) 9318-9341. http://doi.org/10.1021/acs.jmedchem.4c00470.

[244] He Wei-Miao, Hu Jia-Hua, Cui Yu-Jia, Li Jing, Si Yu-Bing, Wang Shuai-Bo, Zhao Yu-Jing, Zhou Zhan, Ma Lu-Fang, Zang Shuang-Quan. Filling the gaps in icosahedral superatomic metal clusters, National Science Review, 11 (2024) nwae174. http://doi.org/10.1093/nsr/nwae174.

[245] Liu Chunhui, Han Peilin, Hou Xiaoxiao, Ge Suxiang, Wei Donghui. A general mechanistic map of organocatalytic hydroboration of alkynes: polarity controlled switchable selective pathways, Organic Chemistry Frontiers, 11 (2024) 3952-3961. http://doi.org/10.1039/D4QO00702F.

[246] Wu Yuanqi, Ao Yuhui, Li Zhiming, Liu Chunhui, Zhao Jinbo, Gao Wenyu, Li Xuemeng, Wang Hui, Liu Yongsheng, Liu Yu. Modulation of metal species as control point for Ni-catalyzed stereodivergent semihydrogenation of alkynes with water, Nature Communications, 14 (2023) 1655. http://doi.org/10.1038/s41467-023-37022-w.

[247] Deng Shicheng, Wang Songfan, Wang Yuanyuan, Xiao Qian, Meng Yuena, Kou Dongxing, Zhou Wenhui, Zhou Zhengji, Zheng Zhi, Wu Sixin. Impact of oxygen incorporation on interface optimization and defect suppression for efficiency enhancement in $Cu_2ZnSn(S, Se)_4$ solar cells, Journal of Energy Chemistry, 95 (2024) 77-85. https://doi.org/10.1016/j.jechem.2024.03.026.

[248] Hui Yao, Liu Rukuan, Gong Yiming, Lan Jingwen, Chen Youhui, Wu Lijun, Xu Airong. Real case: A robust hydrogel strain sensor lifts up 80 kg of a boy volunteer, Sensors and Actuators B: Chemical, 419 (2024) 136346. https://doi.org/10.1016/j.snb.2024.136346.

[249] Xu Silin, Yan Kai-Cheng, Xu Zhi-Hong, Wang Yuan, D Tony, James. Fluorescent probes for targeting the Golgi apparatus: design strategies and applications, Chemical Society Reviews, 53 (2024) 7590-7631. http://doi.org/10.1039/D3CS00171G.

[250] Tian Yu-Man, Wu Wei-Na, Zhao Xiao-Lei, Wang Yuan, Fan Yun-Chang, Xu Zhi-Hong. Dual fluorescence and electrochemical detection of carbon monoxide based on a ferrocene-chalcone platform, Sensors and Actuators B: Chemical, 419 (2024) 136440. https://doi.org/10.1016/j.snb.2024.136440.

[251] Gong Jiawen, Liu Quan, Cai Linlin, Yang Qi, Tong Yuping, Chen Xi, Kotha Sumasri, Mao Xiaobo, He Weiwei. Multimechanism collaborative superior antioxidant CDzymes to alleviate salt stress-induced oxidative damage in plant growth, ACS Sustainable Chemistry & Engineering, 11 (2023) 4237-4247. http://doi.org/10.1021/acssuschemeng.2c07371.

[252] Geng H., Li Z., Liu Q., Yang Q., Jia H., Chen Q., Zhou A., He W.. Boosting the peroxidase-like activity of Pt nanozymes by a synergistic effect of $Ti_{(3)}C_{(2)}$ nanosheets for dual mechanism detection, Dalton transactions (Cambridge, England : 2003), 51 (2022) 11693-11702. http://doi.org/10.1039/d2dt01696f.

[253] Jia Huimin, Gong Jiawen, Hu Zheyuan, Wen Tao, Li Caixia, Chen Yuyang, Huang Jihong, He Weiwei. Antioxidant carbon dots nanozymes alleviate stress-induced depression by modulating gut microbiota, Langmuir, 40 (2024) 19739-19750. http://doi.org/10.1021/acs.langmuir.4c02481.

[254] Zhang Ziyi, Liu Dan, Zhang Xiaoshuo, Luo Xueli, Lin Wanmei, Li Zhonghong, Huang Jihong. Silver nanoparticles deposited carbon microspheres nanozyme with enhanced peroxidase-like catalysis for colorimetric detection of Hg^{2+} in seafood, Microchimica Acta, 190 (2023) 340. http://doi.org/10.1007/s00604-023-05921-w.

[255] Guo Weiyun, Luo Linpin, Nian Ying, Wang Jianlong, Huang Jihong. pH-responsive dual-enzyme mimics based on hollow metal organic framework-derivatives β-$Co(OH)_2$ for multiple colorimetric assays, Microchimica Acta, 190 (2023) 240. http://doi.org/10.1007/s00604-023-05816-w.